

https://dspace.org/

Fabrication of transition and alkali metal-based quaternary nanoparticle counter electrodes for application in dye sensitized solar cells

Mabanne, Thomas

2025-05

University of the Witwatersrand, Johannesburg

https://hdl.handle.net/10539/50320

Mabanne, Thomas. (2025). Fabrication of transition and alkali metal-based quaternary nanoparticle counter electrodes for application in dye sensitized solar cells. [Master's dissertation, University of the Witwatersrand, Johannesburg]. WIReDSpace. https://hdl.handle.net/10539/50320

Downloaded from a DSpace repository. https://dspace.org/

Fabrication of transition and alkali metal-based quaternary nanoparticle counter electrodes for application in dye sensitized solar cells

WITS UNIVERSITY



A dissertation submitted to the Faculty of Science, University of the Witwatersrand, in fulfilment of the degree of Master of Science in Chemistry.

By

Thomas Mabanne

2114783



UNIVERSITY OF THE
WITWATERSRAND,
JOHANNESBURG

Supervisor: Dr. Grace Ngubeni

Co-Supervisor: Prof. Nosipho Moloto

12/05/2025

Date of submission

Declaration

I hereby declare that the work reported in this dissertation is my own independent work, submitted at the School of Chemistry, University of the Witwatersrand, Johannesburg. This work has not been submitted for any degree or examination in any other institution of higher learning.



Thomas Mabanne (Candidate) — 05/05/2025 Date

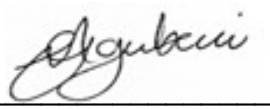

Dr. Grace N. Ngubeni (Supervisor) — 05/05/2025 Date



Prof. Nosipho Moloto (Co-supervisor) — 05/05/2025 Date

Abstract

Herein, the colloidal synthesis of Copper (Cu)-based quaternary semiconductor Cu_2ZnSnS_4 (CZTS), as well as the first-time colloidal synthesis of two alkali metal-based quaternary semiconducting nanoparticle analogues of CZTS, known as Li_2ZnSnS_4 (LZTS) and Na_2ZnSnS_4 (NZTS) using oleylamine (OLA) as a capping agent were investigated. Nuclear magnetic resonance (NMR) spectroscopy, transmission electron microscopy (TEM), X-ray diffraction (XRD), energy dispersive X-ray (EDX) spectroscopy, Fourier-transform infrared (FTIR) spectroscopy, X-ray photoelectron spectroscopy (XPS), ultra-violet visible (UV-Vis) spectroscopy, and Raman spectroscopy were used to characterize the nanoparticles.

As demonstrated by the XRD results, CZTS adopted a kesterite crystal structure, LZTS adopted a mixture of kesterite and wurtzite crystal structure while NZTS adopted a mixture of kesterite and cubic crystal structures. These structural properties were further corroborated using HRTEM and Raman spectroscopy. FTIR indicated that all the nanoparticles were capped through the amine functional group of the capping agent, a conclusion further validated by ^{1}H NMR studies. Solid state NMR identified characteristic peaks for lithium and sodium, indicating the presence of these elements in the as-synthesized LZTS and NZTS nanoparticles. By detecting the presence of each element (i.e. Cu^+, Na^+, Zn^{2+}, Sn^{4+} and S^{2-}) in the as-synthesised nanoparticles, EDX and XPS verified their elemental composition and oxidation states. Based on TEM results, the average sizes of CZTS, LZTS and NZTS nanoparticles were 20 ± 5 nm, 8 ± 1 nm, 5 ± 1 nm respectively. Additionally, all the particles were compact and polydispersed.

A drop-casting method was then used to fabricate thin film counter electrodes from the as-synthesized nanoparticles. Atomic force microscopy (AFM) investigation of CZTS, LZTS, and NZTS thin films yielded root mean square (rms) values of 138.23 nm, 22.49 nm, and 67.95 nm, respectively. These AFM results suggested that the CZTS counter electrode had the largest electrocatalytic surface area for the reduction of the I^-/I_3^- electrolyte compared to LZTS and NZTS counter electrodes. Following that, electrochemical impedance spectroscopy (EIS), cyclic voltammetry (CV), and Tafel polarization measurements were used to examine and compare the electrochemical

properties of the counter electrodes with those of Pt. From CV studies, CZTS had the highest cathodic peak current density of 3.40 $\mathrm{mAcm^{-2}}$ compared to LZTS (0.112 $\mathrm{mAcm^{-2}}$) and NZTS (0.0954 $\mathrm{mAcm^{-2}}$). EIS results showed that the charge transfer resistance (R_{CT}) value for CZTS (1.64 kΩ) was far much lower than that of LZTS (125.2 kΩ) and NZTS (290.4 kΩ), thus suggesting that CZTS had better charge transfer kinetics. According to the Tafel polarization measurements, the values of the limiting diffusion current density (J_{lim}) and the exchange current density (J_0) increased in the following order: NZTS < LZTS < CZTS < Pt. The electrochemical studies led to the general conclusion that all of the counter electrodes had electrocatalytic activity in the following order: NZTS < LZTS < CZTS < Pt.

While alkali metal-based quaternary semiconductor counter electrodes demonstrated lower electrocatalytic performance compared to CZTS and Pt, this study highlights their potential as cost-effective alternatives to Pt in DSSCs. The findings suggest that further optimization, such as incorporating composites, might considerably improve the electrochemical properties of these alkali metal-based materials. This research provides a foundation for developing innovative strategies to improve the performance and cost-effectiveness of DSSC counter electrodes.

Dedication

I dedicate this work to my mother, my siblings, my late father and all who have supported me throughout this journey.

Acknowledgments

First and foremost, I am deeply thankful to God Almighty for blessing me with life and the chance to pursue my dreams.

I also extend my heartfelt appreciation to my supervisor, Dr. Grace Ngubeni. Thank you so much for the guidance, sustained interest and continuous encouragement from my honors program through to the completion of this master's program. Thank you for believing in me with this project. Thank you for your time when I needed your assistance and input with regards to the project even outside office hours and during weekends. Thank you for sharing your life experiences with me, your expertise and skills. I have learned so much from you. I will forever be grateful for the opportunity. I would also like to extend my appreciation to my co-supervisor, Prof. Nosipho Moloto. I highly appreciate your support, your input and suggestions regarding this project. I am grateful for everything

A special thanks to Dr Memory Zimuwandeyi and Mr Thabiso Kojoana for their assistance with NMR measurements, Ms Louise Mostert at CSIR NMISA for the XPS measurements, Ms Rhandzu Rikhotso-Mbungela at CSIR for HRTEM analysis. Thank you to Wits MMU for providing the microscopic instrumentation and expertise for XRD and TEM analysis. Completion of this work would not be possible without the School of Chemistry at the University of the Witwatersrand affording me the opportunity to carry out my research and Tata scholarship, Innovent foundation and Mining Qualifications Authority (MQA) for funding my postgraduate studies.

I would also like to extend my special thanks to all my colleagues in Lab 330B, as well as the Carbo-Nano and CATOMAT groups, for your contributions and for making my MSc journey truly memorable.

Finally, I want to express my gratitude to my family for their support in my pursuit of my dreams. A heartfelt thank you to my greatest supporter, my mother. I appreciate your unwavering encouragement throughout this challenging academic journey and your belief in me. Your guidance and support have truly made a difference.

List of Presentations

Oral Presentations

- Oral presentation at NANOWEBS seminar held at Chemistry department, University of the Witwatersrand on the 26/10/2023.
- Oral presentation at Catalysis and Materials (CATMAT) seminar held at Chemistry department, University of the Witwatersrand on the 15/03/2024.
- Oral presentation at CARBO-NANO seminar held at Chemistry department, University of the Witwatersrand on the 06/08/2024.

Poster presentations

- Poster presentation at the Wits School of Chemistry Annual MSc poster conference held at the University of the Witwatersrand on the 27/09/2024.
- Poster presentation at the 9th international conference on nanoscience and nanotechnology (NanoAfrica 2024) from 20/10/2024 to 24/10/2024 [**3rd place prize**].
- Poster presentation for SACI Central Section Young Chemists' Symposium 2024 hosted by North-West University online on the 4/12/2024 [**1st place prize**].

Table of Contents

Declaration ---------- ii

Abstract ---------- iii

Dedication ---------- v

Acknowledgments ---------- vi

List of Presentations ---------- vii

Table of Contents ---------- viii

List of figures ---------- xii

List of tables ---------- xv

List of symbols and abbreviations ---------- xvi

Dissertation synopsis ---------- xix

Chapter 1: General background ---------- 1

1.1. Introduction ---------- 1

1.2. Problem statement ---------- 3

1.3. Rationale ---------- 3

1.4. Aims and objectives ---------- 4

1.5. References ---------- 5

Chapter 2: Literature review ---------- 7

2.1. Introduction to semiconducting nanoparticles ---------- 7

2.1.1. Semiconducting nanoparticles ---------- 7

2.1.2. Quantum confinement effects ---------- 8

2.2. Cu-based quaternary chalcogenide semiconductors ---------- 9

2.2.1. Cu_2ZnSnS_4 semiconducting quaternary chalcogenides ---------- 10

2.3. Synthetic methods used to synthesize quaternary semiconducting nanomaterials ---------- 11

2.3.1. Top-down methods ---------- 12

2.3.1.1. Mechanical milling ---------- 12

2.3.1.2. Sputtering ---------- 13
2.3.2. Bottom-up methods ---------- 14
2.3.2.1. Sol-gel ---------- 14
2.3.2.2. Colloidal synthesis ---------- 16
2.3.2.2.1. Nucleation ---------- 16
2.3.2.2.1.1. LaMer's nucleation theory ---------- 18
2.3.2.2.2. Growth ---------- 19
2.4. Dye sensitized solar cell ---------- 20
2.4.1. Electrolyte ---------- 21
2.4.2. Counter electrode ---------- 21
2.4.3. Photoanode ---------- 21
2.4.4. Working principle of a DSSC ---------- 22
2.5. Characterization of the counter electrodes of DSSCs ---------- 23
2.5.1. Atomic force microscopy ---------- 24
2.5.1.1. Principle of AFM [73]–[75]. ---------- 24
2.5.2. Cyclic voltammetry ---------- 25
2.5.3. Electrochemical impedance spectroscopy ---------- 27
2.5.4. Tafel polarization ---------- 28
2.5.5. Current voltage measurements ---------- 29
2.6. References ---------- 31
Chapter 3: Colloidal synthesis and characterization of Cu_2ZnSnS_4, Li_2ZnSnS_4 and Na_2ZnSnS_4 nanoparticles ---------- 39
3.1. Introduction ---------- 39
3.2. Experimental section ---------- 40
3.2.1. Chemicals ---------- 40
3.2.2. Colloidal synthesis of the CZTS, LZTS and NZTS nanoparticles ---------- 40
3.3. Characterization ---------- 41

3.4. Results and discussions ---- 42
3.4.1. X-Ray Diffraction analysis ---- 42
3.4.2. FTIR analysis ---- 45
3.4.3. NMR analysis ---- 46
3.4.4. TEM analysis ---- 49
3.4.5. UV-Vis absorption analysis ---- 51
3.4.6. XPS analysis ---- 52
3.4.6.1. CZTS ---- 52
3.4.6.2. LZTS ---- 55
3.4.6.3. NZTS ---- 57
3.4.7. Raman analysis ---- 59
3.5. Conclusion ---- 61
3.6. References ---- 62
Chapter 4: Elucidating the electrochemical properties of CZTS, LZTS and NZTS quaternary semiconductors for potential application as counter electrodes in dye-sensitized solar cells ---- 66
4.1. Introduction ---- 66
4.2. Experimental section ---- 67
4.4.1. Chemicals ---- 67
4.2.2. Counter electrode preparation ---- 67
4.3. Characterization ---- 68
4.4. Results and discussions ---- 69
4.4.1. Electrochemical analysis ---- 69
4.4.1.1. Cyclic voltammetry studies ---- 69
4.4.1.2. Electrochemical impedance studies ---- 73
4.4.1.3. Tafel polarization studies ---- 75
4.4.2. Atomic force microscopy analysis ---- 76

4.5. Conclusion ---------- 77
4.6. References ---------- 80
CHAPTER 5: Overall conclusions, recommendations and future work ---------- 83
5.1: Conclusions ---------- 83
5.2: Recommendations and future work ---------- 85
Appendix ---------- 86
Supporting information ---------- 86

List of figures

Figure 1.1: South Africa's energy mix in 2020 [3]. 1
Figure 1.2: SDG 7 illustrating progress being made with regards to moving away from traditional to renewable energy sources [20]. 2
Figure 2.1: (a) A diagram depicting electronic energy levels and (b) Direct and Indirect bandgap structures that show the variations in momentum plane [5]–[6]. 8
Figure 2.2: Diagram illustrating the increase in band-gap energy as nanoparticle size decreases due to quantum confinement effects [9]. 9
Figure 2.3: (a) Schematic illustration depicting the origin of the CZTS structure [16], (b) kesterite, (c) stannite, (d) wurtzite crystal phases of CZTS [71]. 10
Figure 2.4: Antisite defect occurring in the Kesterite crystal structure of CZTS [72]. 11
Figure 2.5: Diagrammatic representation of the bottom-up and top-down synthetic approaches. 12
Figure 2.6: Schematic diagram demonstrating the principle of ball milling method for nanoparticle formation [31]. 13
Figure 2.7: Schematic diagram demonstrating the principle of sputtering method for nanoparticle formation [32]. 14
Figure 2.8: A graph showing the Gibbs free energy in relation to the clusters' radius. 17
Figure 2.9: LaMer's nucleation and growth model [43]. 19
Figure 2.10: A simplified diagram illustrating the fundamental components of a DSSC [45]. 20
Figure 2.11: Schematic illustrations showing the operation principle of AFM [75]. .. 24
Figure 2.12: The peak cathodic potential (E_{pc}), peak anodic potential (E_{pa}), and peak current density (i_p) are highlighted in this schematic illustration of a cyclic voltammogram [60]. 26
Figure 2.13: Nyquist curves derived from symmetric dummy cells composed of Pt (*insert*), CZTS and varying weight percentages of graphene with CZTS [65]. 27
Figure 2.14: Tafel polarization plot derived from symmetric dummy cells composed of Pt, CZTS and varying weight percentages of graphene with CZTS [65]. 28
Figure 2.15: Typical I-V curve obtained from photocurrent-voltage measurement [69]. 30
Figure 3.1: Schematic diagram showing the synthesis of the nanoparticles. 41

Figure 3.2: XRD patterns of the as-synthesized (a) CZTS, (b) LZTS and (c) NZTS nanoparticles. 44
Figure 3.3: FTIR spectra of OLA, CZTS, LZTS and NZTS. 46
Figure 3.4: ^{1}H NMR spectra of OLA, CZTS, LZTS and NZTS nanoparticles. 48
Figure 3.5: SSNMR spectra of (a) LZTS and (b) NZTS nanoparticles. 49
Figure 3.6: TEM images of (a) CZTS, (b) LZTS and (c) NZTS nanoparticles including particle size distribution histograms (d – f). 50
Figure 3.7: HRTEM images showing the d-spacing values of lattice fringes of (a) CZTS, (b) LZTS, and (c) NZTS nanoparticles. 51
Figure 3.8: (a) UV-Vis absorption spectra and (b) Tauc plot of CZTS, LZTS and NZTS nanoparticles. 52
Figure 3.9: (a) XPS survey spectrum and high-resolution spectra of (b) copper, (c) zinc, (d) tin and (e) sulphur from CZTS nanoparticles. 54
Figure 3.10: High-resolution spectra of (a) carbon, (b) oxygen and (c) nitrogen from CZTS nanoparticles. 55
Figure 3.11: (a) XPS survey spectrum and high-resolution spectra of (b) zinc, (c) tin and (d) sulphur from LZTS nanoparticles. 56
Figure 3.12: High-resolution spectra of (a) carbon, (b) oxygen and (c) nitrogen from LZTS nanoparticles. 57
Figure 3.13: (a) XPS survey spectrum and high-resolution spectra of (b) sodium, (c) zinc, (d) tin and (e) sulphur from NZTS nanoparticles. 58
Figure 3.14: High-resolution spectra of (a) chlorine, (b) carbon, (c) oxygen and (d) nitrogen from NZTS nanoparticles. 59
Figure 3.15: Raman spectra of (a) CZTS, (b) LZTS and (c) NZTS nanoparticles. .. 60
Figure 4.1: Setup for the preparation of the counter electrode and for electrochemical measurements. 68
Figure 4.2: Cyclic voltammograms of (a) CZTS and Pt, (b) LZTS and NZTS at a scan rate of 50 mV/s on GC. 69
Figure 4.3: (a) – (c) Stability assessment of the prepared CZTS, LZTS & NZTS counter electrodes after 50 cycles at 100 mV/s on GC and (d) relationship between the number of CV scans at the obtained current density (black y-axis for CZTS and purple y-axis for LZTS and NZTS). 72

Figure 4.4: Cyclic voltammograms of (a) CZTS, (b) LZTS, (c) NZTS counter electrodes on GC at varying scan rates from 10 mV/s to 100 mV/s and (d) – (f) relationship between the square root of the counter electrodes' scan rates and the anodic and cathodic peak currents. 73
Figure 4.5: (a) Nyquist plot and (b) equivalent circuit used to fit EIS results for the symmetric cells fabricated with two identical electrodes of CZTS (*insert*), LZTS, NZTS and Pt (*insert*) on FTO. 74
Figure 4.6: Tafel polarization curves for the symmetric cells fabricated with two identical electrodes of CZTS, LZTS, NZTS and Pt on FTO. 75
Figure 4.7: 2D and 3D AFM micrographs of (a) CZTS, (b) LZTS and (c) NZTS thin films on FTO substrate. 77
Figure S3.1: (a) - (c) TEM images of NZTS nanocubes and (d) particle size distribution histogram based on the diagonal lengths (red double arrow line) of the nanocubes. 86
Figure S3.2: EDX mapping showing the elemental composition of CZTS nanoparticles along with the corresponding TEM micrograph of CZTS. 87
Figure S3.3: EDX mapping showing the elemental composition of LZTS nanoparticles along with the corresponding TEM micrograph of LZTS. 87
Figure S3.4: EDX mapping showing the elemental composition of NZTS nanoparticles along with the corresponding TEM micrograph of NZTS. 88
Figure S4.1: XRD of (a) CZTS, (b) LZTS and (c) NZTS thin films fabricated on FTO conductive glass substrate. 92

List of tables

Table 3.1: NMR spectral assignments for OLA, CZTS, LZTS and NZTS nanoparticles. 47

Table 4.1: Parameters obtained from the cyclic voltammetry of the three-electrode half-cell setup. 70

Table 4.2: Summary of the electrochemical performance parameters obtained from EIS. 75

Table 4.3: Electrochemical performance parameters from EIS & Tafel polarization curves for the counter electrodes. 76

Table S3.1: Summary of the atomic composition stoichiometric assignments obtained from the fitting of the XPS spectra for CZTS. 89

Table S3.2: Summary of the atomic composition stoichiometric assignments obtained from the fitting of the XPS spectra for LZTS. 90

Table S3.3: Summary of the atomic composition stoichiometric assignments obtained from the fitting of the XPS spectra for NZTS. 91

List of symbols and abbreviations

$\mathbf{I^-/I_3^-}$ – Iodide/triiodide redox couple

$\mathbf{J_{pc}}$ – Cathodic peak current density

AFM – Atomic Force Microscopy

CB – Conduction band

CIGS – Copper indium gallium selenide ($Cu(InGa)Se_2$)

Cl – Chlorine

CNT – Classical nucleation theory

CQCs – Cu-based quaternary chalcogenide semiconductors

Cu – Copper

CV – Cyclic voltammetry

CZTS – Copper zinc tin sulfide (Cu_2ZnSnS_4)

$\mathbf{D_o}$ – Diffusion coefficient

DSSC – Dye sensitized solar cell

EDX – Energy dispersive X-ray

EELLS – Electron energy-loss spectroscopy

$\mathbf{E_g}$ – Band gap energy

EIS – Electrochemical impedance spectroscopy

FCC – Face-centred cubic

FF – Fill factor

FTIR – Fourier transform infrared spectroscopy

FTO – Fluorine-doped tin oxide

Ga – Gallium

GC – Glassy carbon

HOMO – Highest occupied molecular orbital

In – Indium

J_0 – Exchange current density

J_{lim} – Limiting diffusion current density

J_{sc} – Short circuit current density

Li – Lithium

LSNMR – Liquid state NMR

LUMO – Lowest unoccupied molecular orbital

LZTS – Lithium zinc tin sulphide (Li_2ZnSnS_4)

MAS NMR – Magic angle spinning nuclear magnetic resonance

Na – Sodium

NMR – Nuclear magnetic resonance spectroscopy

NZTS – Sodium zinc tin sulfide (Na_2ZnSnS_4)

OLA – Oleylamine

PCE – Power conversion efficiency

Pt – Platinum

R_{CT} – Charge transfer resistance

rms – Root mean square

R_S – Series resistance

S – Sulphur

Sn – Tin

SSNMR – Solid state NMR

TEM – Transmission electron microscopy

UV-Vis – Ultraviolet-Visible spectroscopy

VB – Valence band

V_{oc} – Open circuit voltage

XPS – X-ray photoelectron spectroscopy

XRD – X-ray diffraction

Zn – Zinc

ΔE_{pp} – Peak-to-peak potential difference

Dissertation synopsis

The aim of this research was to use a low-cost colloidal method to synthesize and characterize Cu-based quaternary semiconductor (CZTS) and its alkali metal-based quaternary semiconductor analogues (LZTS and NZTS). Then evaluate the electrocatalytic properties of the semiconductors using cyclic voltammetry (CV), electrochemical impedance spectroscopy (EIS) and Tafel polarization for their potential application as counter electrodes in dye-sensitized solar cells (DSSCs) as potential replacements for expensive Pt-based counter electrodes. The layout of the dissertation is therefore shown below:

Chapter 1: Provides the general background, problem statement and rationale for the study as well as aims and objectives.

Chapter 2: The backbone of this study will be detailed in the literature review as such general introduction to semiconducting nanoparticles, copper-based quaternary chalcogenide semiconductors, various synthetic methods used to synthesize quaternary semiconducting nanomaterials. There is also a detailed description of the individual components of DSSCs, the working principle of DSSCs as well as how the performance parameters of the cell can be evaluated.

Chapter 3: Reports on the synthesis and characterization of CZTS as well as the novel synthesis of LZTS & NZTS using a low-cost colloidal method.

Chapter 4: This part of the study reports on the electrocatalytic properties of the thin films fabricated from CZTS, LZTS and NZTS nanoparticles in the redox reaction of the iodide-triiodide electrolyte system as potential alternative counter electrodes in dye-sensitized solar cells.

Chapter 5: Critically underlines the conclusions deduced from this study and likely the possibility of future studies.

***Appendix*:** Will have all the supplementary figures and tables from chapter 3 and chapter 4.

Chapter 1: General background

1.1. Introduction

Energy has become an essential component of our daily lives after having a significant impact on the development of human civilization. Numerous tasks involving the production and storage of food, transportation, lighting, and cooking all need some form of energy. For millennia, the primary fuel source enabling the global economy to meet its energy needs has been fossil fuels, including natural gas, petroleum, oil and coal [1]. In 2020, over 85% of the electricity generated in the country (Figure 1.1) was anticipated to come from coal, making coal the major energy fuel source in South Africa [2,3]. In addition to polluting the air and contributing to climate change, burning coal releases greenhouse gases that have an adverse effect on human health [4].

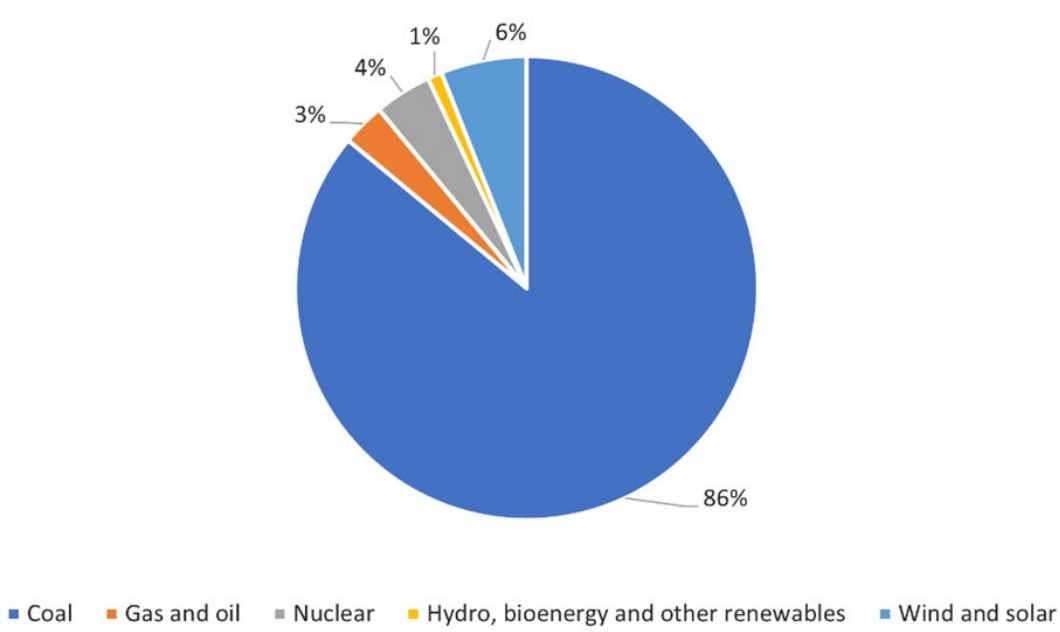

Figure 1.1: South Africa's energy mix in 2020 [3].

Eskom which is South Africa's main electricity supplier had to resort to the implementation of loadshedding to cut down on electricity usage and reduce overloading the electric grid [5]. In light of this, it is critical to transition away from a coal-dominated energy mix and invest in renewable energy sources (Figure 1.2) to generate power, as loadshedding disrupts all operations that rely on the grid for energy supplies.

Research on renewable energy has concentrated on enhancing solar cell performance through environmentally friendly techniques [6]. These methods include hydrogen, solar and wind. Among various renewable energy sources, solar energy has gained greater attention due to its minimal environmental impact and its potential for production by most countries.



Figure 1.2: SDG 7 illustrating progress being made with regards to moving away from traditional to renewable energy sources [20].

Based on their designs and principles of operation, solar cells are divided into three generations. These distinct generations effectively narrate the evolutionary stages that have shaped their development over time [6–8]. Crystalline silicon or gallium arsenide (GaAs) wafers served as the foundation for the *first-generation* of solar cells [8]. Silicon-based solar cells require expensive materials and a more energy-intensive fabrication process [9]. The *second-generation* solar cells have shown to be superior since they use less materials and are manufactured at low temperatures [9]. They use materials such as cadmium telluride (CdTe), amorphous silicon and copper indium gallium selenide (CIGS), which are based on thin film fabrication technology [8,9]. Lastly, the *third-generation* solar cells are aimed at producing cells that are both inexpensive and highly efficient. Researchers investigating photovoltaics have

concentrated on materials which include polymers, organic compounds, dye-sensitized solar cells (DSSCs), and perovskites, as these represent the most cost-effective next-generation photovoltaic technologies. [9]. Due to their dependable photovoltaic performance in low light and reasonably cheap fabrication costs, DSSCs have drawn more interest than other available photovoltaic devices now on the market [10,11]. Considering the aforementioned points, this research project aims to investigate *third-generation* DSSCs.

1.2. Problem statement

The predominate counter electrode in DSSCs is platinum (Pt) deposited on a conductive glass substrate. When used to reduce charge carriers in a triiodide electrolyte, this substrate has remarkable stability, high conductivity, and a superior electrocatalytic activity [6,12,13]. However, the commonly used triiodide electrolyte readily corrodes Pt, forming PtI_4, which is not the most suitable material for use in DSSCs. Additionally, Pt is a valuable metal that raises the cost of making DSSCs, which restricts their use in extensive commercial applications [6,12,14]. As a result, it is necessary to explore substitute materials for Pt in counter electrodes. These materials need to be less expensive than Pt while exhibiting efficient electrocatalytic effects and strong electronic conductivity towards the reduction of the triiodide electrolyte [15].

1.3. Rationale

DSSCs show a promising answer to the current energy need if they can be commercialized cheaply for large scale applications. For that to happen the production costs of these devices need to be reduced while maintaining or improving their power to energy conversion. This project will explore replacing the traditional Pt-based counter electrode with a less expensive material that has similar electrochemical and catalytic properties as platinum. Quaternary semiconducting materials such as Cu_2ZnSnS_4 (CZTS), which are made up of less toxic and readily available elements in comparison to their traditional counterparts such as CdTe and CIGS which have toxic and rare elements such as Cd, Te, In and Ga, have been proposed as promising

candidates for the replacement of Pt-based counter electrodes in DSSCs [16]. This is because CZTS has excellent optical properties and a viable band gap, thus making it a promising replacement for Pt as a counter electrode in DSSCs. However, only power conversion efficiencies ranging from 3.14% – 7.56% were obtained when CZTS was used as a counter electrode in existing studies [6,16–19]. Therefore, we proposed the substitution of copper with sodium and lithium respectively, to produce analogues of CZTS known as Na_2ZnSnS_4 (NZTS) and Li_2ZnSnS_4 (LZTS).

1.4. Aims and objectives

Considering the above, this research was aimed at synthesizing Cu-based quaternary semiconductor, CZTS and its alkali metal-based quaternary semiconductor analogues, LZTS and NZTS. The proposed materials hold significant potential as promising alternatives to Pt for serving as counter electrodes in DSSCs. Thus, the objectives of the project were identified as follows:

- To use the sequential addition colloidal method to synthesize CZTS, LZTS and NZTS nanoparticles.
- Fully characterize the synthesized nanoparticles using various characterization techniques.
- To prepare thin films using the synthesized nanoparticles.
- To evaluate the prepared thin films by applying atomic force microscopy (AFM) and X-ray diffraction (XRD) characterization techniques.
- To conduct electrochemical measurements of the prepared thin films and study their electrochemical properties.

1.5. References

[1] Zhang, L. Copper Zinc Tin Sulfide (Cu_2ZnSnS_4) Photovoltaic Material Development and Thin Film Solar Cells. *University of Minnesota Digital Conservancy* **2016**, 171.

[2] Akinbami, O. M.; Oke, S. R.; Bodunrin, M. O. The State of Renewable Energy Development in South Africa: An Overview. *Alexandria Engineering Journal* **2021**, *60* (6), 5077–5093.

[3] Otavio, V. South Africa Is Trying to Get Rid of Its Coal Addiction Coal Has a Hold on the Power Sector, but for Not Much Longer. *Nanyang Technological University*. Singapore December 27, **2021**. https://www.ntu.edu.sg/cas/news-events/news/details/south-africa-is-trying-to-get-rid-of-its-coal-addiction. (accessed 2023-10-03).

[4] Munawer, M. E. Human Health and Environmental Impacts of Coal Combustion and Post-Combustion Wastes. *Journal of Sustainable Mining* **2018**, *17* (2), 87–96.

[5] Mabunda, N. E. Use of Photovoltaic Energy to Minimize the Impact of Load-Shedding in South Africa. In *2021 International Conference on Electrical, Computer and Energy Technologies (ICECET)*; **2021**; pp 1–4.

[6] Imla Mary, C.; Senthilkumar, M.; Manobalaji, G.; Moorthy Babu, S. Solution Processed $Cu_2ZnSnSe_4$ Nanoink for Inexpensive Pt-Free Counter Electrode in Dye-Sensitized Solar Cells. *Solid State Sciences* **2021**, *116*, 106612.

[7] Islam, M.; Md Yatim, N.; Hashim, M. A Review of CZTS Thin Film Solar Cell Technology. *Journal of Advanced Research in Fluid Mechanics and Thermal Sciences* **2021**, *81*, 73–87.

[8] Pastuszak, J.; Węgierek, P. Photovoltaic Cell Generations and Current Research Directions for Their Development. *Materials* **2022**, *15* (16), 5542.

[9] Goswami, R. Three Generations of Solar Cells. *Advanced Materials Research* **2021**, *1165*, 113–130.

[10] Hug, H.; Bader, M.; Mair, P.; Glatzel, T. Biophotovoltaics: Natural Pigments in Dye-Sensitized Solar Cells. *Applied Energy* **2014**, *115*, 216–225.

[11] Juhász junger, I.; Werner, D.; Schwenzfeier-Hellkamp, E.; Ehrmann, A. Influence of Illumination Spectra on DSSC Performance. *Optik* **2019**, *177*, 8–12.

[12] Mposa, E.; Sithole, R. K.; Ndala, Z.; Ngubeni, G. N.; Mubiayi, K. P.; Shumbula, P. M.; Machogo-Phao, L. F. E.; Moloto, N. Novel 2D-AuSe Nanostructures as Effective Platinum Replacement Counter Electrodes in Dye-Sensitized Solar Cells. *RSC Adv.* **2022**, *12* (20), 12882–12890.

[13] Mahajan, P.; Datt, R.; Gupta, V.; Arya, S. Synthesis and Characterization of ZnO@WO3 Core/Shell Nanoparticles as Counter Electrode for Dye-Sensitized Solar Cell. *Surfaces and Interfaces* **2022**, *30*, 101920.

[14] Dissanayake, M. A. K. L.; Kumari, J. M. K. W.; Senadeera, G. K. R.; Jaseetharan, T.; Weerasinghe, J.; Anwar, H. A Low-Cost, Vein Graphite/Tin Oxide Nanoparticles Based Composite Counter Electrode for Efficient Dye-Sensitized Solar Cells. *Materials Science and Engineering: B* **2021**, *273*, 115440.

[15] Elindjeane Sheela, S.; Murugadoss, V.; Sittaramane, R.; Angaiah, S. Development of Tungsten Diselenide/Polyaniline Composite Nanofibers as an Efficient Electrocatalytic Counter Electrode Material for Dye-Sensitized Solar Cell. *Solar Energy* **2020**, *209*, 538–546.

[16] Chawla, P.; Jain, S.; Vashishtha, P.; Ahamed, M.; Sharma, S. N. Transition from CZTSe to CZTS via Multicomponent CZTSSe: Potential Low Cost Photovoltaic Absorbers. *Superlattices and Microstructures* **2018**, *113*, 502–509.

[17] Mokurala, K.; Kamble, A.; Bhargava, P.; Mallick, S. Fabrication of Dye Sensitized Solar Cells with Cost-Effective Quaternary Sulfide Counter Electrode. In *2014 IEEE International Conference on Power Electronics, Drives and Energy Systems (PEDES)*; **2014**; pp 1–4.

[18] S. Chen, X. Z.; Tao, J.; Tao, H.; Shen, Y.; Zhu, L.; Jiang, J.; Wang, T. Fabrication of Low Cost Kesterite Cu_2ZnSnS_4 (CZTS) Thin Films as Counter-Electrode for Dye Sensitised Solar Cells (DSSCs). *Materials Technology* **2015**, *30* (5), 306–312.

[19] Ngubeni, G. N.; Akinbami, O.; Mxakaza, L.; Nkabinde, S.; Kolokoto, T.; Otieno, F.; Moloto, M. J.; Mubiayi, K. P.; Moloto, N. Evaluating the Effect of the Substrate on the Electrocatalytic Performance of Cu_2ZnSnS_4 and $Cu_2ZnSnSe_4$Counter Electrodes in Dye-Sensitized Solar Cells. *Thin Solid Films* **2022**, *745*, 139099.

[20] 2023 Africa Sustainable Development Report. *United Nations Development Programme*. **2023** https://www.undp.org/africa/publications/2023-africa-sustainable-development-report (accessed 2025-01-07).

Chapter 2: Literature review

2.1. Introduction to semiconducting nanoparticles

2.1.1. Semiconducting nanoparticles

There has been a significant increase in the surge of interest in semiconducting nanoparticles and numerous researchers have directed their attention towards exploring the captivating properties and diverse applications of these nanoparticles. These applications include solar cells, water treatment, sensors, energy storage, optoelectronic devices, catalysis, medical imaging, and quantum computing [1,2]. These semiconducting nanoparticles exhibit unique optoelectronic and magnetic properties depending on their size and shape, which have never been observed in bulk materials [3,4]. The bulk material is primarily defined by the band gap energy (E_g) and the band structure, which can be either indirect or direct [5]. Each material has a unique E_g that varies depending on the material's bulk and its nanoparticle composition, as illustrated in Figure 2.1 (a). Excitation of an electron from the valence band (VB) to the conduction band (CB) requires the least amount of energy known as the E_g. As seen in Figure 2.1 (b), the lowest point of the CB and the highest point of the VB are located in the same momentum plane (k-axis) in the direct bandgap configuration. Thus, any photon with enough energy can easily activate electrons across the gap [6]. Conversely, an indirect bandgap structure occurs when the lowest point of the CB and highest point of the VB are not in the same momentum plane (k-axis) Figure 2.1 (b). An electron must alter its momentum to be excited from the valence band to the conduction band. A phonon interaction is necessary since photons are not momentum carriers.

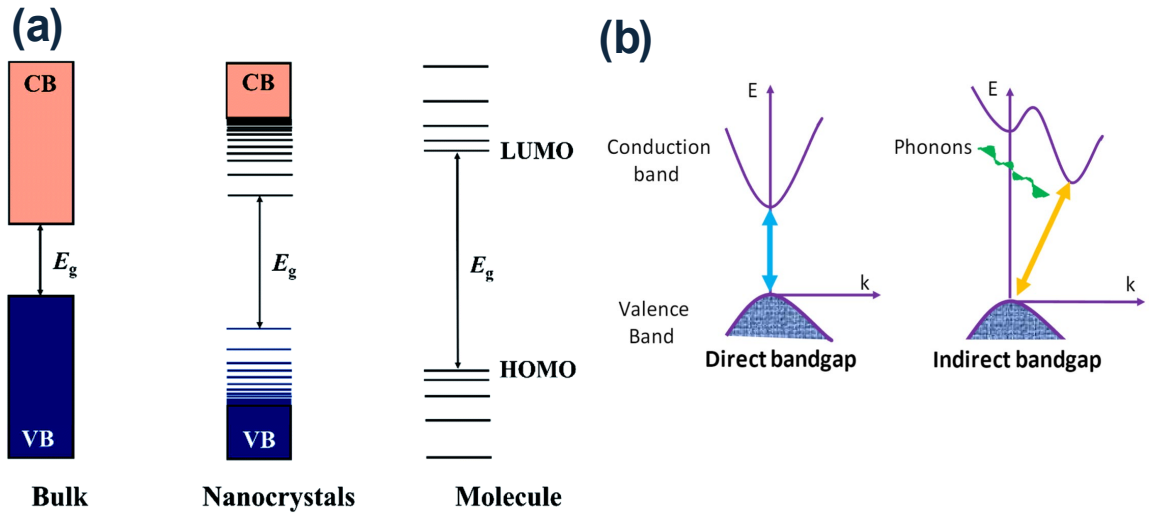

Figure 2.1: (a) A diagram depicting electronic energy levels and (b) Direct and Indirect bandgap structures that show the variations in momentum plane [5,6].

2.1.2. Quantum confinement effects

Quantum confinement primarily deals with the energy of electrons (or electron holes) within a confined space [7]. The effect is observed when a semiconductor nanoparticle's size approaches or falls below the exciton Bohr radius, which is between 2 and 50 nm [6,8,9]. The exciton Bohr radius for a particle is given by, $r_B = \varepsilon(\frac{m}{m^*})a_0$, where ε is the dielelectric constant of the material, m is the rest mass of the electron, m^* is the mass of the particle and a_0 is the Bohr radius of the hydrogen atom [10]. According to Figure 2.2, quantum confinement causes size-dependent changes in the energy gap and density of electronic states. These changes result in an increase in the bandgap and the appearance of discrete energy levels close to the band edges as the dimension of the nanoparticle decreases.

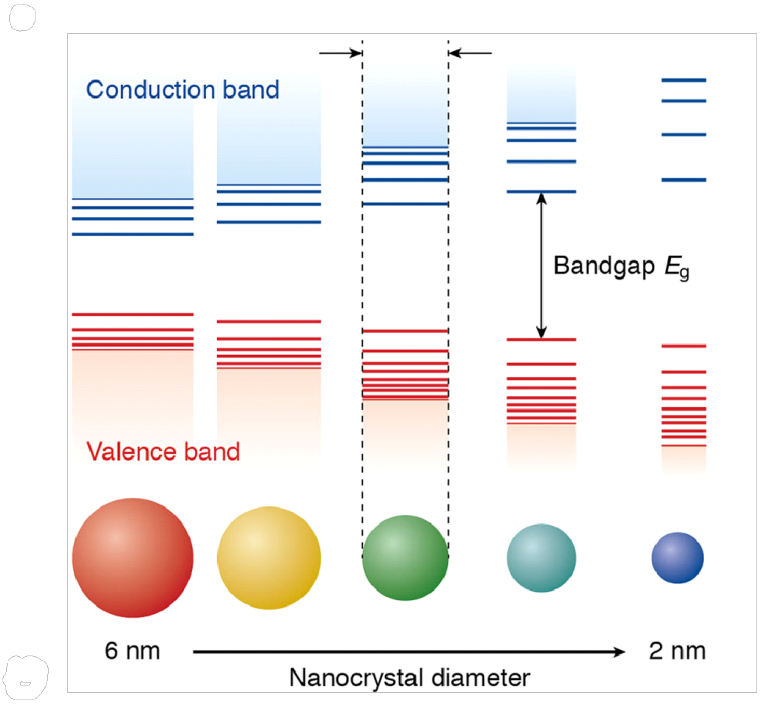

Figure 2.2: Diagram illustrating the increase in band-gap energy as nanoparticle size decreases due to quantum confinement effects [9].

2.2. Cu-based quaternary chalcogenide semiconductors

The quest for affordable and efficient materials for photovoltaic (PV) application has given rise to the exploration of Cu-based quaternary chalcogenides (CQCs) as promising alternative materials capable of substituting the costly Si-based PV technology [11]. $CuInGaSe_2$ (CIGS)-based semiconductor materials have seen remarkable success in the solar cell field since their initial discovery [12]. Solar cells using CIGS absorption layers currently have a maximum power conversion efficiency (PCE) of 23.4%, demonstrating the substantial application potential of CQCs [13]. However, the high price and availability of Ga and In were significant obstacles to the widespread use of CIGS in solar cells. As a result, it became imperative to create highly effective CQCs that would replace In, Ga, or both without sacrificing performance, utilizing readily available and reasonably priced materials. As a result, the earth-abundant elements Zn and Sn, respectively, were used to replace the In and Ga components in CIGS to create Cu_2ZnSnS_4 (CZTS) [12].

2.2.1. Cu_2ZnSnS_4 semiconducting quaternary chalcogenides

As previously mentioned in chapter 1, CZTS is a promising replacement for platinum (Pt) based counter electrodes in DSSCs. This is due to the quaternary semiconductors having, a high absorption coefficient (greater than 10^4 cm^{-1}), an optimum bandgap of 1 − 1.5 eV as well as a p-type conductivity [14,15]. This compound can also be formed through cation mutations (cross-substitutions) within copper indium sulphide ($CuInS_2$), where the In atoms are replaced by Zn and Sn atoms, as illustrated in Figure 2.3 (a) [16]. The quaternary CZTS is commonly known to crystalize and form 3 crystal phases, tetragonal kesterite (space group I4, Figure 2.3b), tetragonal stannite-type (space group I42m, Figure 2.3c) and wurtzite (space group Pc, Figure 2.3d) [17–19]. Distinguishing the three different crystal phases of CZTS using common techniques such as XRD and Raman spectroscopy is challenging because of their comparable atomic scattering factors of Cu and Zn [18]. Kuang Yu *et al*. and Mirjana Dimitrievska *et al*. both recognize the kesterite phase of CZTS as the most stable compared to the stannite and wurtzite phase. The conclusion was drawn based on data obtained from neutron diffraction experiments and a variety of computational studies employing pure or hybrid density function theories [18,19]. This could be the reason why CZTS is commonly referred to as "kesterite," as it predominantly crystallizes in the kesterite phase.

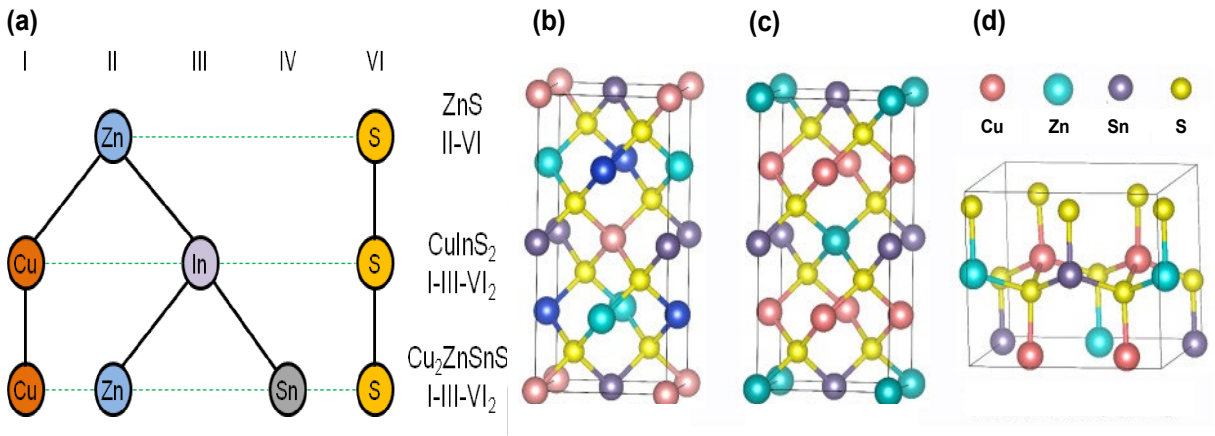

Figure 2.3: (a) Schematic illustration depicting the origin of the CZTS structure [16], (b) kesterite, (c) stannite, (d) wurtzite crystal phases of CZTS [71].

Working with the CZTS compound can be challenging at times due to its tendency to decompose at high temperatures. Moreover, without careful controlled reaction

conditions, various secondary phases like ZnS, Cu_2ZnS_3, and Cu_2S may coexist, further complicating the material's behaviour [20]. Moreover, a mixture of both the stannite and the kesterite crystal phase of CZTS can form during synthesis due to the phases having similar formation energies. The formation of crystal structure defects in CZTS is prone to occur, and among the most frequently observed defects is the antisite defect (Figure 2.4). This defect arises when Cu cations substitute Zn sites, and vice versa, owing to their comparable ionic radii [20]. The primary focus of current research is to gain a deeper understanding of the defects occurring within the CZTS crystal structure, aiming to minimize their occurrence and impact. This research project aims to investigate a potential method for preventing the formation of antisite defects in CZTS by replacing Cu with an atom of significantly different ion size, such as Na or Li. However, it should be noted that such a substitution may alter other properties of the material, such as crystal structure or the type of conductivity, which might then impact the electrochemical properties of the material for the application in DSSCs [21].

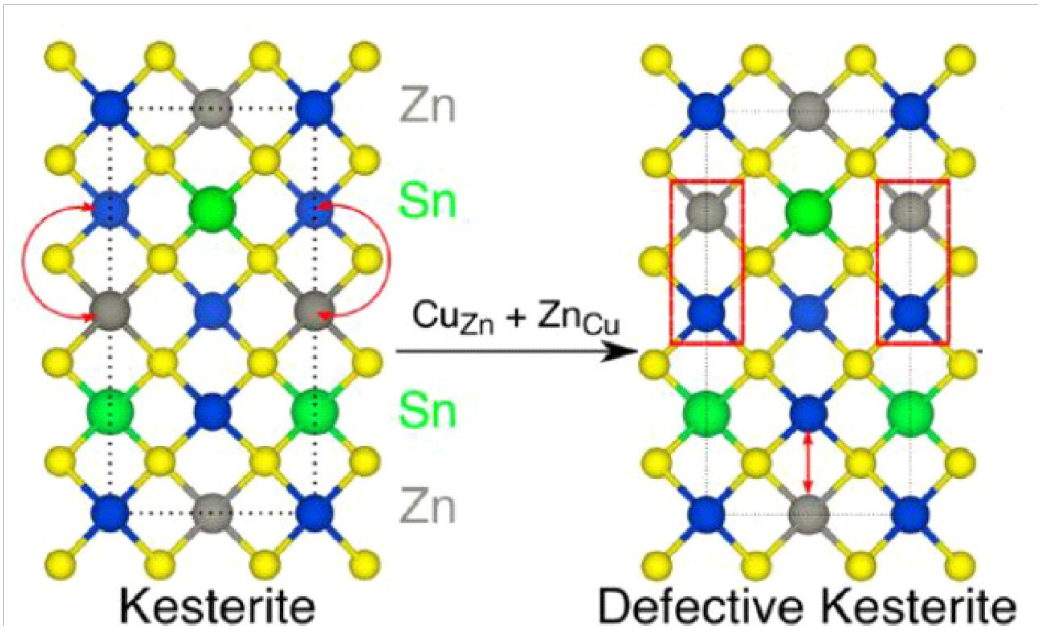

Figure 2.4: Antisite defect occurring in the Kesterite crystal structure of CZTS [72].

2.3. Synthetic methods used to synthesize quaternary semiconducting nanomaterials

The growing interest in the study of semiconducting nanoparticles has led scientists to look at a number of methods for synthesizing these nanomaterials; some of these

methods are discussed in this section. As seen in Figure 2.5, there are two broad approaches for synthesizing quaternary semiconducting nanomaterials namely the bottom-up and top-down methods. The top-down method, is sometimes referred to as the destructive method, works by breaking down bulk materials into smaller units, which are subsequently transformed into the appropriate nanoparticles [22–24]. Atoms and molecules self-assemble to form new nuclei or clusters, which subsequently develop into nanoparticles, according to the bottom-up approach [22,25]. The bottom-up method is more preferred as it results in the production of nanostructures with less defects and more homogenous chemical compositions [26].

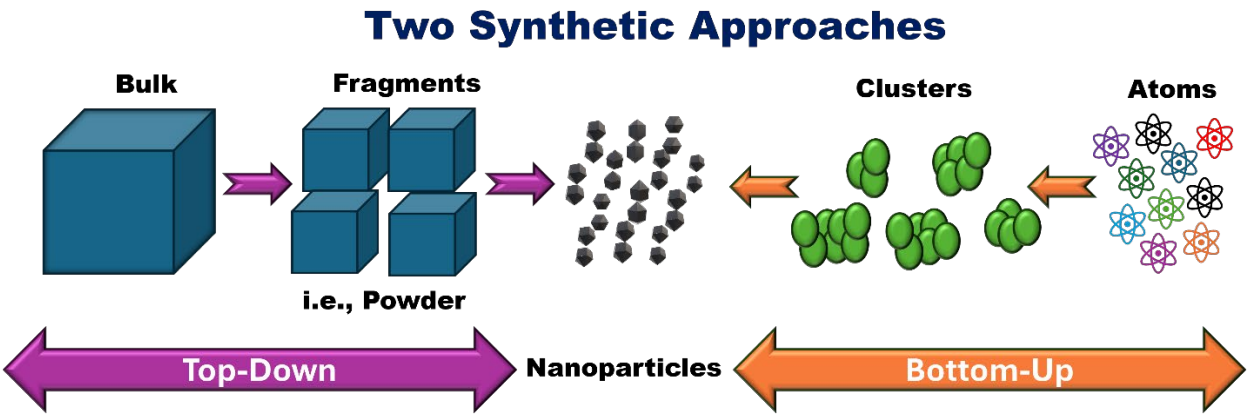

Figure 2.5: Diagrammatic representation of the bottom-up and top-down synthetic approaches.

2.3.1. Top-down methods

Top-down methods are useful for producing large amounts of nanomaterials, but controlling their size and shape can be difficult. Ball-milling and sputtering are among the top-down synthesis methods.

2.3.1.1. Mechanical milling

Ball milling, which creates nanoparticles through attrition, is the most straightforward and effective mechanical procedure in the top-down method [27]. In this process, kinetic energy is transferred from the grinding medium to the material being reduced. The milled materials rupture into smaller particles with newly formed surfaces as a result of their chemical bonds breaking (Figure 2.6) [27,28]. The amount of energy transfer between the balls and the material during the process is controlled by the milling media, milling speed, ball-to-powder weight ratio, type of milling (dry or wet),

type of high energy ball mill (vibrator mill, planetary mill, attritor mill, tumbler ball mill, etc.), milling atmosphere, and milling duration. The morphological and physical characteristics of the resulting nanomaterials are thus affected by these factors [28].

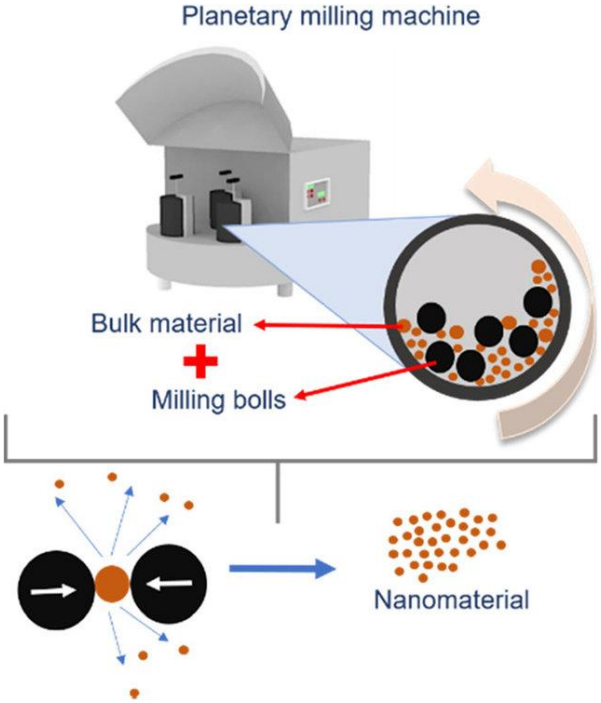

Figure 2.6: Schematic diagram demonstrating the principle of ball milling method for nanoparticle formation [31].

2.3.1.2. Sputtering

The non-thermal vaporization process of sputtering makes it more popular in top-down methods [27]. Through the physical process of sputtering, atoms in a target material that is in the solid state are forced out of it by high-energy ions bombarding it. The atoms then enter the gas phase and land on a substrate surface, where they form a film [27]. This method uses inert gas ions between two electrodes, one for the substrate and the other for the target material (Figure 2.7) [29]. Sputtering is separated into three categories: magnetron, radio frequency (RF) and direct current (DC) sputtering. These categories are based on how ions are formed and focused. The DC sputtering process applies a positive voltage to the substrate and a negative voltage to the target material. Argon, or any other inert gas, is added once the necessary vacuum level has been reached. Vibrant electrons clash with the gas to produce ions due to the strong electric field created between the electrodes. These ions cause

nanoclusters to sputter and deposit on the substrate when they come into contact with the target material [24,27,29]. The radio frequency (RF) sputtering method, on the other hand, is usually used when the target is insulating or close to insulating materials and it uses a high frequency, typically 13.56 MHz, to sufficiently ionize the gas [29]. With the magnetron sputtering technique, the ionization effect and ion concentration toward the target material are enhanced by applying a magnetic field concurrently with the electric field produced by DC/RF sputtering [29,30]. In this project, a Pt counter electrode was fabricated using the Cressington 108 Auto Sputter Coater. The Pt counter electrode was subsequently used for comparative studies.

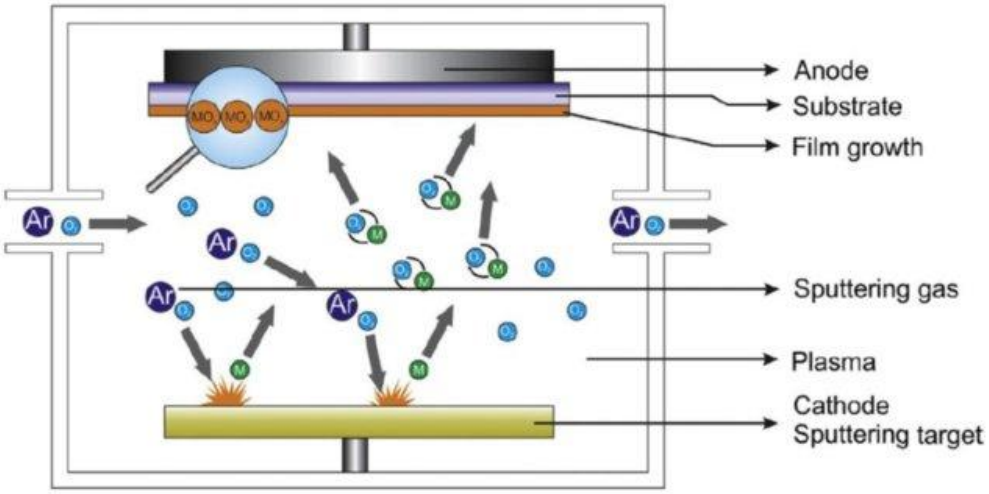

Figure 2.7: Schematic diagram demonstrating the principle of sputtering method for nanoparticle formation [32].

2.3.2. Bottom-up methods

Bottom-up methods rely on natural or controlled processes such as chemical reactions, self-assembly, or molecular deposition to form desired materials. Bottom-up approaches are widely used in nanotechnology and materials science due to their ability to produce highly uniform and precise structures with tailored properties. The sol-gel method and colloidal synthesis are among the top-down synthesis methods.

2.3.2.1. Sol-gel

The sol-gel method is utilized to synthesize various nanomaterials, especially metal oxide nanoparticles [33]. This process begins with the dissolution and conversion of

monomers, or the starting material, into a sol, i.e., a colloidal solution, which serves as the precursor for the subsequent gel formation. After that, the sol is heated and stirred via hydrolysis and alcohololysis reactions to turn it into gel [34,35]. The hydrolysis process produces a moist gel, therefore depending on its intended use and desired characteristics, it must be dried appropriately [36]. The resulting gels are powdered and then calcined following the drying phase. The sol-gel approach is thought to be particularly beneficial because it achieves a consistent nanostructure at low temperatures [34]. There are five steps in the sol-gel process: hydrolysis, condensation, aging, drying and calcination.

Stage 1: Hydrolysis

In this stage, a precursor which is made up of an aqueous solution of the metal alkoxide (M–OR) uses the hydrolysis process in equation 2.1 to react with the surrounding water to generate a colloidal suspension (sol) of the metal hydroxide (M–OH) [37]:

$$M–OR + H–OH = M–OH + R–OH \qquad (2.1)$$

Stage 2: Condensation

When a solvent (such as water or alcohol) is removed to create a sol, a polymer network consisting of metal oxide connections is formed. This process is referred to as the gelation or condensation stage. As the polymer network expands, this process causes the solution's viscosity to increase, creating a porous structure within the liquid phase (sol-gel) [36,37]. A condensation reaction that releases a molecule of water or alcohol is expressed by equation 2.2.

$$M–OH + M–OR = M–O–M + R–OH \;/\; M–OH + M–OH = M–O–M + H–OH \qquad (2.2)$$

Step 3 and 4: Aging and drying

The aging stage sees the condensation reactions continue, finishing the gel's production. During the drying phase, water and other liquids trapped in the gel structure's pores are released during the drying phase.

Stage 5: Calcination

All the volatile organics are eliminated during this final stage, which involves dehydrating the dry gel structure to induce further crystallization.

2.3.2.2. Colloidal synthesis

One of the most flexible techniques for synthesizing quaternary nanoparticles is colloidal synthesis, which modifies a variety of reaction parameters to regulate the size and shape of the resulting nanoparticles. These parameters include reaction time, temperature, capping agents, and metal salt precursors. There are two primary types of colloidal methods: non-injection and hot-injection. Hot-injection methods involve injecting a hot solution of precursors into a cold solution of solvents and surfactants, creating a temperature gradient that initiates the nucleation and growth of quantum dots. Non-injection methods do not require the injection of precursors but rather rely on the thermal decomposition or reduction of precursors in a single solution of solvents and surfactants. Examining the nucleation and growth processes involved in nanoparticle formation is crucial to completely understanding the colloidal synthesis pathway.

2.3.2.2.1. Nucleation

The process of nucleation involves the use of nuclei, or seeds, as templates for other particles to agglomerate together and produce crystal growths [38]. Most theoretical work on nucleation using equilibrium thermodynamics is based on the classical nucleation theory (CNT) that was created more than 70 years ago by Becker and Döring [39]. A thermodynamic system seeks to raise its overall entropy and decrease its Gibbs free energy, according to the CNT [39]. When nuclei form consistently throughout the parent phase, this is known as homogeneous nucleation [38]. Additionally, this kind of nucleation requires a supercritical condition, such a supersaturation, and occurs spontaneously [39,40]. The total free energy of the nanoparticle can be used to provide a thermodynamic description of the formation of homogenous nuclei. The particle's spherical shape was used to explain the nucleation process. In this instance, the nucleation rate for a spherical particle might be described by the total Gibbs free energy, which is the free energy needed to stabilize nuclei without dissolving in the solution [40]. It is the total of two free energies: the surface free energy (ΔG_s) (which is between the surface particle and the bulk particle) and the

bulk-free energy (ΔG_v) (which is the free energy between large-size particles and the solute in solution) [40]. Additionally, as one approaches the supersaturated state, ΔG_s is a positive value proportional to r^2 (radius of the particle) and ΔG_v is a negative value proportional to r^3 [40]. Thus, the Gibbs free energy (G) for a spherical particle of radius r, surface energy (γ), and bulk free energy of the crystal (ΔG_v) can be stated as follows:

$$G = \Delta G_s + \Delta G_v = 4\pi^2 + \frac{4}{3}\pi r^3 \Delta G_v \quad (2.3)$$

ΔG_v is dependent upon the supersaturation of the solution (S), its molar volume (V_m), Boltzmann's constant (k_B) and temperature (T) as shown in equation 2.4

$$\Delta G_v = \frac{-k_B T\, ln(S)}{V_m} \quad (2.4)$$

Figure 2.8 plots the Gibbs free energy vs the radius, illustrating how the Gibbs bulk free energy affects the negative term, and the surface energy affects the positive term.

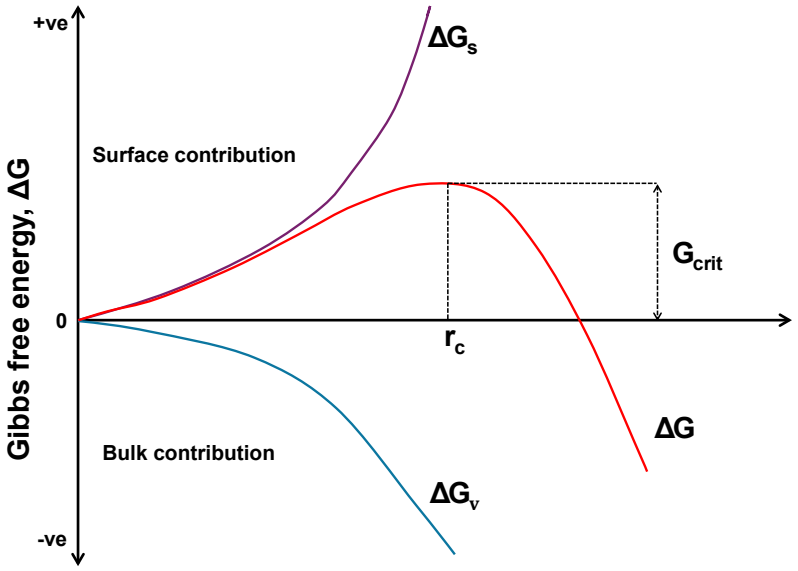

Figure 2.8: A graph showing the Gibbs free energy in relation to the clusters' radius.

The figure additionally shows that there is a critical cluster radius, denoted as r_c, at which a maximum Gibbs energy is present. The activation energy (G_{crit}), which is the corresponding energy barrier, is the minimum radius at which a particle stays stable in solution [39–41]. A cluster of particles is unstable and will dissolve again in solution if its radius is less than r_c. In contrast, the particle cluster is stable, and growth is encouraged if the cluster's radius is greater than r_c [38–41]. This means that the critical

radius (r_c) can be thought of as the lowest radius at which a nucleus can remain in the solution and keep growing [40].

The critical radius is given as:

$$r_c = \frac{2}{\Delta G_v} \tag{2.5}$$

While the activation energy is given as:

$$\Delta G_{crit} = \frac{16\pi\gamma^3}{\Delta G_v{}^2} \tag{2.6}$$

The Arrhenius equation can be used to express the nucleation rate for N particles at time t. Since the activation energy acts as the energy barrier for nucleation, nucleation is seen as a statistical process, and the nucleation rate dN/dt can be stated using the following equation.

$$\frac{dN}{dt} = Ae^{(\frac{\Delta G_{crit}}{k_B T})} \tag{2.7}$$

2.3.2.2.1.1. LaMer's nucleation theory

LaMer and Dinegar proposed the idea of burst nucleation in 1950 and applied the CNT to the creation of colloidal nanocrystals in a solution phase [42]. Nucleation is separated, and then growth occurs, according to the burst nucleation hypothesis. Moreover, because of homogeneous nucleation, nuclei are produced simultaneously during the burst nucleation process and eventually grow without further nucleation after that [39,42]. LaMer's nucleation model can be divided into three stages as illustrated in Figure 2.9. First, the precursor must undergo decomposition in order for monomer to develop. The concentration of monomer then rises until it reaches a point of supersaturation (C_s). In the second stage, saturation keeps rising until it reaches a point (C_{min}) where self-nucleation or burst nucleation can occur because the energy barrier (activation energy) for nucleation has been overcome. The concentration of free monomers in solution is dramatically reduced because of burst nucleation in the third stage, reaching below the minimum supersaturation level, at which point no further nucleation takes place. During this stage, the nuclei start to develop, and the monomers diffuse to the nucleation site.

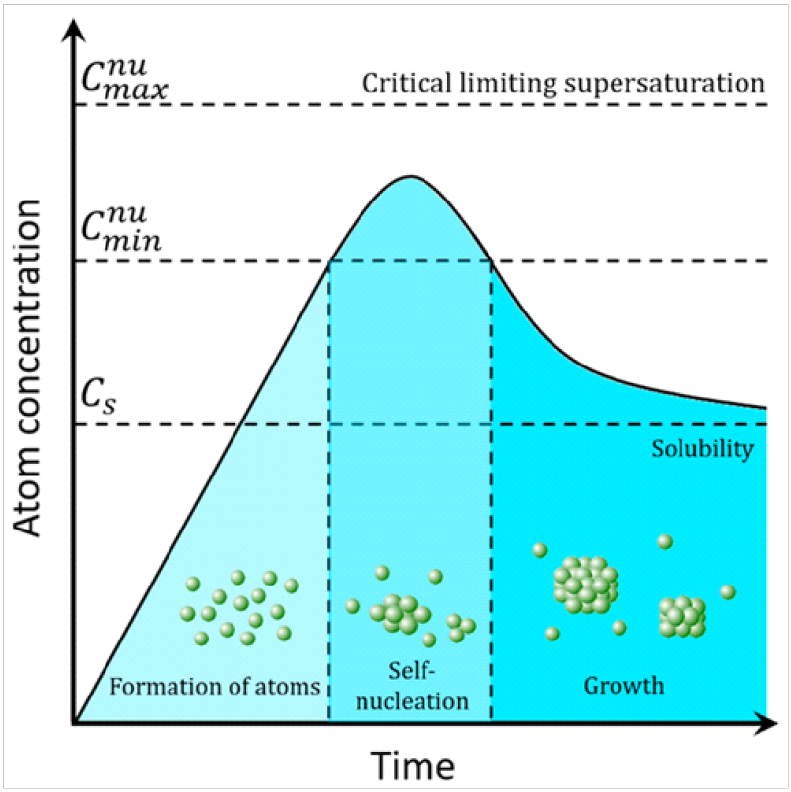

Figure 2.9: LaMer's nucleation and growth model [43].

2.3.2.2.2. Growth

Atoms are added to the developing crystal as the development stage progresses. Another model that has been applied to clarify the mechanism of particle growth in a precursor solution is Oswald ripening [40]. Oswald ripening is a growth process that promotes the growth of large particles by causing smaller crystals in solution to redissolve and deposit on their surface. Nucleation and growth steps can be considered to occur simultaneously as described by the Finke-Watzky mechanism [38]. Equation 2.8 describes the gradual continuous nucleation that occurs in the first step, and equation 2.9 describes the autocatalytic surface growth that occurs in the second step without diffusion control.

$$A \rightarrow B \tag{2.8}$$

$$A + B \rightarrow 2B \tag{2.9}$$

2.4. Dye sensitized solar cell

In the quest for sustainable energy solutions, dye sensitized solar cells (DSSCs) have come out as a promising technology with the potential to revolutionize the field of photovoltaics. Unlike traditional silicon-based solar cells, DSSCs employ a unique design inspired by natural photosynthesis, utilizing light-absorbing dyes to convert sunlight into electricity. The sandwich structure of a DSSC is made up of 3 major components: the electrolyte solution (usually a triiodide solution), a dye sensitized photoanode and a Pt-based counter electrode as shown in Figure 2.10. Since the discovery of DSSCs by O`Regan and Gräzel in 1991 which resulted in approximately 7% simulated light to electric energy conversion and approximately 12% in diffuse light, scientists have since been trying to optimize various parameters of each component of DSSCs [44]. However, there are various components which hinder the commercialization of DSSC devices. The limitations of each component are further discussed below.

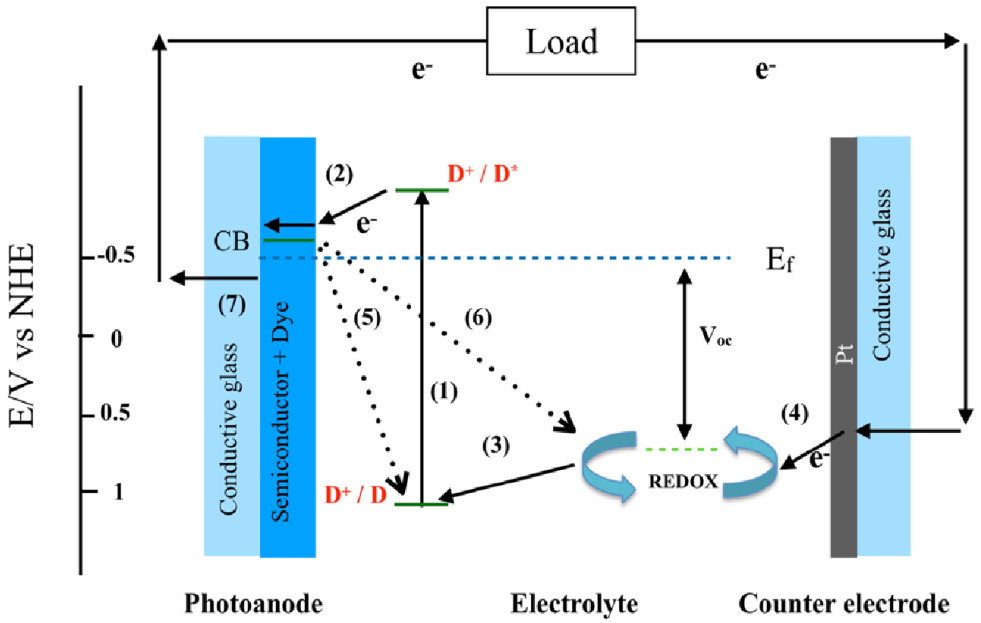

Figure 2.10: A simplified diagram illustrating the fundamental components of a DSSC (refer to section 2.4.4. for details about reaction process 1 to 6) [45].

2.4.1. Electrolyte

The electrolyte comprises of the redox couple, which is an essential component as it allows the electrolyte to transport charges between the photoanode and the counter electrode for regeneration of the dye during the operation of a DSSC [46,47]. The selection of the electrolyte (i.e., solid-state, quasi-solid state and/or liquid state) significantly influences the stable operation and maximum efficiency of the cell, as it directly impacts the mass transportation of charge carriers within the electrolyte through diffusion processes [45,46]. According to Rondán-Gómez *et al.*, liquid state electrolytes are extensively used in DSSCs due to their ability to achieve remarkable efficiency levels, typically around 13% [45]. This efficiency is presently considered the highest among traditional DSSCs. Therefore, liquid electrolytes that incorporate an iodide/triiodide (I^-/I_3^-) redox couple are extensively researched in DSSCs due to their inherent photovoltaic properties, which have the potential to enhance DSSC efficiency.

2.4.2. Counter electrode

The counter electrode component of a DSSC plays a crucial role in facilitating the catalytic reaction that leads to the reduction of the electrolyte solution. Through effective electron collection from the external circuit, it significantly enhances the performance of DSSCs [14,47–49]. To date, the most conventional counter electrode consists of a Pt coating on a conductive substrate. This substrate has superior electrocatalytic activity, high conductivity, and remarkable stability for the reduction of charge carriers in a triiodide electrolyte [14,48,50]. However, Pt easily corrodes by the frequently used triiodide electrolyte and results in the formation of PtI_4 which hinders the efficiency of the DSSC. Consequently, Pt is a precious metal which increases the cost of the fabrication of DSSC thus limiting the usage of DSSCs for large-scale commercial applications [14,48–50].

2.4.3. Photoanode

The photoanode is made up of a wide band gap metal oxide semiconductor (i.e., titanium dioxide, zinc oxide, tin dioxide) sensitized with a ruthenium dye that is coated on a conductive glass substrate such as indium-doped tin oxide (ITO) or fluorine-

doped tin oxide (FTO). It is worth noting that photoanodes have two main functions which are to adsorb the dye and transport the photo-excited electrons from the dye to the external circuit [51,52]. For maximum adsorption of the dye, the photoanode must have a large surface area for fast transmittance of the photo-excited electrons [52]. To ensure a high electron collection efficiency in the cell or DSSC, it is essential to have a rapid charge transport rate [51]. Among the various metal oxide semiconductors, titanium dioxide (TiO_2) is the extensively used semiconductor material in the fabrication of a photoanode. This is due to its attractive properties of being stable and having improved photovoltaic characteristics [53,54]. TiO_2 semiconductors have a large surface area of approximately 50 m^2/g which enables the material to have a strong ability to adsorb the dye and transfer electrons [51,52]. However, the efficiency of DSSCs is greatly hindered by the high recombination losses and low electron mobility properties exhibited by TiO_2, thereby posing limitations on its overall performance [53]. Intensive investigations have been conducted to reduce the recombination losses and improve electron transfer of TiO_2 nanoparticles through the doping of TiO_2 with non-metal and metal ions and combining TiO_2 with different nanocomposites such as carbon nanotubes [54,55].

2.4.4. Working principle of a DSSC

The dye molecules in DSSCs function as molecular electron pumps whenever they absorb light [47]. Electrons transition between two molecular orbitals based on their ground or excited state. The lowest orbital is known as the lowest unoccupied molecular orbital (LUMO), while the highest orbital is known as the highest occupied molecular orbital (HOMO). When visible light is introduced to the cell, the photons of light are absorbed by the dye (D) molecules which generate excited electrons (D*) from the LUMO level in the ground state to HOMO level in the excited state followed by the dye (reaction 1) [45,47]. The excited electron is subsequently moved to the conduction band of the TiO_2 semiconductor (reaction 2). The dye remains in its oxidised state (D^+) and then receives electrons from the triiodide electrolyte redox couple (I^-/I_3^-). This process returns the dye to its ground state (D) and enables the continuous generation of excited electrons (reaction 3) [45]. The counter electrode then donates its electrons to the electrolyte redox couple so that it can return to its

ground state (reaction 4) [56]. In reaction 5, the oxidized dye (D^+) captures the electrons in the TiO_2 film, leading to dye recombination. Similarly, in reaction 6, the electrons in the TiO_2 film are captured by the electrolyte of the redox couple, resulting in electrolyte recombination [47]. Based on the working principle, thorough investigation is required to characterize the DSSC device.

Chemical reactions within DSSC following photo-absorption (refer to Figure 2.10):

$$D \xrightarrow{\text{photo-excitation}} D^* \qquad \text{reaction 1}$$

$$D^* \xrightarrow{\text{electron injection}} D^+ + e^- \qquad \text{reaction 2}$$

$$2D^+ + 3I^- \xrightarrow{\text{dye regeneration}} 2D + I_3^- \qquad \text{reaction 3}$$

$$I_3^- + 2e^- \xrightarrow{\text{electrolyte regeneration}} 3I^- \qquad \text{reaction 4}$$

Recombination reactions

$$D^+ + e^- \xrightarrow{\text{dye recombination}} D \qquad \text{reaction 5}$$

$$I_3^- + e^- \xrightarrow{\text{electrolyte recombination}} 3I^- \qquad \text{reaction 6}$$

2.5. Characterization of the counter electrodes of DSSCs

Numerous characterization techniques have been developed to obtain a comprehensive understanding of the relative reaction process mechanisms, including charge generation, transfer, and recombination occurring at the counter electrode, and to design new materials that improve the photovoltaic performance of the DSSCs [57]. To examine the process mechanisms, analyse component interactions, and assess the performance of the DSSCs, atomic force microscopy (AFM), electrochemical and photoelectrochemical techniques such as Tafel polarization, cyclic voltammetry (CV), electrochemical impedance spectroscopy (EIS), and current–voltage (I–V) characterization have been identified as the most effective methods. This section of the dissertation introduces the characterization techniques used in this research project, highlighting the diverse instruments used to analyse materials synthesized across various research fields.

2.5.1. Atomic force microscopy

AFM is a versatile technique capable of imaging nearly any surface, making it particularly effective for obtaining valuable insights into the characterization of thin films and coatings. Information on the surface topology and roughness of the fabricated thin films is obtained in this work using AFM. This technique is highly effective for surface roughness measurements because it can quantitatively assess the x, y, and z dimensions with nanoscale precision.

2.5.1.1. Principle of AFM

An AFM comprises of four main components (Figure 2.11), starting with the cantilever that has a sharp tip. A reflective coating on the cantilever's back enables it to reflect light like a mirror. The second component is the laser beam and photodetector, where the laser beam is directed onto the cantilever's back, and the reflected light is detected by a photodetector that is highly sensitive to the laser's position. The cantilever, laser, and detector system are precisely controlled and scanned using the third component which is the piezoelectric scanner, while the sample, placed on a translation stage beneath the microscope, can also be moved. The fourth component is the feedback control system, which regulates a consistent force between the tip and the sample by modifying the cantilever’s height to provide precise and steady imaging.

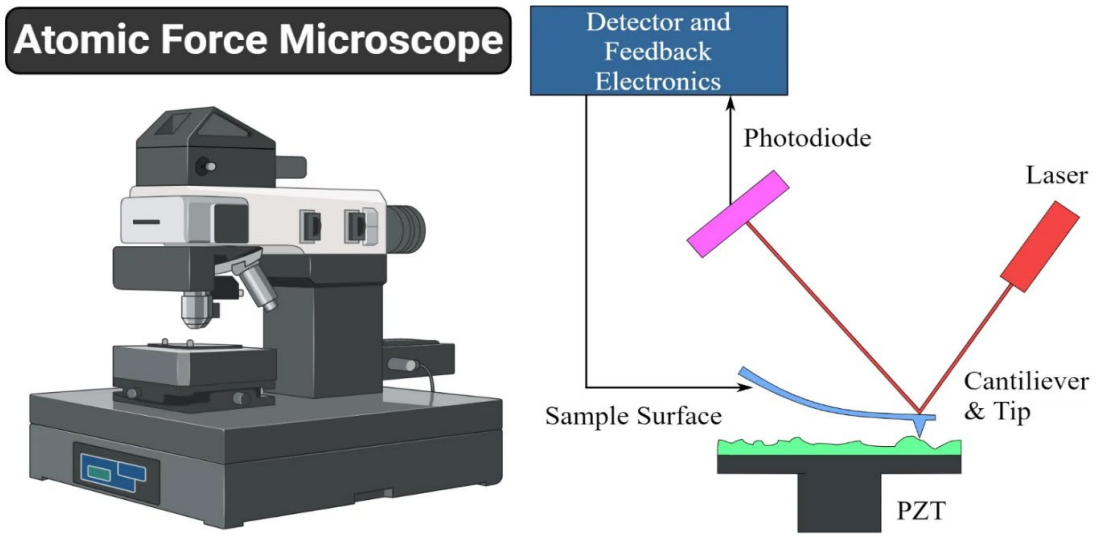

Figure 2.11: Schematic illustrations showing the operation principle of AFM [75].

When the cantilever's tip, which is connected to its free end, approaches the surface closely, attractive and repulsive forces arising from the interactions between the tip and the surface of the sample causes the cantilever to bend either positively or negatively. The laser beam is used to detect this bending. The cantilever can be considered as a spring, and the magnitude of the force produced between the tip and the surface depends on the spring constant (stiffness) of the cantilever and the distance between the tip and the surface [73-75]. This force can be described using Hooke's Law, as shown by the following equation:

$$F = -k \cdot x \tag{2.10}$$

Where: F is the force, k is the spring constant and x is the distance of the cantilever deflection. If the cantilever's spring constant is lower than that of the surface, bending occurs, and this deflection is monitored. As the tip moves across the sample, it fluctuates up and down based on the surface properties of the sample (e.g., topography). Electrostatic, magnetic, capillary, and Van der Waals interactions between the tip and the sample are the sources of these fluctuations. In order to generate a topographical image, the tip's displacement is measured [73-75].

2.5.2. Cyclic voltammetry

Cyclic voltammetry (CV) is a technique used for investigating the counter electrodes' electrocatalytic activity in relation to the reduction of the triiodide electrolyte [58]. The counter electrode, reference electrode (RE) and working electrode (WE) are the three electrodes that are typically used in CV analysis. During analysis, the potential undergoes a consistent sweep rate, reversing at a designated point, with continuous monitoring of the current. Potential measurements occur between the WE and the RE, while current measurement takes place between the WE and the counter electrode [57]. A typical cyclic voltammogram of a counter electrode is shown in Figure 2.12, along with all the important data that can be extracted from it. The peak current density (i_p) and the peak-to-peak potential difference (ΔE_{pp}) are two significant parameters from the CV analysis that characterize the electrocatalytic capabilities of a counter electrode [59]. The most important factor in a DSSC's operation is the reduction of the triiodide ions. Reaction 2.11 represents the reduction reaction, where the negative

current cathodic peak (I_{pc}) is associated with it, and reaction 2.12 represents the oxidation reaction, where the positive current anodic peak (I_{pa}) is associated to it.

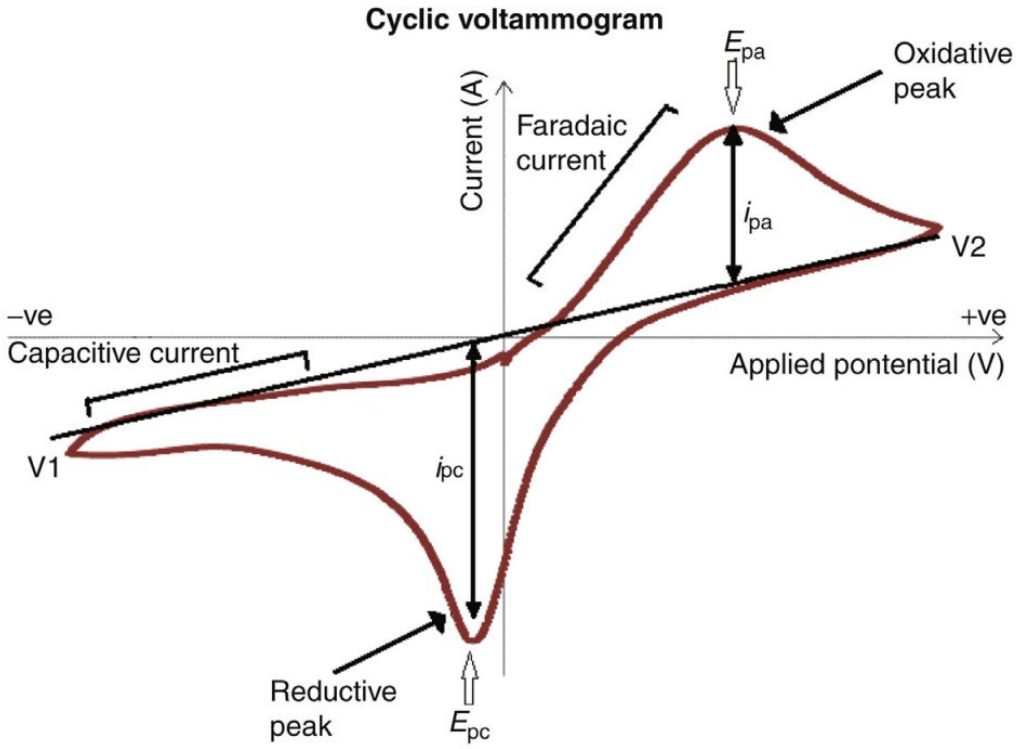

Figure 2.12: The peak cathodic potential (E_{pc}), peak anodic potential (E_{pa}), and peak current density (i_p) are highlighted in this schematic illustration of a cyclic voltammogram [60].

$$I_3^- + 2e^- \leftrightarrow 3I^- \quad (2.11)$$

$$3I_2 + 2e^- \leftrightarrow 2I_3^- \quad (2.12)$$

The rate at which the catalyst converts I_3^- ions to I^- ions is indicated by the cathodic peak current density (i_{pc}). Greater electrocatalytic ability of the catalytic material is generally implied by a larger cathodic peak current density. However, information regarding the reversibility of the redox process is provided by the ΔE_{pp}. Thus, a higher electrocatalytic activity is indicated by a smaller ΔE_{pp}, which results in a faster redox reaction [57]. The morphology, surface area and composition of the counter electrode materials influence the I_p and E_{pp} parameters. Evaluating the stability of the counter electrode material involves conducting multiple cycles of CV analysis. Variations in the CV curve characteristics are subsequently employed to evaluate the stability of different counter electrode materials.

2.5.3. Electrochemical impedance spectroscopy

The electron-hole recombination and charge transfer kinetics, as well as the electrocatalytic activity of the counter electrodes in DSSCs, are studied using the electrochemical impedance spectroscopy (EIS) technique [57,61]. In this analysis, two identical electrodes with cathode and anode capabilities make up a symmetric cell, on which EIS measurements are carried out [58]. With this method, the working electrode of an electrochemical cell is subjected to a small sinusoidal potential and the current response that results is measured [60,62]. The electrochemical characteristics of a system can be examined by obtaining the electrochemical parameters such as series resistance (R_S), charge transfer resistance (R_{CT}), diffusion resistance (Z_W), and double layer capacitance (C_{dl}) from the equivalent circuit, which is fitted with the measured data using a software. Nyquist and Bode plots are commonly used to display the results of EIS studies [57,63]. A typical example of the Nyquist plot is shown in Figure 2.13. The starting point of the plot is the R_S, mainly caused by the conductive substrate [63]. The R_{CT} at the interface between the electrode and electrolyte is represented by the radius of the semicircle. For the reduction of the triiodide redox couple at the counter electrode's catalytic surfaces, a lower R_{CT} value indicates significant electron transfer from the counter electrode to the electrolyte [64].

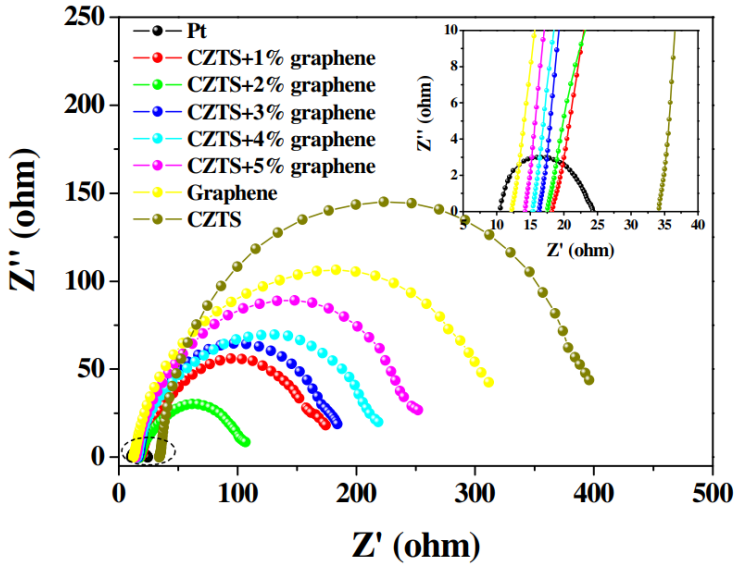

Figure 2.13: Nyquist curves derived from symmetric dummy cells composed of Pt (*insert*), CZTS and varying weight percentages of graphene with CZTS [65].

2.5.4. Tafel polarization

To confirm the electrocatalytic activities and interfacial charge-transfer characteristics of the counter electrode, Tafel polarization studies are utilized [63]. The Tafel plot shows the logarithmic current density (log *J*) as a function of the applied potential (V) as shown in Figure 2.14. The Tafel plot yields two critical parameters: the limiting diffusion current density (J_{lim}) and the exchange current density (J_0), which are used to assess the catalytic activity of an electrocatalytic film.

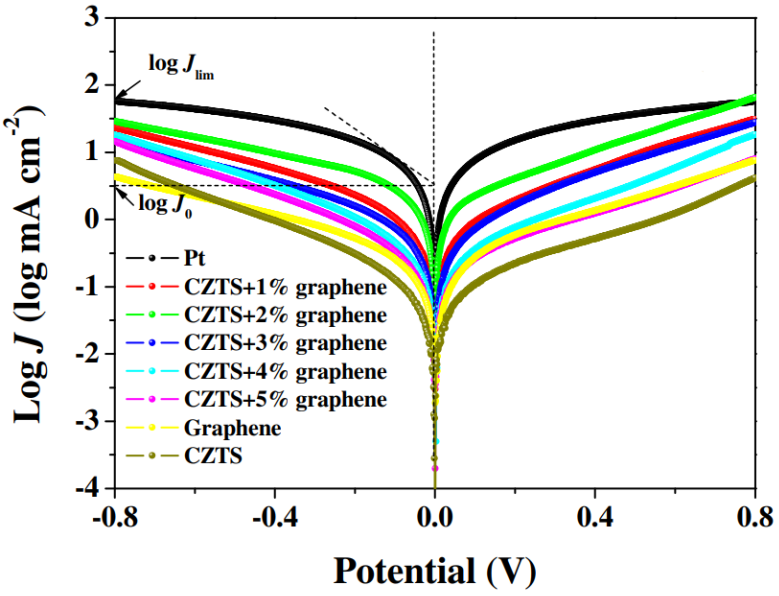

Figure 2.14: Tafel polarization plot derived from symmetric dummy cells composed of Pt, CZTS and varying weight percentages of graphene with CZTS [65].

According to equation 2.13, the exchange current density depends on the charge transfer resistance.

$$J_o = \frac{RT}{nFR_{CT}} \qquad (2.13)$$

where T is the temperature, n is the number of electrons involved in the reaction, F is the Faraday constant, and R is the gas constant [65,66]. Because of the inverse relationship between J_0 and R_{CT} shown in equation 2.13, a higher J_0 value indicates significantly higher catalytic activity. The current density in DSSCs that is limited by transfer resistance is determined by the diffusion of ionic carriers in the electrolyte between different electrodes. The ion diffusion rate between two counter electrodes can be measured by adjusting this measurement [66]. There is a linear relationship

between the J_{lim} obtained from the Tafel diagram and the diffusion coefficient (D_n) of the redox couple according to equation 2.14. Therefore, a higher J_{lim} value means larger D_n value, indicating better electrocatalytic activity where C is the electrolyte concentration and l is the spacer's thickness [63,65–67].

$$J_{lim} = \frac{2nFCD_n}{l} \tag{2.14}$$

2.5.5. Current voltage measurements

Finding the current and potential of the cell using an external variable resistance at a specific incoming light intensity is the fundamental measurement needed to assess the efficiency of a DSSC [68]. Thus, the primary purpose of current voltage (I-V) measurements is to determine the DSSC's electrical output power under standard light conditions [69]. The I-V curve, as seen in Figure 2.15, makes it easy to get four crucial DSSC parameters: power conversion efficiency (PCE, η), fill factor (FF), open circuit voltage (V_{oc}), and short-circuit current (I_{sc}). The highest voltage that can be measured in the absence of current flow is known as the V_{oc}, and it represents the energy differential between the semiconductor's Fermi level and the redox energy level of the redox pair [68,69]. The highest current production of a solar cell is known as the I_{sc}, and it is measured when the applied voltage across the solar cell is zero or when the solar cell is short-circuited [69]. The voltage and current density are multiplied to determine the cell's power per unit area, which peaks at a specific point on the J-V curve. Maximum power output (P_{max}) is the name given to this point at which power reaches its maximum, while maximum current density (I_m) and voltage (V_m) are the matching current and voltage values. The ratio of a cell's maximum power (P_{max}) to the product of its open circuit voltage (V_{oc}) and short circuit current density (J_{sc}) is known as its fill factor (FF). The efficiency (η) of the cell is determined by dividing the maximum power (P_{max}) by the total intensity of the incident light (P_{in} = $100\ \mathrm{mW.cm^{-2}}$). Equations 2.15 and 2.16 provide the relationship between η and FF [17,69,70].

$$\eta = \frac{P_{max}}{P_{in}} = \frac{V_{oc} \times I_{sc} \times FF}{P_{in}} \times 100\% \tag{2.15}$$

$$FF = \frac{P_{max}}{V_{oc} \times J_{sc}} = \frac{I_m \times V_m}{V_{oc} \times I_{sc}} \tag{2.16}$$

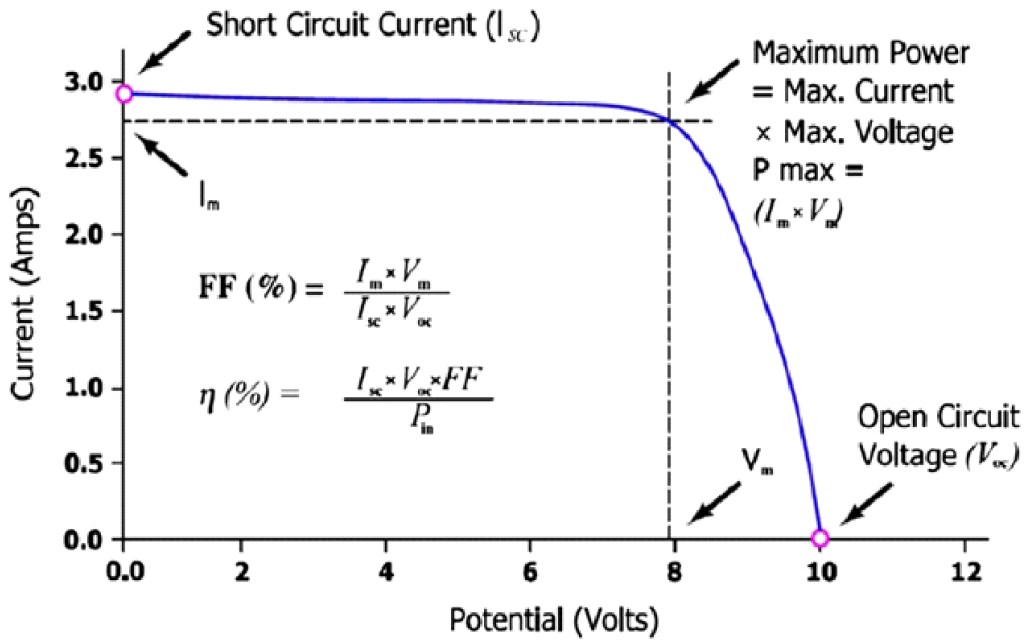

Figure 2.15: Typical I-V curve obtained from photocurrent-voltage measurement [69].

In conclusion, over the years the exploration of various materials for counter electrodes in DDSCs have revealed significant advancements in enhancing the efficiency and stability of these devices. The reviewed literature highlights the potential of alternative materials such as Cu-based and metal alkali-based quaternary semiconductors to replace the conventional Pt counter electrode. These materials not only offer cost-effective solutions but also exhibit promising catalytic properties. However, challenges such as optimizing the synthesis methods and improving the overall performance of these materials remain. Future research should focus addressing these issues and to further advance the field of DSSCs. This review underscores the importance of continued innovation in developing sustainable and efficient solar energy technologies.

2.6. References

[1] Hossain, N.; Mobarak, M. H.; Mimona, M. A.; Islam, M.; Hossain, A.; Zohura, F.; Chowdhury, M. Advances and Significances of Nanoparticles in Semiconductor Applications -A Review. *Results in Engineering* **2023**.

[2] Mathuri, S.; Zhu, Y.; Margoni, M. M.; Li, X. Semiconducting Nanoparticles: Single Entity Electrochemistry and Photoelectrochemistry. *Front Chem* **2021**, *9*, 688320.

[3] Ishtiaq, M.; al-Rashida, M.; Alharthy, R. D.; Hameed, A. Chapter 15 - Ionic Liquid–Based Colloidal Nanoparticles: Applications in Organic Synthesis. In *Metal Nanoparticles for Drug Delivery and Diagnostic Applications*; Shah, M. R., Imran, M., Ullah, S., Eds.; Elsevier, **2020**; pp 279–299.

[4] Lim, J.; Bae, W. K.; Kwak, J.; Lee, S.; Lee, C.; Char, K. Perspective on Synthesis, Device Structures, and Printing Processes for Quantum Dot Displays. *Optical Materials Express* **2012**, *2*, 594–628.

[5] Chang, J.; Waclawik, E. R. Colloidal Semiconductor Nanocrystals: Controlled Synthesis and Surface Chemistry in Organic Media. *RSC Adv.* **2014**, *4* (45), 23505–23527.

[6] Tallapally, V. Colloidal Synthesis and Photophysical Characterization of Group IV Alloy and Group IV- V Semiconductors: Ge1-xSnx and Sn-P Quantum Dots. PhD Thesis, **2018**.

[7] Gopal, R.; Kathirgamanathan, P.; Ravi, G.; Elangovan, T.; Kumar, B.; Manivannan, N.; Kasinathan, K.; Arjun Kumar, B. Quantum Confinement Effect of 2D Nanomaterials; **2020**.

[8] Zaini, M. S.; Ying Chyi Liew, J.; Alang Ahmad, S. A.; Mohmad, A. R.; Kamarudin, M. A. Quantum Confinement Effect and Photoenhancement of Photoluminescence of PbS and PbS/MnS Quantum Dots. *Applied Sciences* **2020**, *10* (18).

[9] Rabouw, F.; Donega, C. Excited-State Dynamics in Colloidal Semiconductor Nanocrystals. *Topics in Current Chemistry* **2016**, *374*.

[10] Jagtap, S.; Chopade, P.; Tadepalli, S.; Bhalerao-Pawar, A.; Gosavi, S. A Review on the Progress of ZnSe as Inorganic Scintillator. *Opto-Electronics Review* **2019**, *27*, 90–103.

[11] Kush, P.; Deka, S. Multifunctional Copper-Based Quaternary Chalcogenide Semiconductors Toward State-of-the-Art Energy Applications. *ChemNanoMat* **2019**, *5* (4), 373–402.

[12] Zheng, X.-L.; Yang, Y.-J.; Liu, Y.-H.; Deng, P.-L.; Li, J.; Liu, W.-F.; Rao, P.; Jia, C.-M.; Huang, W.; Du, Y.-L.; Shen, Y.-J.; Tian, X.-L. Fundamentals and Photocatalytic Hydrogen Evolution Applications of Quaternary Chalcogenide Semiconductor: Cu_2ZnSnS_4. *Rare Metals* **2022**, *41* (7), 2153–2168.

[13] Liu, W.; Li, H.; Qiao, B.; Zhao, S.; Xu, Z.; Song, D. Highly Efficient CIGS Solar Cells Based on a New CIGS Bandgap Gradient Design Characterized by Numerical Simulation. *Solar Energy* **2022**, *233*, 337–344.

[14] Imla Mary, C.; Senthilkumar, M.; Manobalaji, G.; Moorthy Babu, S. Solution Processed Cu_2ZnSnS_4 Nanoink for Inexpensive Pt-Free Counter Electrode in Dye-Sensitized Solar Cells. *Solid State Sciences* **2021**, *116*, 106612.

[15] Kolokoto, T.; Mashindi, V.; Kadzutu-Sithole, R.; Machogo-Phao, L. F. E.; Ndala, Z. B.; Shumbula, N. P.; Nkabinde, S. S.; Ngubeni, G. N.; Gqoba, S. S.; Mubiayi, K. P.; Moloto, N. The Effect of the Metal and Selenium Precursors on the Properties of $NbSe_2$ and Nb_2Se_9 Nanostructures and Their Application in Dye-Sensitized Solar Cells. *RSC Adv.* **2021**, *11* (50), 31159–31173.

[16] Abusnina, M. Synthesis and Characterization of Kesterite Cu_2ZnSnS_4 (CZTS) Thin Films for Solar Cell Application; **2016**.

[17] Sun, K.; Liu, F.; Hao, X. *Kesterite $Cu_2ZnSnS_{4-x}Se_x$ Thin Film Solar Cells*; IntechOpen, **2021**.

[18] Dimitrievska, M.; Boero, F.; Litvinchuk, A. P.; Delsante, S.; Borzone, G.; Perez-Rodriguez, A.; Izquierdo-Roca, V. Structural Polymorphism in “Kesterite” Cu_2ZnSnS_4: Raman Spectroscopy and First-Principles Calculations Analysis. *Inorganic Chemistry* **2017**, *56* (6).

[19] Yu, K.; Carter, E. A. A Strategy to Stabilize Kesterite CZTS for High-Performance Solar Cells. *Chem. Mater.* **2015**, *27* (8), 2920–2927.

[20] Kumar, M.; Dubey, A.; Adhikari, N.; Venkatesan, S.; Qiao, Q. Strategic Review of Secondary Phases, Defects and Defect-Complexes in Kesterite CZTS–Se Solar Cells. *Energy & Environmental Science* **2015**, *8*.

[21] Hages, C. J.; Koeper, M. J.; Agrawal, R. Optoelectronic and Material Properties of Nanocrystal-Based CZTSe Absorbers with Ag-Alloying. *Solar Energy Materials and Solar Cells* **2016**, *145*, 342–348.

[22] Messaoudi, O.; Bendahou, M. Biological Synthesis of Nanoparticles Using Endophytic Microorganisms: Current Development. In *Nanotechnology and the Environment*; Sen, M., Ed.; IntechOpen: Rijeka, **2020**.

[23] Shyam, A.; Chandran, S.; George, B. Plant Mediated Synthesis of AgNPs and Its Applications: An Overview Plant Mediated Synthesis of AgNPs and Its Applications: An Overview. *Inorganic and Nano-Metal Chemistry* **2020**, *51*.

[24] Baig, N.; Kammakakam, I.; Falath, W. Nanomaterials: A Review of Synthesis, Properties, Recent Progress, and Challenges. *Materials Advances* **2021**, *2*.

[25] Ahmad, F.; Ashraf, N.; Ashraf, T.; Zhou, R.-B.; Yin, D.-C. Biological Synthesis of Metallic Nanoparticles (MNPs) by Plants and Microbes: Their Cellular Uptake, Biocompatibility, and Biomedical Applications. *Applied Microbiology and Biotechnology* **2019**, *103*.

[26] Pieła, A.; Klimek-Ochab, M. Fungal Synthesis of Size-Defined Nanoparticles. *Advances in Natural Sciences: Nanoscience and Nanotechnology* **2017**, *8*, 043001.

[27] Abid, N.; Khan, A. M.; Shujait, S.; Chaudhary, K.; Ikram, M.; Imran, M.; Haider, J.; Khan, M.; Khan, Q.; Maqbool, M. Synthesis of Nanomaterials Using Various Top-down and Bottom-up Approaches, Influencing Factors, Advantages, and Disadvantages: A Review. *Advances in Colloid and Interface Science* **2022**, *300*, 102597.

[28] Dhand, C.; Dwivedi, N.; Loh, X. J.; Jie Ying, A. N.; Verma, N. K.; Beuerman, R. W.; Lakshminarayanan, R.; Ramakrishna, S. Methods and Strategies for the Synthesis of Diverse Nanoparticles and Their Applications: A Comprehensive Overview. *RSC Adv.* **2015**, *5* (127), 105003–105037.

[29] Kumar, D. S.; Kumar, B. J.; Mahesh, H. M. Chapter 3 - Quantum Nanostructures (QDs): An Overview. In *Synthesis of Inorganic Nanomaterials*; Bhagyaraj, S. M., Oluwafemi, O. S., Kalarikkal, N., Thomas, S., Eds.; Micro and Nano Technologies; Woodhead Publishing, 2018; pp 59–88.

[30] Braun, M. Magnetron Sputtering Technique; **2015**; pp 2929–2957.

[31] Barizão, A.; Oliveira, J.; Gonçalves, R.; Cassini, S.; Cassini, T. Keywords Nanomaterials; . Nanoparticles; . Magnetism; . Iron Oxide; . Synthesis Route. **2021**.

[32] Abdullah, H.; Al-Amiery, A.; Al-Baghdadi, S. The Using of Nanomaterials as Catalysts for Photodegradations. *Journal of Physics: Conference Series* **2021**, *1853*, 012052.

[33] Arya, S.; Mahajan, P.; Mahajan, S.; Khosla, A.; Datt, R.; Gupta, V.; Young, S.-J.; Oruganti, S. K. Review—Influence of Processing Parameters to Control Morphology and Optical Properties of Sol-Gel Synthesized ZnO Nanoparticles. *ECS Journal of Solid State Science and Technology* **2021**, *10* (2), 023002.

[34] Bokov, D.; Turki Jalil, A.; Chupradit, S.; Suksatan, W.; Javed Ansari, M.; Shewael, I. H.; Valiev, G. H.; Kianfar, E. Nanomaterial by Sol-Gel Method: Synthesis and Application. *Advances in Materials Science and Engineering* **2021**, *2021* (1), 5102014.

[35] Kumar, A.; Yadav, N.; Bhatt, M.; Mishra, N.; Chaudhary, P.; Singh, R. Sol-Gel Derived Nanomaterials and It's Applications: A Review. *Research Journal of Chemical Sciences* **2015**, *5*, 1–6.

[36] Mahato, S. S.; Mahata, D.; Panda, S.; Mahata, S. Perspective Chapter: Sol-Gel Science and Technology in Context of Nanomaterials – Recent Advances. In *Sol-Gel Method*; Singh, J. P., Acharya, S. S., Kumar, S., Dixit, S. K., Eds.; IntechOpen: Rijeka, **2023**.

[37] Navas, D.; Fuentes, S.; Castro-Alvarez, A.; Chavez-Angel, E. Review on Sol-Gel Synthesis of Perovskite and Oxide Nanomaterials. *Gels* **2021**, *7* (4).

[38] Thanh, N. T. K.; Maclean, N.; Mahiddine, S. Mechanisms of Nucleation and Growth of Nanoparticles in Solution. *Chem. Rev.* **2014**, *114* (15), 7610–7630.

[39] Polte, J. Fundamental Growth Principles of Colloidal Metal Nanoparticles – a New Perspective. *CrystEngComm* **2015**, *17*, 6809–6830.

[40] Abbas, M.; Zeng, L.; Guo, F.; Rauf, M.; Yuan, X.-C.; Cai, B. A Critical Review on Crystal Growth Techniques for Scalable Deposition of Photovoltaic Perovskite Thin Films. *Materials* **2020**, *13*, 1–42.

[41] Zhou, J.; Zhou, Y.; Tang, W. Molecular Mechanism of Organic Crystal Nucleation: A Perspective of Solution Chemistry and Polymorphism. *Crystals* **2022**, *12* (7).

[42] Jana, S. Advances in Nanoscale Alloys and Intermetallics: Low Temperature Solution Chemistry Synthesis and Application in Catalysis. *Dalton transactions (Cambridge, England : 2003)* **2015**, *44*.

[43] Nishchakova, A. D.; Bulusheva, L. G.; Bulushev, D. A. Supported Ni Single-Atom Catalysts: Synthesis, Structure, and Applications in Thermocatalytic Reactions. *Catalysts* **2023**, *13* (5).

[44] Juhász junger, I.; Werner, D.; Schwenzfeier-Hellkamp, E.; Ehrmann, A. Influence of Illumination Spectra on DSSC Performance. *Optik* **2019**, *177*, 8–12.

[45] Rondán-Gómez, V.; Montoya De Los Santos, I.; Seuret-Jiménez, D.; Ayala-Mató, F.; Zamudio-Lara, A.; Robles-Bonilla, T.; Courel, M. Recent Advances in Dye-Sensitized Solar Cells. *Appl. Phys. A* **2019**, *125* (12), 836.

[46] Longo, C.; De Paoli, M.-A. Dye-Sensitized Solar Cells: A Successful Combination of Materials. *J. Braz. Chem. Soc.* **2003**, *14*, 898–901.

[47] Wu, J.; Lan, Z.; Lin, J.; Huang, M.; Huang, Y.; Fan, L.; Luo, G. Electrolytes in Dye-Sensitized Solar Cells. *Chem. Rev.* **2015**, *115* (5), 2136–2173.

[48] Mahajan, P.; Datt, R.; Gupta, V.; Arya, S. Synthesis and Characterization of ZnO@WO_3 Core/Shell Nanoparticles as Counter Electrode for Dye-Sensitized Solar Cell. *Surfaces and Interfaces* **2022**, *30*, 101920.

[49] Dissanayake, M. A. K. L.; Kumari, J. M. K. W.; Senadeera, G. K. R.; Jaseetharan, T.; Weerasinghe, J.; Anwar, H. A Low-Cost, Vein Graphite/Tin Oxide Nanoparticles Based Composite Counter Electrode for Efficient Dye-Sensitized Solar Cells. *Materials Science and Engineering: B* **2021**, *273*, 115440.

[50] Mposa, E.; Sithole, R. K.; Ndala, Z.; Ngubeni, G. N.; Mubiayi, K. P.; Shumbula, P. M.; Machogo-Phao, L. F. E.; Moloto, N. Novel 2D-AuSe Nanostructures as Effective Platinum Replacement Counter Electrodes in Dye-Sensitized Solar Cells. *RSC Adv.* **2022**, *12* (20), 12882–12890.

[51] Ye, M.; Wen, X.; Wang, M.; Iocozzia, J.; Zhang, N.; Lin, C.; Lin, Z. Recent Advances in Dye-Sensitized Solar Cells: From Photoanodes, Sensitizers and Electrolytes to Counter Electrodes. *Materials Today* **2015**, *18* (3), 155–162.

[52] Yang, J.; Yu, X.; Li, Y.; Cheng, G.; Yi, Z.; Zhang, Z.; Chi, F.; Liu, L. A Novel Dye-Sensitized Solar Cell Structure Based on Metal Photoanode without FTO/ITO. *Micromachines (Basel)* **2022**, *13* (1), 122.

[53] Jamalullail, N.; Mohamad, I. S.; Norizan, M. N.; Mahmed, N.; Taib, B. N. Recent Improvements on TiO_2 and ZnO Nanostructure Photoanode for Dye Sensitized Solar Cells: A Brief Review. *EPJ Web of Conferences* **2017**, *162*, 01045.

[54] Miao, F.; Sun, B.; Tao, B.; Wang, Y.; Chu, P. K. MoS_2/Ag/TiO_2 for Photoanode of Dye Sensitized Solar Cells. *Journal of Materials Research and Technology* **2022**, *20*, 781–790.

[55] Dubey, R. S.; Jadkar, S. R.; Bhorde, A. B. Synthesis and Characterization of Various Doped TiO_2 Nanocrystals for Dye-Sensitized Solar Cells. *ACS Omega* **2021**, *6* (5), 3470–3482.

[56] Sharma, K.; Sharma, V.; Sharma, S. S. Dye-Sensitized Solar Cells: Fundamentals and Current Status. *Nanoscale Res Lett* **2018**, *13* (1), 381.

[57] Wu, J.; Lan, Z.; Lin, J.; Huang, M.; Huang, Y.; Fan, L.; Luo, G.; Lin, Y.; Xie, Y.; Wei, Y. Counter Electrodes in Dye-Sensitized Solar Cells. *Chem. Soc. Rev.* **2017**, *46* (19), 5975–6023.

[58] Bhojanaa, K. B.; Kannadhasan, S.; Santhosh, N.; Vijayakumar, P.; Senthil Pandian, M.; Ramasamy, P.; Pandikumar, A. Enhanced Electrochemical and Photovoltaic Performance for MoO3 Nanorods at Different Calcination Temperature Based Counter Electrode in Pt-Free Dye-Sensitized Solar Cells Applications. *SN Applied Sciences* **2020**, *2* (10), 1750.

[59] Meyer, E.; Taziwa, R.; Mutukwa, D.; Zingwe, N. A Review on the Advancement of Ternary Alloy Counter Electrodes for Use in Dye-Sensitised Solar Cells. *Metals* **2018**, *8* (12).

[60] Guy, O. J.; Walker, K.-A. Graphene Functionalization for Biosensor Applications; **2016**; pp 85–141.

[61] Sarker, S.; Ahammad, A. J. S.; Seo, H. W.; Kim, D. M. Electrochemical Impedance Spectra of Dye-Sensitized Solar Cells: Fundamentals and Spreadsheet Calculation. *International Journal of Photoenergy* **2014**, *2014* (1), 851705.

[62] Sacco, A. Electrochemical Impedance Spectroscopy: Fundamentals and Application in Dye-Sensitized Solar Cells. *Renewable and Sustainable Energy Reviews* **2017**, *79*, 814–829.

[63] Becker, M.; Bertrams, M.-S.; Constable, E. C.; Housecroft, C. E. How Reproducible Are Electrochemical Impedance Spectroscopic Data for Dye-Sensitized Solar Cells? *Materials (Basel)* **2020**, *13* (7).

[64] Thomas, S.; Thrithamarassery Gangadharan, D.; Anjusree, G.; T.A., D.; Nair, S.; Nair, S. A Review on Counter Electrode Materials in Dye-Sensitized Solar Cells. *Journal of Materials Chemistry A* **2014**, *2*, 4474–4490.

[65] Wei, L.; Wu, Q.; Chen, W.; Wang, D.; Jiang, B.; Sun, G.; Yu, F.; Feng, J.; Yang, Y. Balance of Catalytic Activity and Conductivity of Cu2ZnSnS4/Graphene Counter Electrode for Dye-Sensitized Solar Cells: Using Hydrothermal-Synthesized Kesterite Cu_2ZnSnS_4 and Graphene Obtained by Product Line. *Journal of Solid State Electrochemistry* **2020**, *24* (2), 263–272.

[66] Shao, W.; Wu, W. High-Efficiency (Over 10%) Parallel Tandem Dye-Sensitized Solar Cells Based on Tri-Carbon Electrodes. *Transactions of Tianjin University* **2022**, *28* (5), 414–422.

[67] Liu, W.-W.; Jiang, W.; Liu, Y.-C.; Niu, W.-J.; Liu, M.-C.; Kong, L.-B.; Lee, L.; Wang, Z. M.; Chueh, Y.-L. Interface Engineered Binary Platinum Free Alloy-Based Counter Electrodes with Improved Performance in Dye-Sensitized Solar Cells. *Scientific Reports* **2020**, *10* (1), 9157.

[68] Jena, A.; Mohanty, S. P.; Kumar, P.; Naduvath, J.; Gondane, V.; Lekha, P.; Das, J.; Narula, H. K.; Mallick, S.; Bhargava, P. Dye Sensitized Solar Cells: A Review. *Transactions of the Indian Ceramic Society* **2012**, *71* (1), 1–16.

[69] Yeoh, M.-E.; Chan, K.-Y. Recent Advances in Photo-Anode for Dye-Sensitized Solar Cells: A Review: Recent Advances in Photo-Anode for DSSCs: A Review. *Int J Energy Res* **2017**, *41* (15), 2446–2467.

[70] Garcia Mayo, S. *Dye-Sensitized Solar Cells: The Future of Consumer Electronics?*; **2021**.

[71] Beraich, M.; Shaili, H.; Hafidi, Z.; Benhsina, E.; Majdoubi, H.; Taibi, M.; Guenbour, A.; Bellaouchou, A.; Mzerd, A.; Bentiss, F.; Zarrouk, A.; Fahoume, M. Facile Synthesis of the Wurtz Stannite (Orthorhombic) Cu_2MnGeS_4 Thin Film via Spray Ultrasonic Method: Structural, Raman, Optical and Electronic Study. *Journal of Alloys and Compounds* **2020**, *845*, 156216.

[72] Berman, S.; Sai Gautam, G.; Carter, E. A. Role of Na and Ca as Isovalent Dopants in Cu_2ZnSnS_4 Solar Cells. *ACS Sustainable Chem. Eng.* **2019**, *7* (6), 5792–5800.

[73] Chari, C. *Exploring Thin Films and Coatings with AFM*. AZoM, **2023**. https://www.azom.com/article.aspx?ArticleID=22108 (accessed 2024-12-21).

[74] Sivarajah, I. Atomic Force Microscopy: General Principles and Applications. *AZoOptics*. **2021**. https://www.azooptics.com/Article.aspx?ArticleID=2083 (accessed 2024-12-21).

[75] Mokobi, F. Atomic Force Microscope: Principle, Parts, Uses - Microbe Notes. *microbenotes*. **2023**. https://microbenotes.com/atomic-force-microscope-afm/ (accessed 2024-12-21).

Chapter 3: Colloidal synthesis and characterization of Cu_2ZnSnS_4, Li_2ZnSnS_4 and Na_2ZnSnS_4 nanoparticles

3.1. Introduction

Growing concerns about the energy and the environment have prompted ongoing development into low-cost and high-efficiency solar absorber materials. The traditional light absorbing materials for photovoltaics application, for example $Cu(InGa)Se_2$ (CIGS) are the most widely used and commercialized materials for large scale photovoltaic manufacturing because of their high-power conversion efficiency and stability [1,2]. Nevertheless, alternative potential materials are also being thoroughly studied because indium (In) and gallium (Ga) elements are scarce and expensive in CIGS materials. Thus, among various types of semiconductors, CZTS has been proposed to be an appropriate absorber for solar cell applications. Since all the components of Cu_2ZnSnS_4 (CZTS) are more abundant in the earth's crust compared to those of CIGS, they are also far less expensive and safer for the environment. Zinc (Zn) and tin (Sn) are found in the earth's crust at 1500 and 45 times, respectively, which are higher in abundance than In and Ga [3]. CZTS has similar crystal structure and electrical characteristics to CIGS. These properties include having p-type conductivity and a strong light absorption ability (high absorption coefficient of over 10^4 cm^{-1}) in the wavelength range from visible to near infrared of the solar spectrum [3–6].

Nevertheless, CZTS-based solar cells have so far demonstrated comparatively low efficiencies (<13%), which have been linked to the existence of Cu-Zn antisite defects that cause disorder in the CZTS kesterite crystal structure, leading to band gap narrowing and poor light absorption [7,8]. Given that copper tends to exist in both monovalent and divalent forms, the existence of defects may be the result of CZTS dissociating [8]. Therefore, it is worth looking into replacing the copper atoms with alkali metal atoms which always exist in monovalent form. These monovalent metals have the potential to reduce the defects observed with the kesterite crystal structure of CZTS.

The purpose of this work was to entirely replace copper with monovalent alkali metals i.e., lithium and sodium atoms respectively, to form analogues of CZTS known as Li_2ZnSnS_4 (LZTS) and Na_2ZnSnS_4 (NZTS) respectively through a low-cost colloidal synthesis method. The synthesized materials have been characterized through various techniques such as X-ray diffraction (XRD), Raman spectroscopy, Fourier transform infrared spectroscopy (FTIR), X-ray photoelectron spectroscopy (XPS), nuclear magnetic resonance (NMR) spectroscopy, ultraviolet-visible (UV-Vis) spectroscopy and transmission electron microscopy (TEM).

3.2. Experimental section

3.2.1. Chemicals

Copper (I) chloride (CuCl, 97.0%), lithium sulfide (Li_2S, 99.98%), sodium sulfide nanohydrate ($Na_2S•5H_2O$, ≥ 98.0%), zinc chloride ($ZnCl_2$, 98.0%), elemental sulfur (S, ≥ 99.0%), stannic chloride ($SnCl_4•5H_2O$, 97.5%), oleylamine (OLA, 70.0%), ethanol (96.0%), chloroform ($CHCl_3$), deuterated chloroform ($CDCl_3$, 99.8%), toluene, hexane, methanol, isopropanol, de-ionised water. All chemicals were purchased from Sigma Aldrich, except for stannic chloride, which was purchased from Saarchem. All chemicals were used without any further purification.

3.2.2. Colloidal synthesis of the CZTS, LZTS and NZTS nanoparticles

OLA capped CZTS nanoparticles were synthesized using the sequential addition colloidal method as shown in Figure 3.1. The synthesis method was derived from Ngubeni *et al.* with some modifications [14]. 20 mL of OLA was added to a three-necked round bottom flask. The flask was placed on a heating mantle, connected to a Schleck line and a condenser. OLA was then heated to 100 °C while being purged with N_2 to remove oxygen from the reaction. A mole ratio of 2:1:1:4 was used for the synthesis of CZTS and the order in which the precursor salts were sequentially added is as follows: CuCl was first to be added at 100 °C, followed by $ZnCl_2$ at 120 °C, then $SnCl_4•5H_2O$ at 180 °C, and finally S at 220 °C. Once all the precursor salts were added sequentially, the temperature of the reaction flask was held at 220 °C for 50 minutes.

The reaction mixture was subsequently cooled to 70 °C, and the nanoparticles were precipitated by adding ethanol to the reaction mixture. Finally, the nanoparticles were isolated by centrifugation (at 8000 rpm) for five cycles while washing with a mixture of ethanol and chloroform with a ratio of 4:1. The nanoparticles were then oven dried at 100 °C for 24 hours.

A similar method was followed for the synthesis of OLA capped LZTS and NZTS nanoparticles however Li_2S was used as the precursor salt for LZTS with a mole ratio of 2:1:0.25:2 and $Na_2S•9H_2O$ was used as the precursor salt for NZTS with a mole ratio of 2:1:0.5:4.

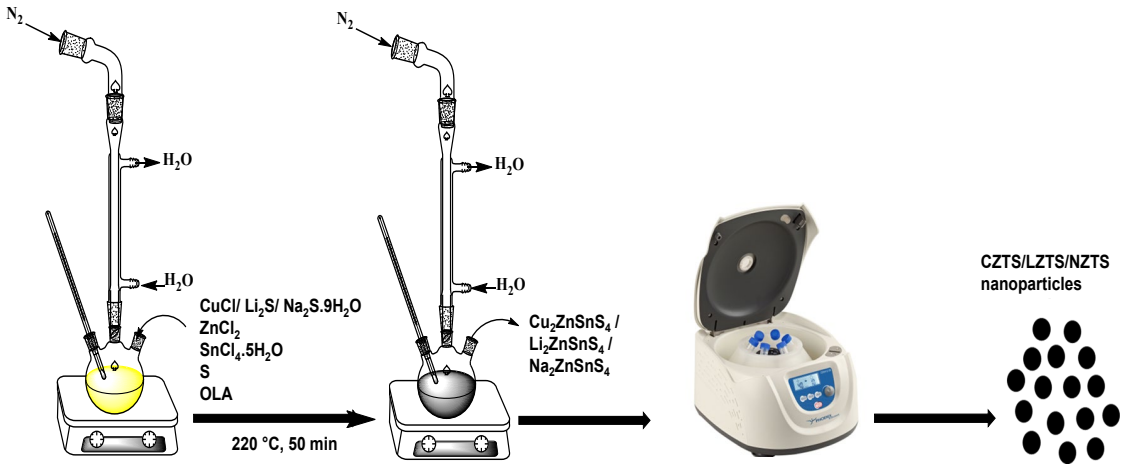

Figure 3.1: Schematic diagram showing the synthesis of the nanoparticles.

3.3. Characterization

The following techniques were used to characterize the nanoparticles:

UV-vis absorption measurements were carried out using the Horiba scientific Duetta™ 3-in-1 spectrofluorometer with a CCD or a silicon-based multi-channel array detector. The powdered samples were dispersed in toluene and loaded into a quartz cuvette with a 1 cm path length for spectral analysis. For crystal structure analysis, X-ray diffraction (XRD) measurements were conducted using the Bruker D2 Phaser Powder X-ray diffractometer, employing Cu-Kα1 radiation (λ = 1.54184 Å) at 30 kV/30 mA with SSD160 (1D mode) detector. The measurements were performed in a step count of 2279 for 20 minutes over a 2θ range of 10 – 70° at room temperature and a PSD opening of 4.774°. Morphological characterization was performed using a

transmission electron microscope (TEM), specifically the FEI Tecnai T12 and JEOL JEM-2100, operating at 200 kV. The samples were dispersed in toluene and sonicated for 15 minutes. Subsequently, a few drops of the suspended nanoparticles were deposited onto a copper grid with a lacy carbon support and allowed to air dry at room temperature before analysis. A Java-based image processing software called ImageJ was used to estimate the sizes of the nanoparticles and the estimated average sizes of CZTS, LZTS and NZTS nanoparticles. The FTIR spectra were obtained using the Thermo Scientific™ Nicolet™ iS20 FTIR Spectrometer fitted with a diamond crystal and a deuterated triglycine sulfate (DTGS) detector. ^{1}H NMR data was collected using 400 MHz Bruker AVANCE III spectrometer. Solid-state ^{7}Li and ^{23}Na MAS NMR experiments were performed on a 11.8 T Bruker AVANCE III 500 MHz spectrometer. X-ray photoelectron spectroscopy (XPS) analysis was performed using the Thermo ESCAlab 250Xi with a monochromatic Al Kα X-ray source (1486.7 eV, 300 W, 900 µm). The scan survey spectra were measured at a constant pass energy mode of 100 eV while the Hi-Res spectra were measured at a pass energy mode of 20 eV.

For Raman analysis, an infrared diode laser source of 633 nm (He-Ne) was utilized to excite low-frequency spectra (below 500 cm^{-1}). A low incident light power density of less than 15 W/cm^2 was utilized to prevent photodegradation of the samples and to rule out laser damage. Spectra were captured with a 20X long working distance objective (NA = 0.35), then scattered with a high-solution LabRam HR800 grating spectrometer equipped with a charge-coupled detector.

3.4. Results and discussions

3.4.1. X-Ray Diffraction analysis

To confirm that the CZTS nanoparticles were successfully produced via colloidal synthesis, XRD analysis was carried out after synthesis. Figure 3.2 (a) displays both the as-synthesised CZTS nanoparticles' XRD pattern along with the standard reference pattern. The CZTS nanoparticles exhibited a tetragonal kesterite crystal structure and matched well with the I-42 space group from pattern: PDF 01-080-6857. The diffraction peaks CZTS were observed at 2θ values of 29.1°, 33.5°, 47.9°, 56.7°, and 59.5°, respectively. These values corresponded to the diffraction planes of (112),

(200), (220), (312), and (224). Furthermore, there were no impurities observed from the CZTS XRD diffractogram. XRD data can also offer valuable insights into estimating the crystal size of materials. To achieve this, the Debye–Scherrer equation (3.1) was used to calculate the crystal size of the materials [11]:

$$D = \frac{k\lambda}{\beta \cos\theta} \tag{3.1}$$

In equation 3.1, λ is the X-ray wavelength, β is the peak broadening, or the full width at half maximum (FWHM) of the peak in radians, θ is the Bragg angle in radians, D is the average crystal size in Angstroms (Å), and k is a dimensionless shape factor with a value of around 0.9. The calculated estimate of the average crystallite size for all the XRD peaks of CZTS were 9 ± 3.1 nm.

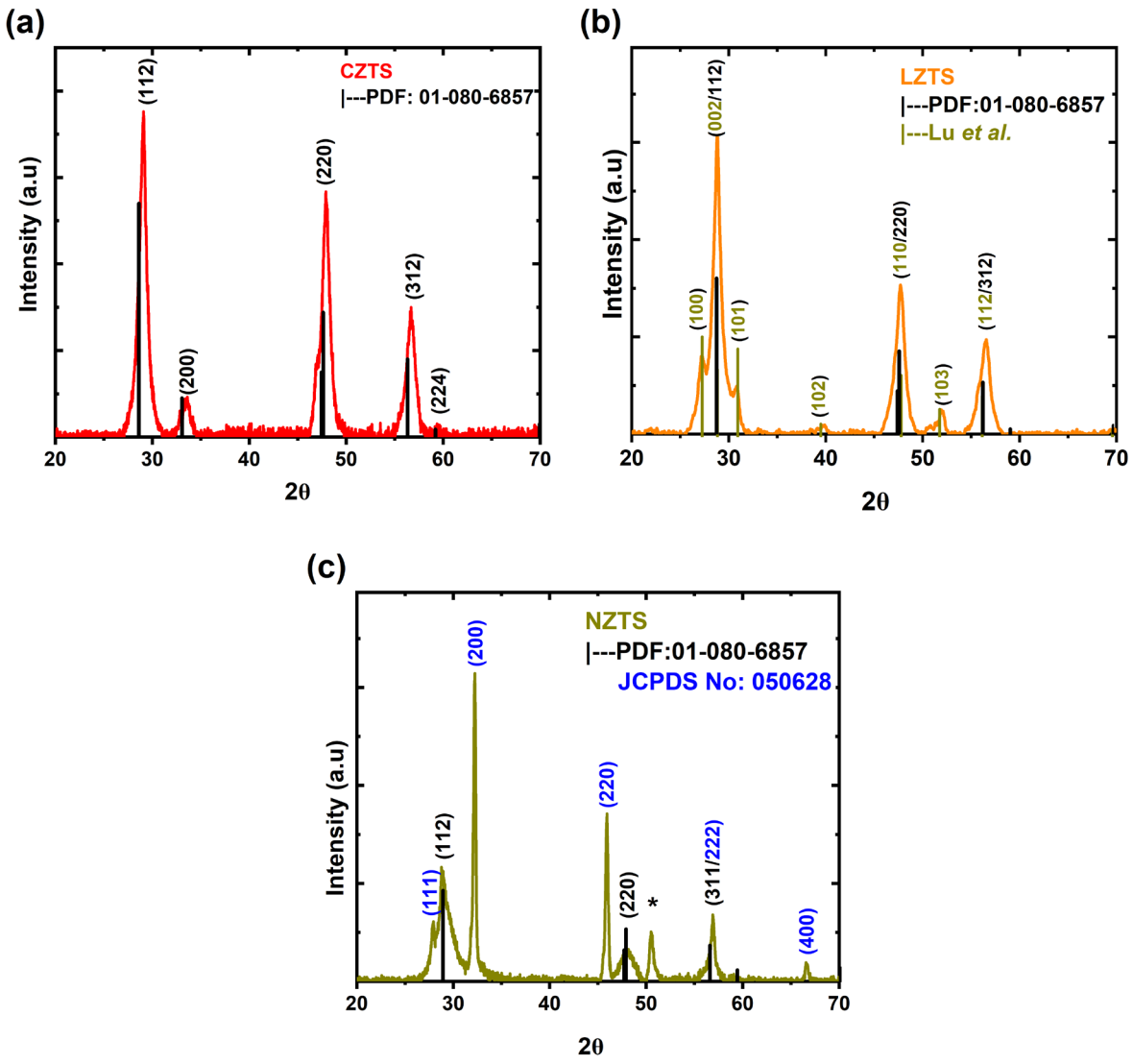

Figure 3.2: XRD patterns of the as-synthesized (a) CZTS, (b) LZTS and (c) NZTS nanoparticles.

In Figure 3.2 (b), LZTS adopted a hexagonal wurtzite form of the CZTS crystal structure with a space group of $P6_3mc$, which was comparable to what Lu *et al*. had reported [2]. The diffraction peaks of the nanoparticles appeared at 2θ values of 27.3°, 28.8°, 30.8°, 39.8°, 47.7°, 51.9°, and 56.5°, respectively. These values corresponded with the diffraction planes of (100), (002), (101), (102), (110), (103), and (112). However, the (002), (110) and (112) diffraction planes of LZTS appear to be in the same position as the (112), (220) and (312) diffraction planes of CZTS. This suggests that the LZTS nanoparticles crystallized into two crystal structures which are the wurtzite and kesterite crystal structures. Similarly to estimating the crystallite size of CZTS, the estimated calculated average crystallite size for the kesterite phase of LZTS was 7 ± 0.66 nm and the estimated calculated average crystallite size for the wurtzite phase of LZTS was 7 ± 1.1 nm. Kuang *et al*. and Dimitrievska *et al*. both recognize the kesterite phase of CZTS as the most stable compared to the wurtzite phase [23,24]. Therefore, the stability of the wurtzite phase of LZTS might hinder the catalytic activity of the nanoparticles duration their application as a counter electrode in dye sensitized solar cells (DSSCs).

Similarly to LZTS, the NZTS nanoparticles (Figure 3.2c) have crystallized into two crystal structures. The first crystal structure is the kesterite crystal structure which is similar to that of CZTS with diffraction peaks appearing at 2θ values of 28.9°, 48.1° and 56.9° which corresponded to (112), (220) and (312) diffraction planes. The other crystal phase is observed to be a halite or a face-centred cubic (FCC) crystal structure which comes from an unknown secondary product. Moreover, the halite or FCC crystal structure is similar to that of NaCl. The NaCl halite crystal structure has diffraction peaks appearing at around 27.8°, 32.2°, 45.9°, 56.9°, and 66.6° which correspond to (111), (200), (220), (222) and (400) diffraction planes (JCPDS No: 050628). The estimated calculated average crystallite size for the kesterite phase of NZTS was 8 ± 4.1 nm and the estimated calculated average crystallite size for the FCC phase of NZTS was 26 ± 6.97 nm. Moreover, looking at the peak intensities, the cubic crystal structure is more dominant than the kesterite crystal structure of NZTS. Similarly to LZTS, the coexistence of the two different crystal structures within the NZTS sample

might complicate the material's behaviour during the application studies as a counter electrode in DSSCs.

3.4.2. FTIR analysis

FTIR was used to characterize the surface chemistry and investigate the binding of the OLA capping agent on CZTS, LZTS and NZTS nanoparticles. The FTIR spectra of the as-synthesized nanoparticles are depicted in Figure 3.3. Three functional groups were identified in pure OLA which were C=C, NH_2 and CH_2/CH_3. The OLA spectrum showed high intensity of symmetric and asymmetric C-H stretching vibration at 3004 cm^{-1}, 2923 cm^{-1} and 2852 cm^{-1}, which resulted from CH_2 groups. The peak at ~1462 cm^{-1} is attributed to the C-H bending vibrations of the methyl (CH_3) group present in the alkane chain of OLA. The peaks at 3373 cm^{-1} ,1616 cm^{-1}, 793 cm^{-1} correspond to NH_2 stretch vibrations and NH_2 bending vibrations, respectively. The peak at 1071 cm^{-1} corresponds to the C-N stretching vibrations of the primary amine. All the nanoparticles showed peaks that were distinctive to the oleyl group in the 2800 – 3500 cm^{-1}, 1315 –1680 cm^{-1} and 1090 – 500 cm^{-1} regions which indicated the presence of the capping agent in all of the nanoparticles. Additionally, there is a minor shift to a higher wavenumber of the C-N stretching vibration from the spectrum of pure OLA compared to that of OLA capped CZTS, LZTS and NZTS spectra. This shift may be explained by the interaction between N and the nanoparticles through coordination and the subsequent constraint of the capping ligand motions thus suggesting that the nanoparticles are attached to the amine group of the ligand [25,26]. The detected O=C=O is a result of atmospheric CO_2.

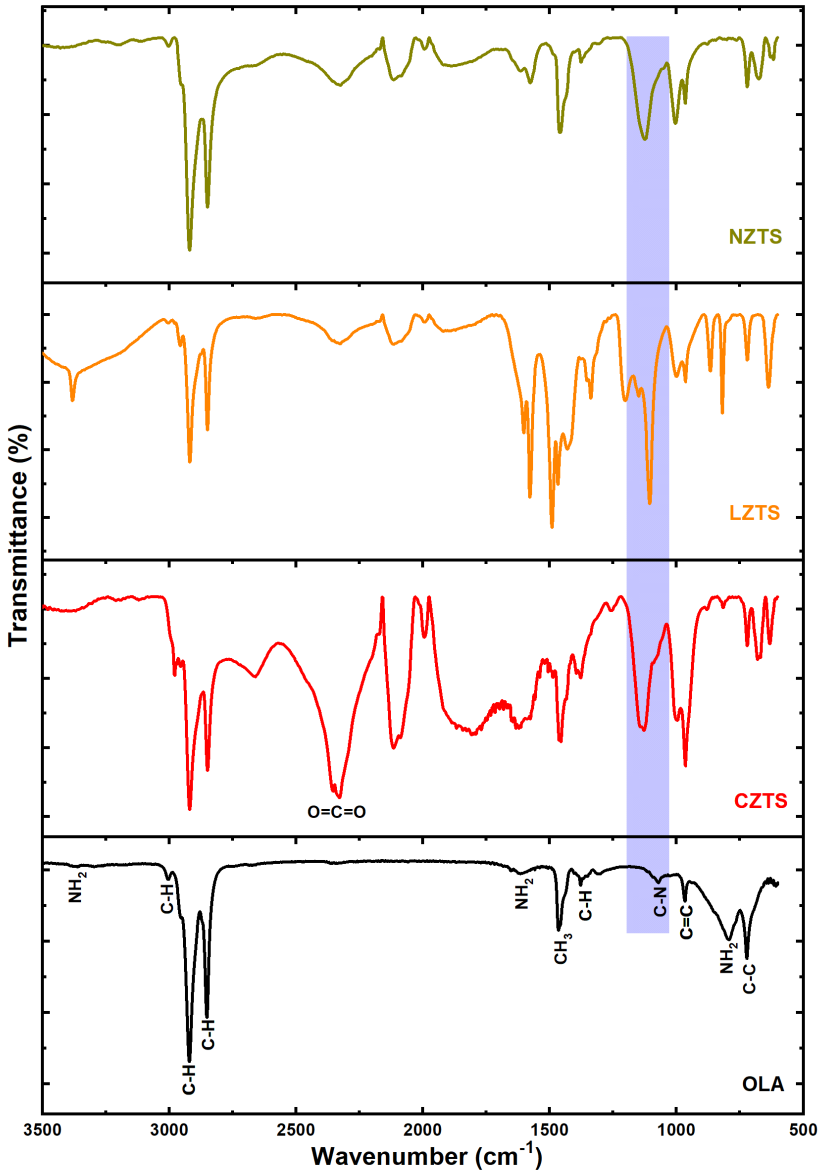

Figure 3.3: FTIR spectra of OLA, CZTS, LZTS and NZTS.

3.4.3. NMR analysis

The capping of the produced nanoparticles was further confirmed by proton NMR. The findings summarized in Table 3.1 are from the ^{1}H NMR spectra of OLA, OLA capped CZTS, LZTS and NZTS respectively, (Figure 3.4). The changes in the multiplicity and the number of protons of the peaks observed in the ^{1}H NMR of the OLA capped CZTS, LZTS and NZTS nanoparticles could imply a potential interaction between the capping agent and the synthesized nanoparticles. Moreover, the peak corresponding to the

proton associated with the amine in OLA (1.44 – 1.40 ppm) has decreased in intensity across all the OLA-capped nanoparticles, indicating the proximity of the nanoparticles to this functional group. This observation suggests the likely attachment of the nanoparticles to the amine functional group of the capping agent. Thus, the amine functional group of OLA is responsible for the binding of OLA to the synthesized nanoparticles.

Table 3.1: NMR spectral assignments for OLA, CZTS, LZTS and NZTS nanoparticles.

Compound	^{1}H NMR (δ ppm)
OLA	-HC=CH- (5.38 – 5.28), -H_2C-NH_2 (2.89 – 2.64), H_2C-CH_2-HC= (2.03 – 1.92), -H_2C-H_2C-H_2C-NH_2 (1.44 – 1.40), -CH_2- (1.37 – 1.11), -CH_3 (0.89 – 0.85)
CZTS	-HC=CH- (5.40 – 5.37), -H_2C-NH_2 (3.67/2.72 – 2.38), H_2C-CH_2-HC= (2.03 – 1.98), -CH_2- (1.28), -CH_3/-CH_2- (0.92 – 0.88)
LZTS	-HC=CH- (5.37), -H_2C-NH_2 (3.67), H_2C-CH_2-HC= (2.04 – 1.99), -CH_2-(1.28), -CH_3/-CH_2- (0.90 – 0.88)
NZTS	-HC=CH- (5.50), H_2C-CH_2-HC= (2.15), -CH_2- (1.42 – 1.40), -CH_3/-CH_2- (1.02)

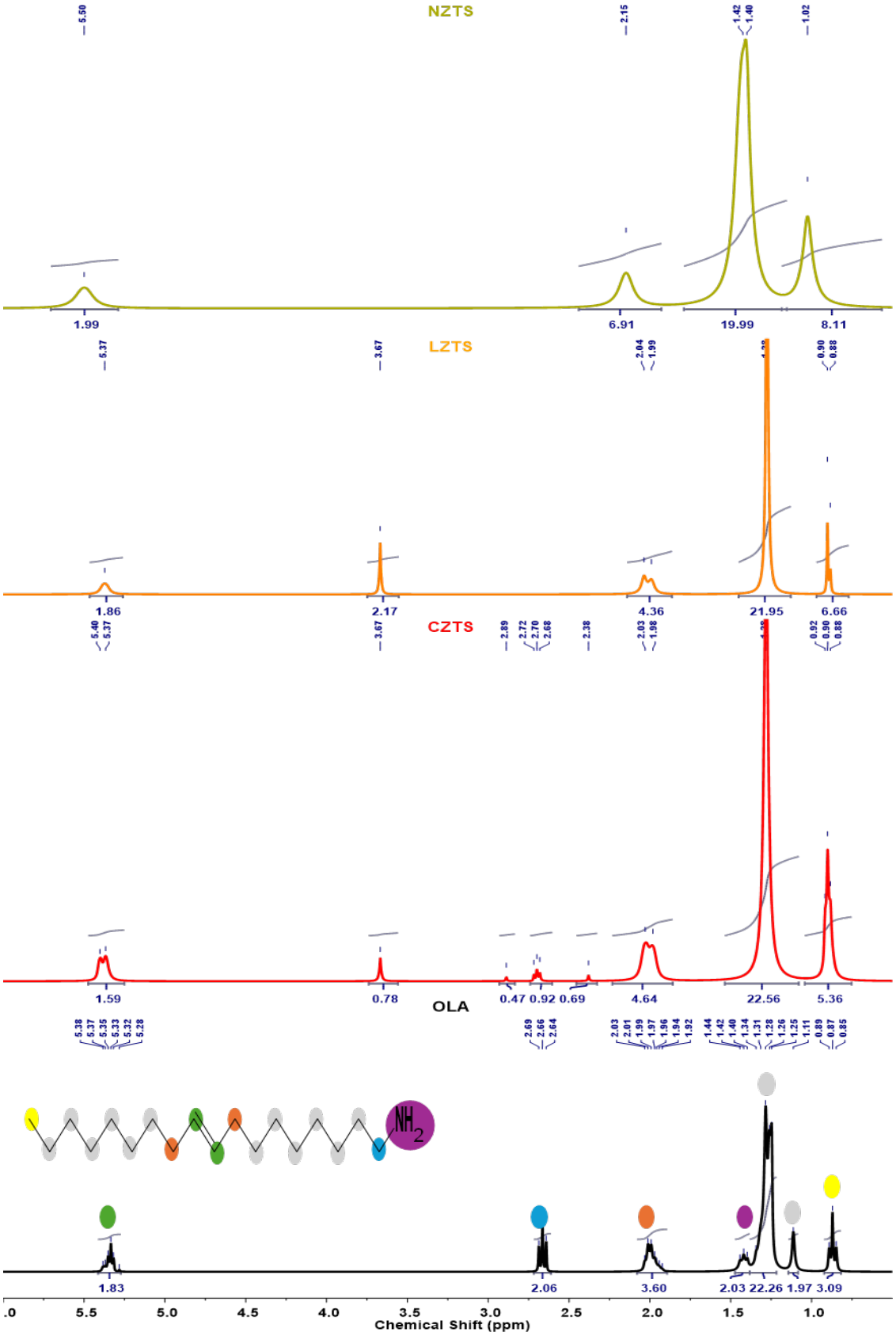

Figure 3.4: ^{1}H NMR spectra of OLA, CZTS, LZTS and NZTS nanoparticles.

On the other hand, solid state NMR (SSNMR) spectroscopy technique was used to confirm the presence of lithium and sodium atoms of LZTS and NZTS nanoparticles. The results are presented in Figure 3.5 below. Two peaks of lithium were observed for LZTS at 3.84 ppm and 1.42 ppm (Figure 3.5a) and one peak of sodium was observed for NZTS at 8.71 ppm (Figure 3.5b).

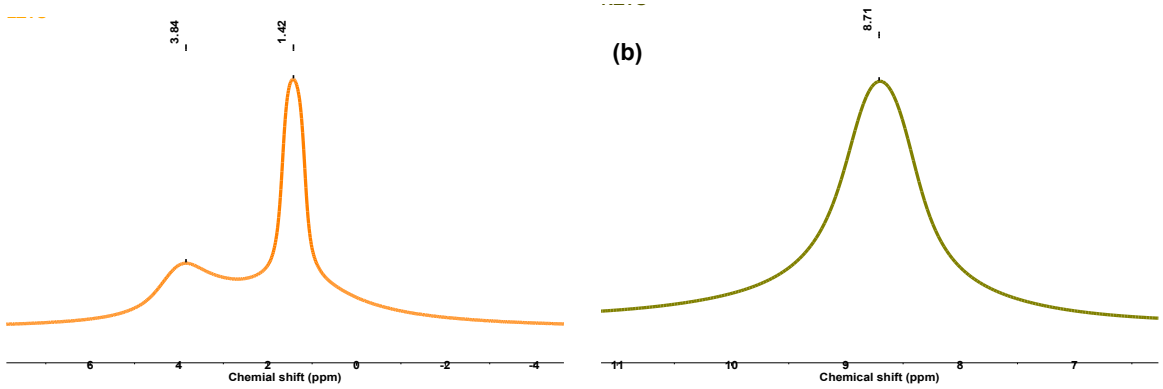

Figure 3.5: SSNMR spectra of (a) LZTS and (b) NZTS nanoparticles.

3.4.4. TEM analysis

The sizes and morphologies of CZTS, LZTS and NZTS nanoparticles were investigated through TEM analysis. Figure 3.6 (a – c) displays the TEM images of the as-synthesized nanoparticles. Both LZTS and NZTS nanoparticles formed small spherical particles while CZTS nanoparticles were quasi-spherical in shape. In addition to forming small circular particles, NZTS also formed nanocubes of various diagonal lengths. A histogram and TEM images of these nanocubes are depicted in Figure S3.1 (a – c) of the appendix section. The presence of the nanocubes along with nanoparticles in the NZTS sample further supports the statement made during XRD analysis about the presence of two different crystal phases in the NZTS sample.

The estimated average sizes of CZTS, LZTS and NZTS nanoparticles were 20 ± 5 nm, 8 ± 1 nm, 5 ± 1 nm respectively as depicted by the particle size distribution graphs (Figure 3.6 d – f). The nanocubes of NZTS had diagonal lengths ranging from 73 nm – 487 nm (histogram given Figure S3.1d).

All the nanoparticles were agglomerated and polydispersed. It has been previously reported that, polydispersity and agglomeration is associated with good photocatalytic

properties of nanomaterials [12,13]. Additionally, particle agglomeration and polydispersity can be beneficial for solar cell applications, as they enhance particle interconnectivity, thereby facilitating easier charge transport [14].

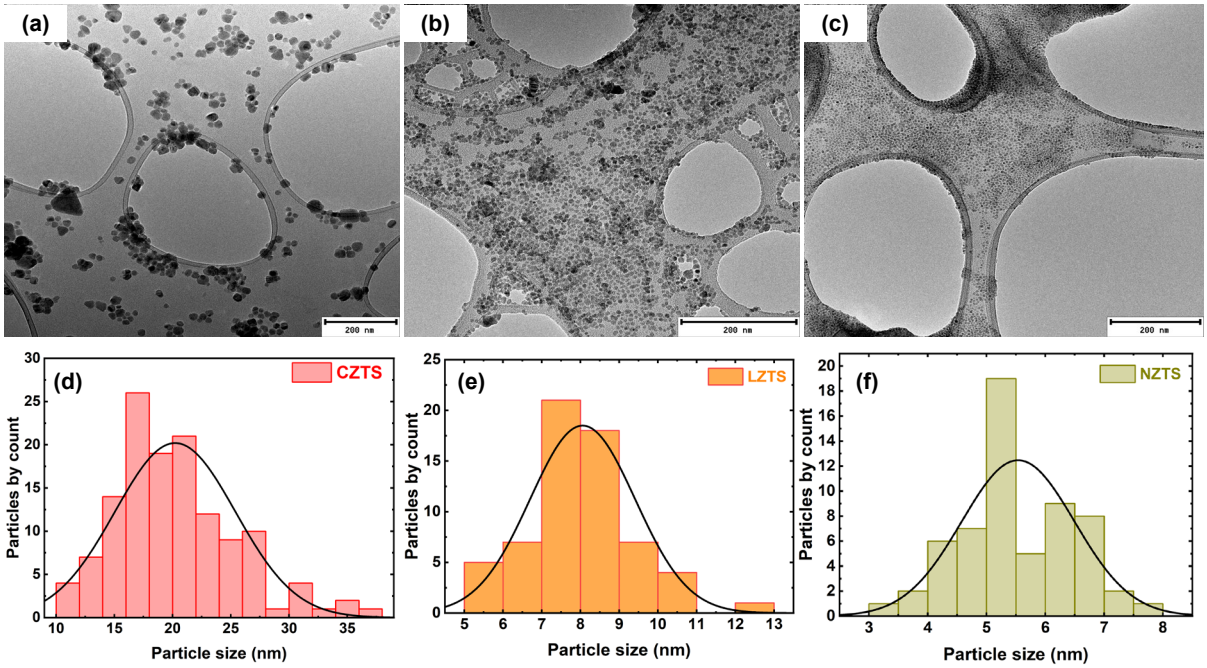

Figure 3.6: TEM images of (a) CZTS, (b) LZTS and (c) NZTS nanoparticles including particle size distribution histograms (d – f).

To better understand the crystallinity of the as-synthesized CZTS, LZTS and NZTS nanoparticles, high-resolution TEM (HRTEM) was carried out as shown in Figure 3.7. According to XRD, the (112) plane of the kesterite crystal structure is responsible for the lattice fringes that were seen on HRTEM images of all of the nanoparticles which had a d-spacing value of 0.32 nm. Additionally, the lattice fringes with a d-spacing value of 0.34 nm from LZTS (Figure 3.7 b) may be attributed to (100) planes of the wurtzite crystal structure.

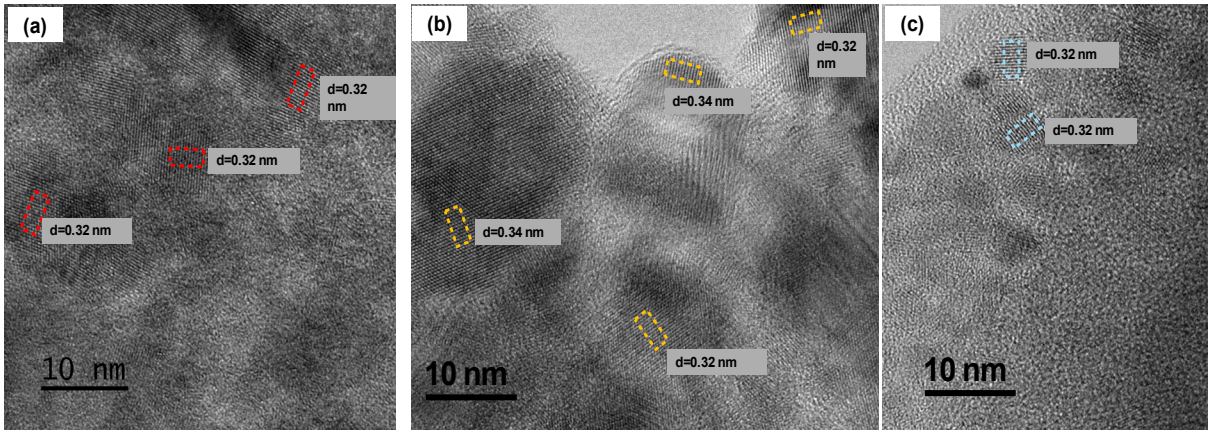

Figure 3.7: HRTEM images showing the d-spacing values of lattice fringes of (a) CZTS, (b) LZTS, and (c) NZTS nanoparticles.

Elemental composition analysis of the as-synthesized nanoparticles was conducted using TEM Energy Dispersive X-ray (TEM-EDX) technique, and the results are shown in Figure S3.2–S3.4 in the appendix section. EDX mapping shows the presence of Cu atoms that make up CZTS nanoparticles, Na atoms that make up NZTS nanoparticles, and atoms such as Zn, Sn and S, which make up all the as-synthesized nanoparticles. EDX mapping could not detect Li atoms from the LZTS sample because these atoms are too light and they also have a very low energy of characteristic radiation, making them difficult to detect by standard EDX methods. The Cl atoms present in the EDX mapping of NZTS (Figure S3.4), may be regarded as an impurity that comes from incomplete decomposition of the chloride precursors used during synthesis.

3.4.5. UV-Vis absorption analysis

To investigate the optical properties of the as-synthesised nanoparticles, UV-Vis absorption spectroscopy was used. The Tauc plot (Figure 3.8b) was then generated using the acquired UV-vis spectra (Figure 3.8a). The Tauc plots were used to calculate the optical band gap energy of the as-prepared CZTS, LZTS and NZTS nanoparticles respectively, based on the following equation [15].

$$(\alpha h\nu)^{\frac{1}{n}} = A(h\nu - E_g) \qquad (3.2)$$

where ν is the frequency, E_g is the band gap, α is the absorption coefficient, h is Planck's constant, and A is a constant. The permitted optical transition determines the

value of n. For materials with a direct band gap, it is assumed to be 1/2. The optical band gap of CZTS, LZTS and NZTS was 3.42 eV, 3.07 eV and 3.22 eV respectively. It is evident from these results that the substitution of Cu atoms by Li and Na atoms introduces a disorder in the nanomaterials which influences the electronic and optical properties of these materials since it marginally narrows the band gap of these nanomaterials. According to published research, the ideal optical band gap of CZTS usually falls within the range of 1.0 eV to 1.5 eV [12,14]. The increased band energy variation seen for the as-synthesized CZTS nanoparticles may be explained through surface modification of the nanoparticles by the capping agent [28]. When the capping agent binds to the surface of the nanoparticles, their surface properties are altered [28]. This leads to changes in the electronic structure and energy levels of the nanoparticles.

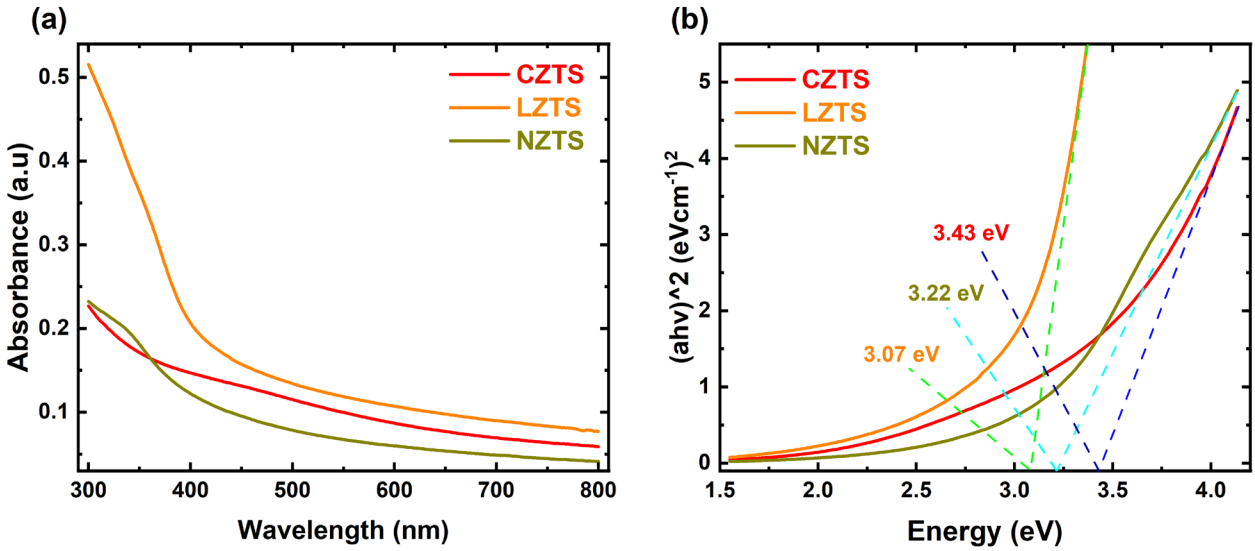

Figure 3.8: (a) UV-Vis absorption spectra and (b) Tauc plot of CZTS, LZTS and NZTS nanoparticles.

3.4.6. XPS analysis

3.4.6.1. CZTS

X-ray photoelectron spectroscopy (XPS) is a very useful technique in studying the atom bonding and elemental composition of the as-synthesized nanoparticles.

Copper, zinc, tin, sulphur, carbon, oxygen, and nitrogen atoms are present in the CZTS survey spectrum (Figure 3.9a). The capping agent OLA is responsible for the nitrogen and carbon atoms, whereas copper, zinc, tin and sulfur atoms make up the Cu-quaternary chalcogenide that is synthesized from the chloride salt precursors and elemental sulfur. The detected oxygen was assumed to be the consequence of the capping agent oxidizing because no oxide contaminants were seen during XRD analysis. [14]. The oxidation states of the constituent elements in the CZTS nanoparticles were identified using high-resolution XPS. At 932.1 eV (Cu $2p_{3/2}$) and 951.9 eV (Cu $2p_{1/2}$) in Figure 3.9b, the doublet peaks of copper had a peak separation energy of 19.8 eV, which is close to the standard 19.9 eV thus reflecting the oxidation state of Cu(I) [19, 20]. The oxidation state of zinc (II) is shown by the doublet peak in the zinc spectrum (Figure 3.9c) at 1022.1 eV (Zn $2p_{3/2}$) and 1045.1 eV (Zn $2p_{1/2}$), which exhibited a peak separation energy of 23.0 eV. However, the peak separation energy of 8.3 eV of the Sn 3d peaks, which were detected at 486.4 eV ($3d_{5/2}$) and 494.7 eV ($3d_{1/2}$), respectively, verified Sn (IV). The 2p peak of S lying in the range of 160 –164 eV suggests the S^{2-} species. These findings further validate the as-synthesised material's phase purity and are consistent with the published values of the binding state of the elemental constituents of CZTS [14,19–22].

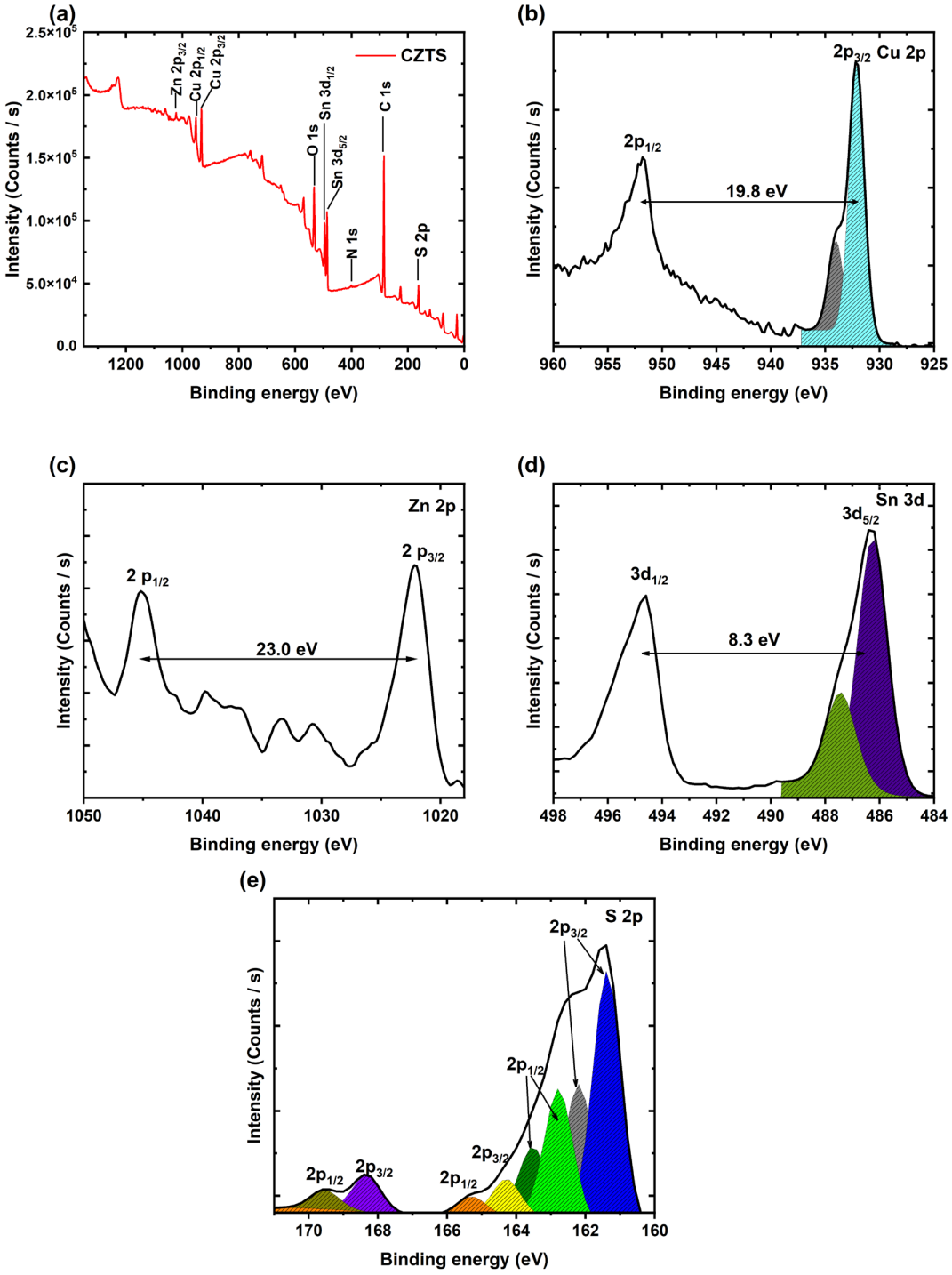

Figure 3.9: (a) XPS survey spectrum and high-resolution spectra of (b) copper, (c) zinc, (d) tin and (e) sulphur from CZTS nanoparticles.

Figure 3.10 shows not only the high-resolution spectra of the constituents of CZTS but also the high-resolution spectra of O 1s, N 1s and C 1s. O-C=O, C-C and C-O peaks from the capping agent OLA are the three distinctive carbon peaks that are shown in

the C1s (Figure 3.10a). The distinctive oxygen peaks, C = O, C-O and O-C=O are also visible in the O1s spectrum (Figure 3.10b). OLA's binding to the CZTS nanoparticles via the nitrogen atom is linked to two peaks in the nitrogen high resolution spectra (Figure 3.10c) that are located between 398.5 and 405.6 eV.

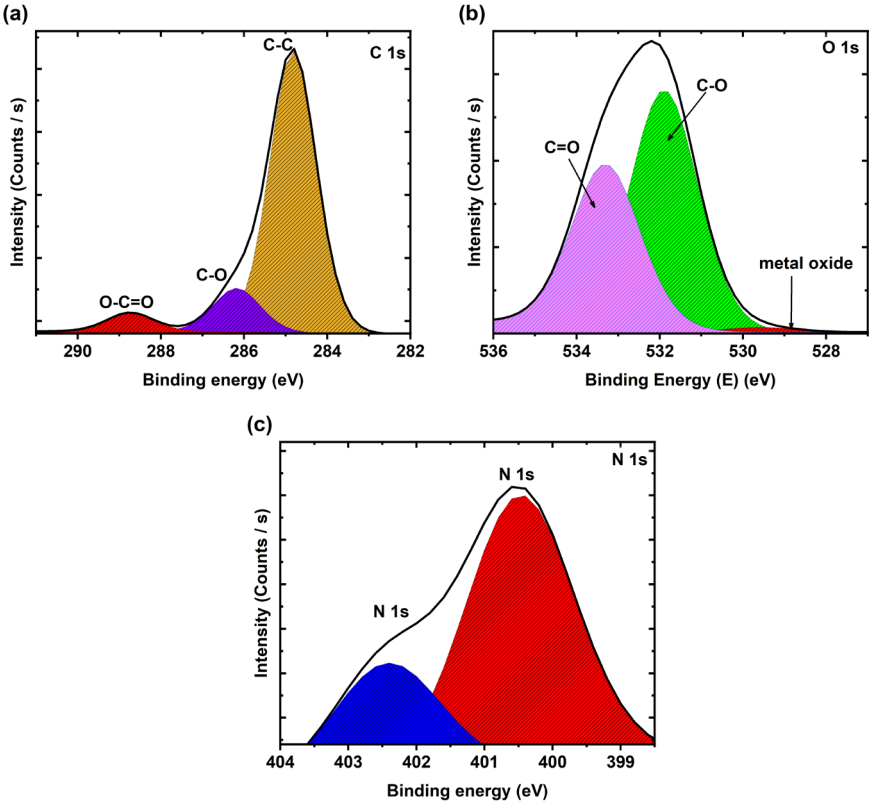

Figure 3.10: High-resolution spectra of (a) carbon, (b) oxygen and (c) nitrogen from CZTS nanoparticles.

3.4.6.2. LZTS

Atoms of zinc, tin, sulphur, carbon, oxygen, and nitrogen are present in the LZTS survey spectrum (Figure 3.11a). The capping agent OLA is responsible for the nitrogen and carbon atoms, whereas zinc and tin atoms make up the alkali quaternary chalcogenide which is synthesized from the chloride salt precursors and elemental sulfur. The Li peak could not be detected in the survey spectrum even though SSNMR confirmed the presence of Li atoms in the LZTS nanoparticles. Since XPS is a surface sensitive technique, then it is possible that the concentration of Li was low and/ or Li was not detected on the surface of the sample. The oxidation states and peak separation energies of Zn, Sn and S (Figure 3.11 b – d) from high-resolution XPS of

LZTS nanoparticles were similar to those obtained from the same elements found in CZTS.

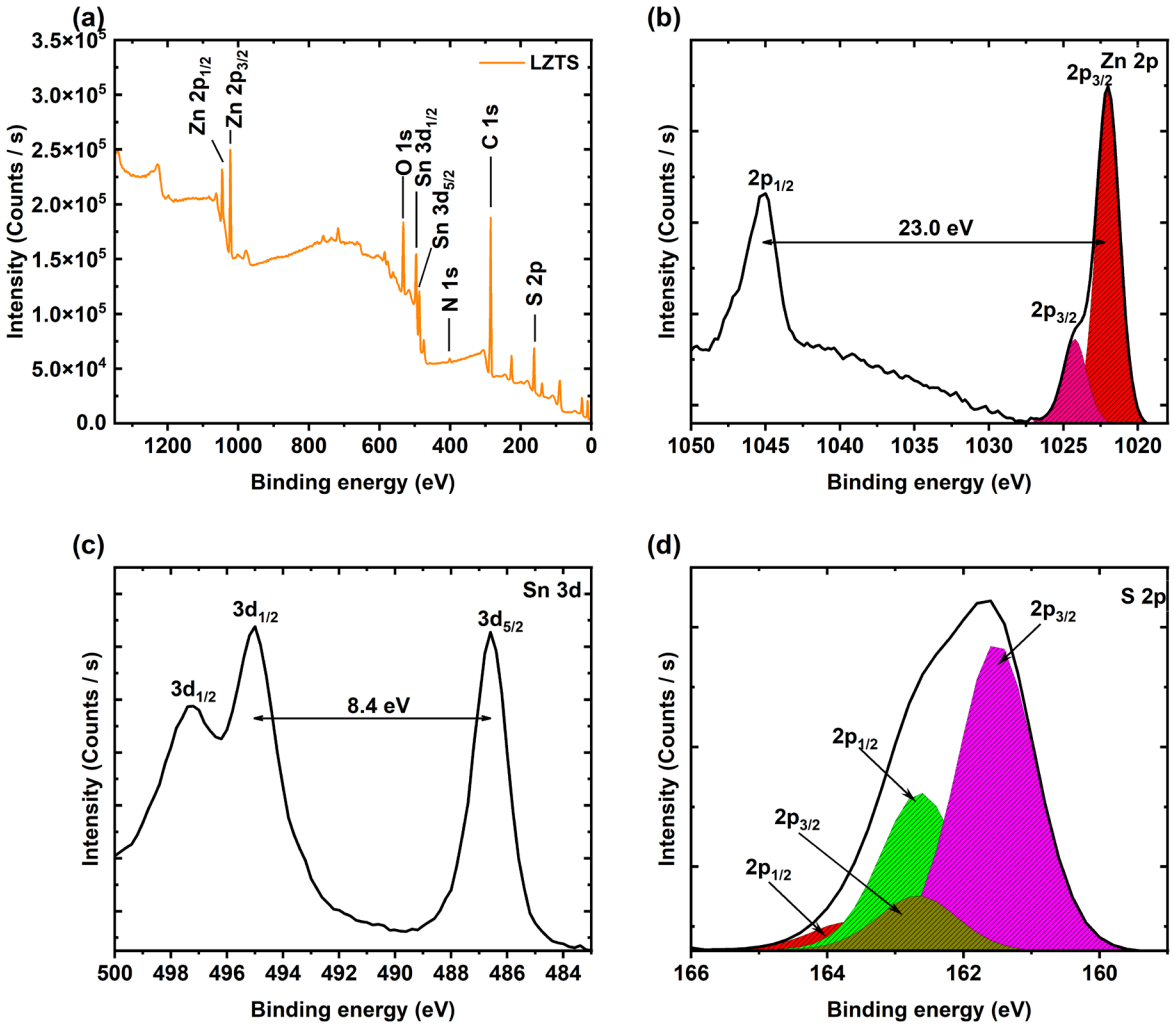

Figure 3.11: (a) XPS survey spectrum and high-resolution spectra of (b) zinc, (c) tin and (d) sulphur from LZTS nanoparticles.

The constituents of the caping agents from the high-resolution XPS in Figure 3.12 were similar to those found in Figure 3.10. However, all the constituents of the capping agent OLA in LZTS had less % atomic composition compared to those found in CZTS (the table of atomic compositions obtained from XPS analysis is given in Table S3.1–S3.3 of the appendix section).

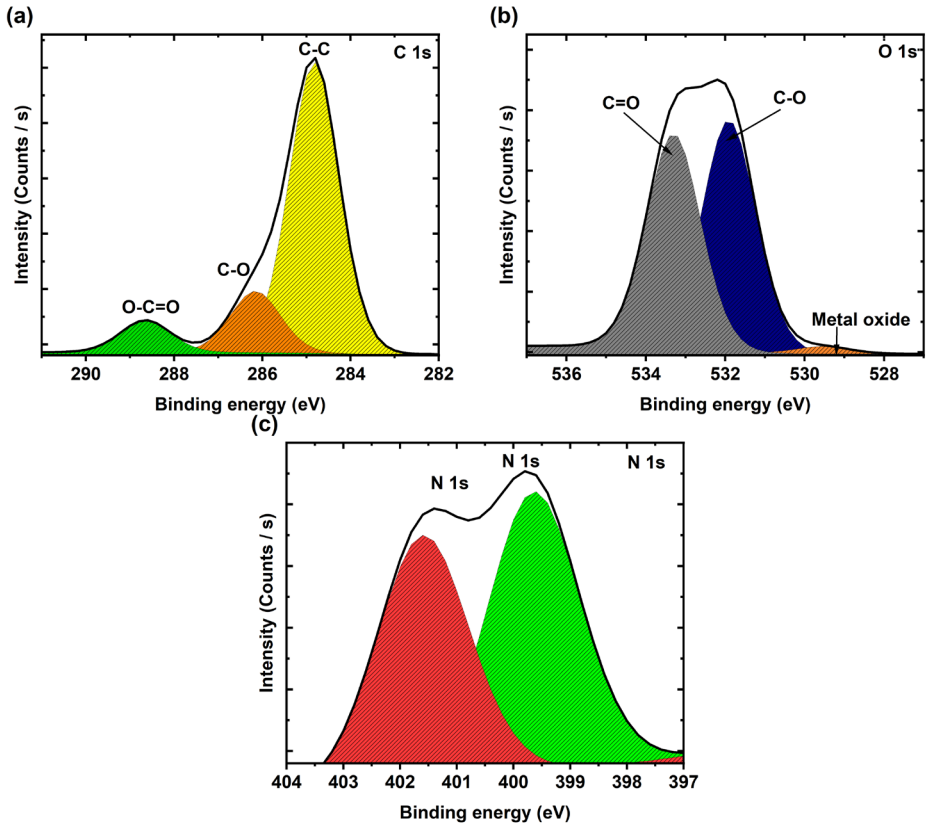

Figure 3.12: High-resolution spectra of (a) carbon, (b) oxygen and (c) nitrogen from LZTS nanoparticles.

3.4.6.3. NZTS

The XPS survey spectrum (Figure 3.13a) shows the elements present in the NZTS nanoparticles which are sodium, chlorine, zinc, tin, sulphur, carbon, oxygen and nitrogen atoms. In Figure 3.13 (b), the high-resolution spectra of Na 1s showed the presence of Na atoms, indicating that there was sufficient Na present for the successful formation of NZTS. Cl 2p peaks with a peak energy separation of 1.6 eV were detected by high-resolution XPS at 198.8 eV (Cl $2p_{3/2}$) and 200.6 eV (Cl $2p_{1/2}$). Even though Cl had a small intensity in the survey spectrum, we can consequently conclude that both XPS and EDX were able to quantify the presence of Cl as an impurity formed during the synthesis of NZTS nanoparticles. The oxidation states and peak separation energies of Zn, Sn and S from high-resolution XPS of LZTS nanoparticles were similar to those obtained from the same elements in CZTS and LZTS. Furthermore, the high-resolution XPS of N 1s, O 1s and C 1s in Figure 3.14 (b – d), is indicative of the successful capping of the nanoparticles.

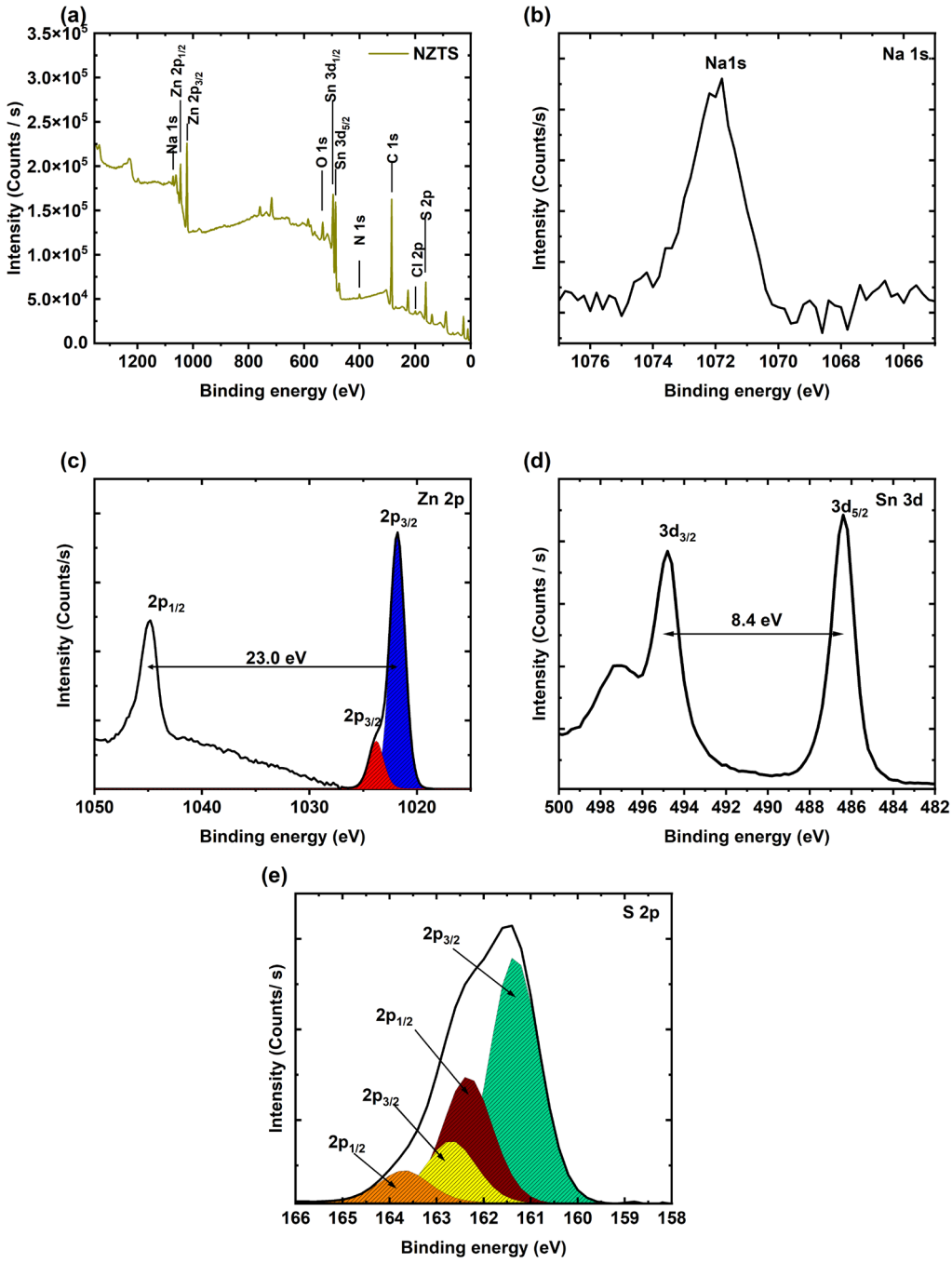

Figure 3.13: (a) XPS survey spectrum and high-resolution spectra of (b) sodium, (c) zinc, (d) tin and (e) sulphur from NZTS nanoparticles.

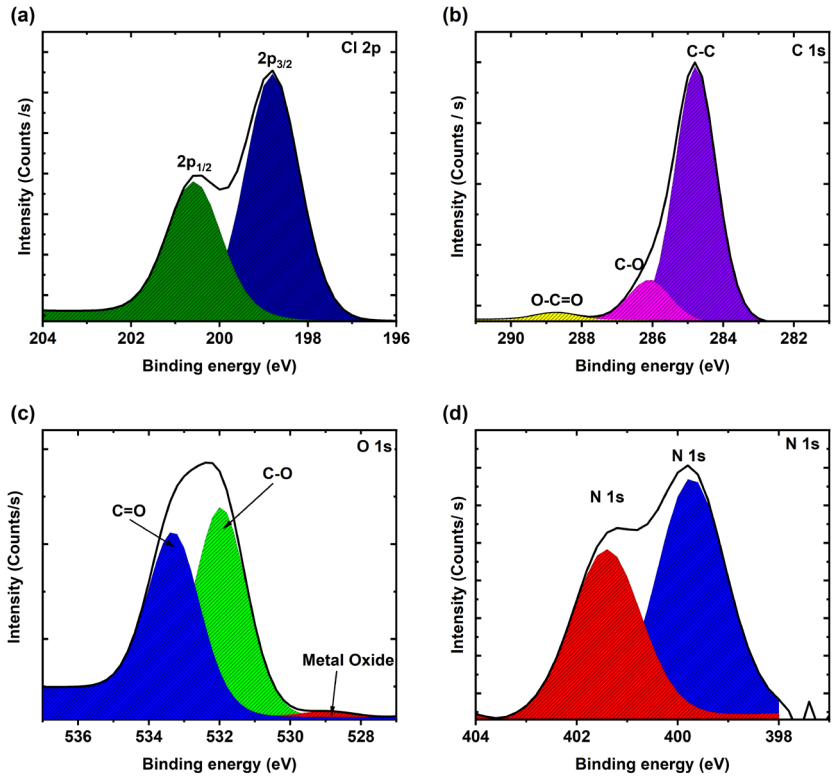

Figure 3.14: High-resolution spectra of (a) chlorine, (b) carbon, (c) oxygen and (d) nitrogen from NZTS nanoparticles.

3.4.7. Raman analysis

Raman spectroscopy is a useful method for a more precise identification of the structure of nanomaterials. In addition to providing precise information about the presence of binary phases (Cu_2S, Li_2S, Na_2S, ZnS) and ternary phases (Cu_2SnS_3, Li_2SnS_3 and Na_2SnS_3) present in CZTS, LZTS, and NZTS, this technique also offers information about the various phonon modes of a given material. Figure 3.15 displays each nanoparticle's Raman spectrum. Two prominent peaks in the Raman spectra of CZTS (Figure 3.15a) are situated at 331 cm^{-1} and 289 cm^{-1} represent the A_1 and A_2 vibration modes respectively [14,20]. According to studies, the reported prominent Raman peak positions for kesterite CZTS are between 331 cm^{-1} and 338 cm^{-1}, whereas the weak peak positions fall between 284 cm^{-1} and 289 cm^{-1} [21]. These findings thus support the single crystal nature of kesterite phase CZTS in the product.

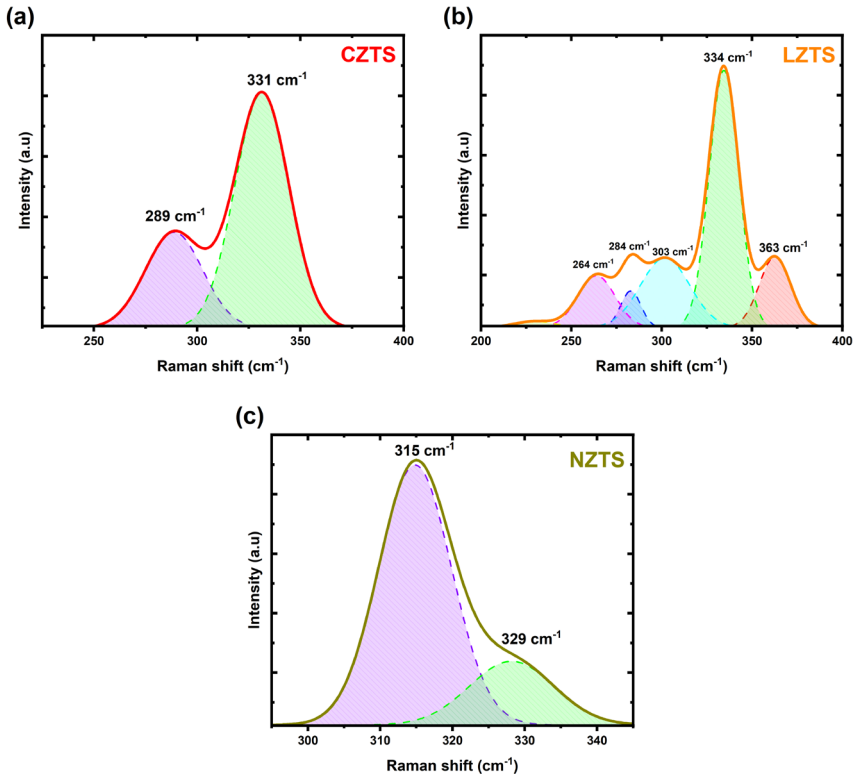

Figure 3.15: Raman spectra of (a) CZTS, (b) LZTS and (c) NZTS nanoparticles.

The Raman spectrum of LZTS (Figure 3.15b) indicated that the two major Raman peaks which are located at 334 cm^{-1} and 363 cm^{-1} may be the result of Sn-S vibrations, and a minor peak located at 284 cm^{-1} [9]. These two major peaks are close to the A_1 vibration mode and the 1 minor peak is close to the A_2 vibration mode of kesterite CZTS, thus these peaks could be ascribed to the kesterite phase of LZTS. The additional peak at 264 cm^{-1} can be attributed to the B_2 vibrational mode [22]. Therefore, we can conclude that the kesterite crystal structure of LZTS identified in the XRD analysis was also confirmed by Raman analysis.

The minor Raman peak located at 329 cm^{-1} for NZTS (Figure 3.15c) is close to the A_1 vibration mode of kesterite CZTS, thus these peaks could be ascribed to the kesterite phase of NZTS. The major peak at 315 cm^{-1} is close to the vibrational mode of Na_4SnS_4 reported by Bousselmi *et al.* [9]. In light of this, we can consequently conclude that NZTS was synthesized with Na_4SnS_4 as a possible secondary product. The intensity of the 315 cm^{-1} peak in comparison to that of the 329 cm^{-1} peak, further supports the statement made during XRD analysis of the NZTS sample that the cubic crystal structure is more dominant than the kesterite crystal structure of NZTS.

3.5. Conclusion

The nanoparticles synthesized through a low-cost colloidal synthesis method exhibited high crystallinity with distinct structural characteristics. CZTS adopted a kesterite crystal structure, while LZTS displayed a mixture of wurtzite and kesterite crystal structures. In contrast, NZTS presented a mixture of kesterite and FCC crystal structures. These structural properties were thoroughly analysed and confirmed using XRD, HRTEM and Raman spectroscopy.

The role of OLA as a capping agent was confirmed through FTIR and ^{1}H NMR, both of which demonstrated that the nanoparticles were capped via the nitrogen amine group of the capping agent. SSNMR provided further confirmation of the successful synthesis of LZTS and NZTS by identifying signature peaks corresponding to lithium and sodium, indicating the presence of these elements in the respective nanoparticles.

Elemental composition analyses using TEM-EDX and XPS revealed the constituent elements of all synthesized nanoparticles (except for Li which was difficult to detect using these techniques). This included the surface ligand OLA, where oxidation was observed. Even though Li atoms could not be detected by standard EDX mapping in this work, the advancements in HRTEM and scanning TEM (STEM), particularly with the recent introduction of aberration correction technology, have made it possible to directly observe Li atoms [27]. TEM analysis also indicated that the nanoparticles exhibited agglomeration and were polydispersed.

The optical properties of the synthesized nanoparticles were evaluated, and their band gaps were determined. The optical band gaps of CZTS, LZTS, and NZTS were found to be 3.42 eV, 3.07 eV, and 3.22 eV, respectively. These values highlight the potential applicability of the synthesized nanoparticles in various optoelectronic and energy-related applications.

In conclusion, this study successfully synthesized and characterized CZTS, LZTS, and NZTS nanoparticles using a cost-effective colloidal method, providing valuable insights into their structural, chemical, and optical properties. These findings contribute to the broader understanding of quaternary semiconducting nanoparticles and their potential applications in advanced material science.

3.6. References

[1] Rajesh, G.; Muthukumarasamy, N.; Subramanian, E. P.; Venkatraman, M. R.; Agilan, S.; Ragavendran, V.; Thambidurai, M.; Velumani, S.; Yi, J.; Velauthapillai, D. Solution-Based Synthesis of High Yield CZTS (Cu_2ZnSnS_4) Spherical Quantum Dots. *Superlattices and Microstructures* **2015**, *77*, 305–312.

[2] Lu, X.; Zhuang, Z.; Peng, Q.; Li, Y. Wurtzite Cu_2ZnSnS_4 Nanocrystals: A Novel Quaternary Semiconductor. *Chem. Commun.* **2011**, *47* (11), 3141–3143.

[3] Tiong, V.; Zhang, Y.; Bell, J.; Wang, H. Phase-Selective Hydrothermal Synthesis of Cu_2ZnSnS_4 Nanocrystals: The Effect of Sulphur Precursor. *CrystEngComm* **2014**, *16*, 4306–4313.

[4] Kannan, A. G.; Manjulavalli, T. E. Synthesis and Characterization of Cu_2ZnSnS_4 Nanoparticles. *Nanomaterials and Energy* **2015**, *4* (2), 118–123.

[5] Aldakov, D.; Lefrançois, A.; Reiss, P. Ternary and Quaternary Metal Chalcogenide Nanocrystals: Synthesis, Properties and Applications. *J. Mater. Chem. C* **2013**, *1* (24), 3756–3776.

[6] Ozel, F.; Kus, M.; Yar, A.; Arkan, E.; Can, M.; Aljabour, A.; Varal, N.; Ersoz, M. Fabrication of Quaternary Cu_2FeSnS_4 (CFTS) Nanocrystalline Fibers through Electrospinning Technique. *Journal of Materials Science* **2014**, *50*, 1573–4803.

[7] Berman, S.; Sai Gautam, G.; Carter, E. A. Role of Na and Ca as Isovalent Dopants in Cu_2ZnSnS_4 Solar Cells. *ACS Sustainable Chem. Eng.* **2019**, *7* (6), 5792–5800.

[8] Gour, K. S.; Singh, O. P.; Tawale, J. S.; Singh, V. N. Silver (Ag) Incorporated Cu_2ZnSnS_4 Thin Film for Improved Optical and Morphological Properties. *Superlattices and Microstructures* **2018**, *120*, 54–59.

[9] Bousselmi, G.; Khemiri, N.; Benali, A.; Graça, M. P. F.; Santos, R.; Costa, B.; Mounir, K. Synthesis and Study of Structural, Optical, and Electrical Properties of Nontoxic and Earth-Abundant Na_2ZnSnS_4 Material. *Journal of Materials Science Materials in Electronics* **2020**, *27*.

[10] El Radaf, I. M.; Al-Zahrani, H. Studies on the Structural, Optical, and Optoelectrical Properties of Innovative Li_2ZnSnS_4 Thin Films Deposited by Nebulizer Spray Pyrolysis. *Optical and Quantum Electronics* **2024**, *56*.

[11] Nwambaekwe, K. C.; Masikini, M.; Mathumba, P.; Ramoroka, M. E.; Duoman, S.; John-Denk, V. S.; Iwuoha, E. I. Electronics of Anion Hot Injection-Synthesized Te-Functionalized Kesterite Nanomaterial. *Nanomaterials* **2021**, *11* (3).

[12] Kolokoto, T.; Mashindi, V.; Kadzutu-Sithole, R.; Machogo-Phao, L. F. E.; Ndala, Z. B.; Shumbula, N. P.; Nkabinde, S. S.; Ngubeni, G. N.; Gqoba, S. S.; Mubiayi, K. P.; Moloto, N. The Effect of the Metal and Selenium Precursors on the Properties of $NbSe_2$ and Nb_2Se_9 Nanostructures and Their Application in Dye-Sensitized Solar Cells. *RSC Adv.* **2021**, *11* (50), 31159–31173.

[13] Cheng, J.; Dai, Z.; Chen, B.; Ji, R.; Yang, X.; Hu, R.; Zhu, J.; Li, L. Well-Dispersed Cu_2ZnSnS_4 Nanocrystals Synthesized from Alcohols and Their Applications for Polymer Photovoltaics. *Nanoscale Research Letters* **2016**, *11* (1), 550.

[14] Ngubeni, G. N.; Akinbami, O.; Mxakaza, L.; Nkabinde, S.; Kolokoto, T.; Otieno, F.; Moloto, M. J.; Mubiayi, K. P.; Moloto, N. Evaluating the Effect of the Substrate on the Electrocatalytic Performance of Cu_2ZnSnS_4 and Cu2ZnSnSe4 Counter Electrodes in Dye-Sensitized Solar Cells. *Thin Solid Films* **2022**, *745*, 139099.

[15] Alirezazadeh, F.; Sheibani, S. Facile Mechano-Chemical Synthesis and Enhanced Photocatalytic Performance of Cu_2ZnSnS_4 Nanopowder. *Ceramics International* **2020**, *46* (17), 26715–26723.

[16] Rajesh, G.; Muthukumarasamy, N.; Subramanian, E. P.; Venkatraman, M. R.; Agilan, S.; Ragavendran, V.; Thambidurai, M.; Velumani, S.; Yi, J.; Velauthapillai, D. Solution-Based Synthesis of High Yield CZTS (Cu_2ZnSnS_4) Spherical Quantum Dots. *Superlattices and Microstructures* **2015**, *77*, 305–312.

[17] Wang, J.; Zhang, P.; Song, X.; Gao, L. Surfactant-Free Hydrothermal Synthesis of Cu_2ZnSnS_4 (CZTS) Nanocrystals with Photocatalytic Properties. *RSC Adv.* **2014**, *4* (53), 27805–27810.

[18] Tiong, V.; Zhang, Y.; Bell, J.; Wang, H. Phase-Selective Hydrothermal Synthesis of Cu_2ZnSnS_4 Nanocrystals: The Effect of Sulphur Precursor. *CrystEngComm* **2014**, *16*, 4306–4313.

[19] Mxakaza, L.; Ngubeni, G.; Moloto, N.; Tetana, Z. Cu_2ZnSnS_4/N-MWCNTs Hybrid Systems as Counter Electrode Substitutes for Platinum in Dye-Sensitized Solar Cells. *Journal of Materials Research* **2024**, *39* (4), 689–701.

[20] Baskaran, P.; Nisha, K. D.; Harish, S.; Prabakaran, S.; Navaneethan, M.; Archana, J.; Ponnusamy, S.; Muthamizhchelvan, C.; Ikeda, H. High-Performance Electrocatalytic and Cationic Substitution in Cu_2ZnSnS_4 as a Low-Cost Counter Electrode for Pt-Free Dye-Sensitized Solar Cells. *J Mater Sci* **2021**, *56* (6), 4135–4150.

[21] Li, M.; Zhou, W.-H.; Guo, J.; Zhou, Y.-L.; Hou, Z.-L.; Jiao, J.; Zhou, Z.-J.; Du, Z.-L.; Wu, S.-X. Synthesis of Pure Metastable Wurtzite CZTS Nanocrystals by Facile One-Pot Method. *J. Phys. Chem. C* **2012**, *116* (50), 26507–26516.

[22] Baskaran, P.; Nisha, K. D.; Harish, S.; Prabakaran, S.; Navaneethan, M.; Archana, J.; Ponnusamy, S.; Muthamizhchelvan, C.; Ikeda, H. High-Performance Electrocatalytic and Cationic Substitution in Cu2ZnSnS4 as a Low-Cost Counter Electrode for Pt-Free Dye-Sensitized Solar Cells. *J Mater Sci* **2021**, *56* (6), 4135–4150.

[23] Dimitrievska, M.; Boero, F.; Litvinchuk, A. P.; Delsante, S.; Borzone, G.; Perez-Rodriguez, A.; Izquierdo-Roca, V. Structural Polymorphism in “Kesterite” Cu_2ZnSnS_4: Raman Spectroscopy and First-Principles Calculations Analysis. *Inorganic Chemistry* **2017**, *56* (6).

[24] Yu, K.; Carter, E. A. A Strategy to Stabilize Kesterite CZTS for High-Performance Solar Cells. *Chem. Mater.* **2015**, *27* (8), 2920–2927.

[25] Wu, H.; Chen, W. Synthesis and Reaction Temperature-Tailored Self-Assembly of Copper Sulfide Nanoplates. *Nanoscale* **2011**, *3* (12), 5096–5102.

[26] Lu, X.; Tuan, H.-Y.; Korgel, B. A.; Xia, Y. Facile Synthesis of Gold Nanoparticles with Narrow Size Distribution by Using AuCl or AuBr as the Precursor. *Chemistry – A European Journal* **2008**, *14* (5), 1584–1591.

[27] Muto, S.; Tatsumi, K. Detection of Local Chemical States of Lithium and Their Spatial Mapping by Scanning Transmission Electron Microscopy, Electron Energy-Loss Spectroscopy and Hyperspectral Image Analysis. *Microscopy* **2017**, *66* (1), 39–49.

[28] Mbuyazi, T. B.; Ajibade, P. A. Influence of Different Capping Agents on the Structural, Optical, and Photocatalytic Degradation Efficiency of Magnetite (Fe_3O_4) Nanoparticles. *Nanomaterials* **2023**, *13* (14), 2067.

Chapter 4: Elucidating the electrochemical properties of CZTS, LZTS and NZTS quaternary semiconductors for potential application as counter electrodes in dye-sensitized solar cells

4.1. Introduction

Counter electrodes with outstanding stability, low cost, and high efficiency are necessary for photoelectrochemical solar energy conversion. Photoelectrochemical solar cells rely on the efficient recovery of redox from the counter electrodes, which are essential components with good conductivity and high catalytic activity. Counter electrodes are an essential part of photoelectrochemical solar cells and must have strong catalytic activity and sufficient conductivity for effective redox recovery [1]. To date, the most commonly used counter electrode active material for dye-sensitized solar cells (DSSCs) has been platinum (Pt). But the expensive price of Pt-based materials prevents them from being developed further [2]. Researchers have made attempts to replace the Pt based counter electrode in order to address this problem. Quaternary semiconducting materials, such as CZTS and its analogues, derived from naturally occurring elements, have recently garnered significant attention for their potential use as Pt counter electrode substitutes due to their superior p-type electrochemical properties and good electrocatalytic activity [3,4]. Power conversion efficiencies (PCEs) of 3.9% for $Cu_2ZnSnSe_4$ (CZTSe) [5], 8.3% and 8.2% for Cu_2CoSnS_4 (CCTS) and Cu_2NiSnS_4 (CNTS) respectively [1], and the range of 3.14% – 7.56% for CZTS [6,7] have been reported when using CZTS and its analogues as counter electrodes in DSSCs.

Nanomaterials have been used in form of thin films or quantum dots in solar cell devices. A solution processing method was used in this study to prepare the quaternary semiconductor thin films [8]. In order to prepare the ink, quaternary semiconducting nanoparticles must first be synthesized and then dissolved in a non-polar solvent. After that, the ink is drop-cast onto a substrate to create a thin coating. The performance of the materials in a DSSC device is greatly influenced by the fabrication method used to make these thin films.

I was unable to find any literature that reports on the use of LZTS and NZTS as counter electrodes in DSSCs. Herein, CZTS, LZTS and NZTS thin films are fabricated, and several electrochemical parameters have been used in this work to assess the catalytic capabilities of the produced counter electrode materials for the potential application in DSSCs. The ionic and electronic processes occurring at the interface between the electrolyte and the counter electrode can be observed through using cyclic voltammetry measurements. Moreover, the kinetics of the electrochemical processes were assessed, using electrochemical impedance spectroscopy (EIS) measurements. Lastly, the interfacial charge-transfer characteristics between the counter electrode surfaces and the iodide/triiodide (I^-/I_3^-) electrolyte were examined using the Tafel polarization technique.

4.2. Experimental section

4.4.1. Chemicals

Lithium perchlorate ($LiClO_4$, ≥ 95%), lithium iodide (LiI, 99.9%), iodine (I_2, ≥99.8%), acetonitrile (99.5%), N-methyl-2-pyrrolidone (anhydrous NMP, 99.5%), toluene (anhydrous, 99.8%), glassy carbon electrode (GC, active area ~ 0.07 cm^2), fluorine doped tin oxide coated glass slide (FTO, surface resistivity ~7 Ω/sq). All chemicals were purchased from Sigma Aldrich and were used without any further purification.

4.2.2. Counter electrode preparation

Fluorine-doped tin oxide (FTO, 7 Ω/cm^2) cut into 1.4 by 1.4 cm pieces were washed by ultrasonicating in soap and rinsed with ultra-pure water, followed by further rinsing with acetone and isopropanol. Prior to use, FTO glass was dried with an air gun. The ink of the counter electrodes was separately prepared by dispersing 40 mg of CZTS, LZTS and NZTS nanoparticles in a mixture of 0.7 mL toluene and 0.3 mL NMP, which acted as a binder. After 24 h of vigorous stirring, the homogenous solutions were sonicated for 10 minutes. 5 – 10 µL of the inks were drop casted onto pre-cleaned GC electrode at room temperature. The GC electrode was then oven dried at 90 – 100 °C to form the counter electrode thin film. The counter electrodes on FTO were prepared in the same way, however 30 µL of the inks were drop casted onto pre-cleaned FTO glass substrate (area ~ 1.96 cm^2) at room temperature which were subsequently oven

dried at 90 – 100 °C to form the counter electrode thin film. For comparative studies, Pt was sputter coated onto FTO glass.

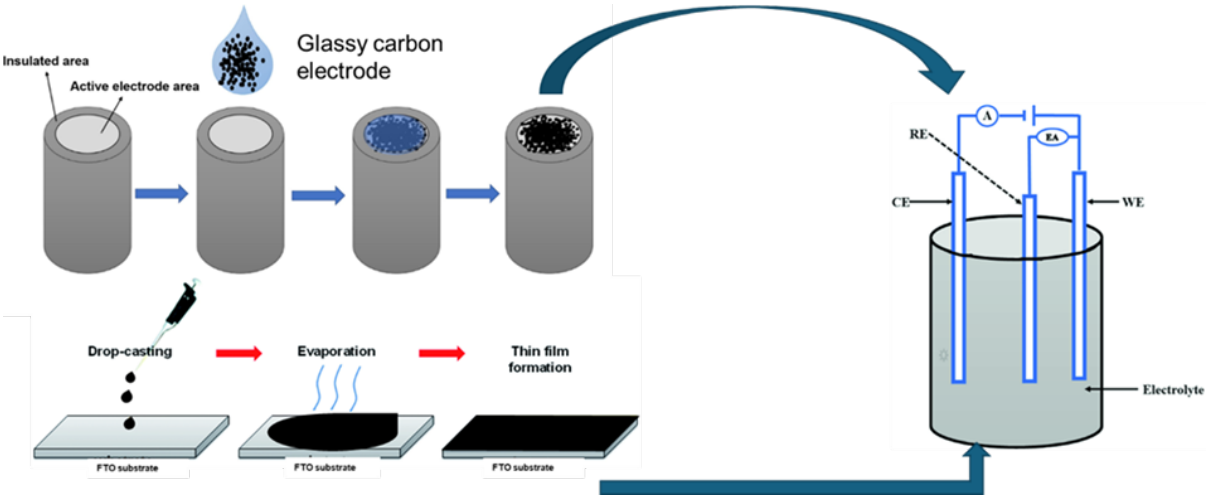

Figure 4.1: Setup for the preparation of the counter electrode and for electrochemical measurements.

4.3. Characterization

The surface roughness of the as-prepared counter electrodes was studied using Atomic Force Microscope (Nanosurf CoreAFM, Model BT02218). The Cressington 108 auto Sputter Coater was used to prepare sputter coated Pt thin films on FTO. Cyclic voltammetry (CV), electrochemical impedance spectroscopy (EIS), and Tafel polarization measurements were done using Biologic: VMP 300. A three-electrode system (Figure 4.1) was used to conduct the CV measurements using Pt as a counter electrode, Ag/AgCl as the reference electrode, the synthesized nanoparticles as the working electrode after being drop-casted on GC and the (I^-/I_3^-) electrolyte. The electrolyte was prepared by dissolving 0.135 g LiI (0.05 M), 0.05 g I_2 (0.02 M), and 1.05 g $LiClO_4$ (0.5 M) in 20 ml acetonitrile. In cyclic voltammetry, a potential between − 1.5 V to 1.5 V was applied between the working and reference electrodes and current response between the working and counter electrode recorded at increasing scan rates of 10, 25, 50, 75, and 100 mV/s. The stability of the working electrode in the electrolyte was evaluated by running 50 scans at the maximum scan rate of 100 mV/s.

EIS measurements were obtained using a symmetrical cell with two identical thin films on FTO in the redox electrolyte used for DSSCs in the dark. The electrodes were

analysed between 100 kHz and 100 MHz at varying open circuit potentials for each sample. The Tafel polarization analysis was conducted at a potential window of –1.0 to 1.0 V with a scan rate of 100 mV/s.

4.4. Results and discussions

4.4.1. Electrochemical analysis

4.4.1.1. Cyclic voltammetry studies

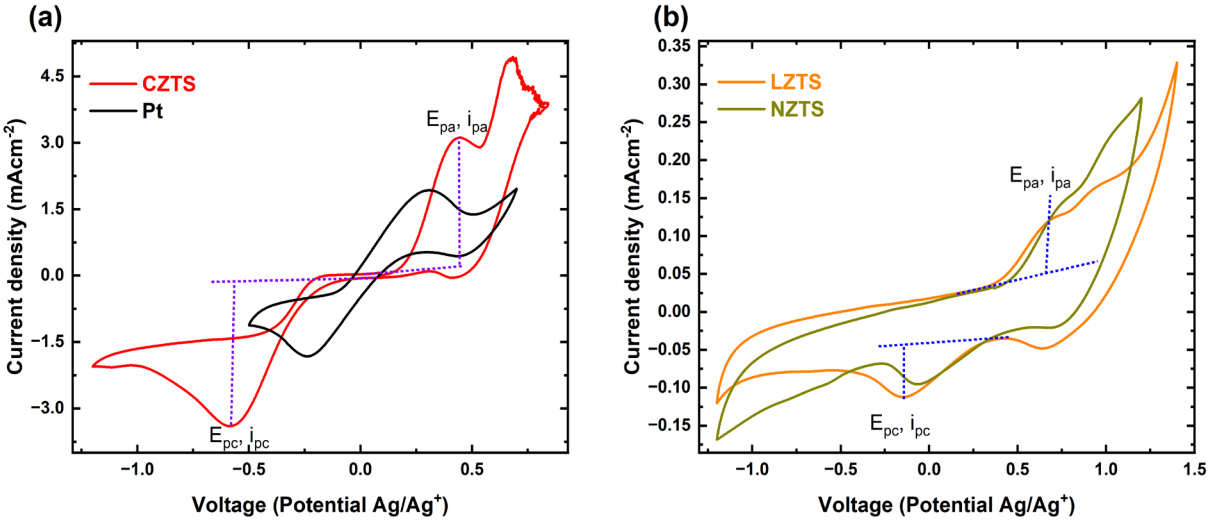

Figure 4.2: Cyclic voltammograms of (a) CZTS and Pt, (b) LZTS and NZTS at a scan rate of 50 mV/s on GC.

The electrocatalytic activity of CZTS, LZTS and NZTS counter electrodes under the I^-/I_3^- electrolyte was investigated by cyclic voltammetry (CV). The CV curves of the 4 different counter electrodes are composed of a pair of redox peaks and the CV curves are given in Figure 4.2. The first pair of redox peaks (top and bottom left-hand side peaks with the dotted lines on the CV plots) were attributed to oxidation and reduction reactions which are represented by equation (4.1). The second pair of peaks for CZTS, LZTS and NZTS (right-hand side of the CV plots) corresponded to the reaction represented by equation (4.2).

$$I_3^- + 2e^- \leftrightarrow 3I^- \qquad (4.1)$$

$$3I_2 + 2e^- \leftrightarrow 2I_3^- \qquad (4.2)$$

The Pt was scanned within the potential range of -0.5 V to 0.5 V, while CZTS, LZTS, and NZTS were scanned within the potential range of -1.5 V to 1.5 V. This is due to no oxidation or reduction reactions were occurring outside the potential range of -0.5 V to 0.5 V for Pt, as the CV curve showed no peaks beyond this region.

The peak-to-peak separation (ΔE_{pp}) and the cathodic peak current density (J_{pc}) are two important parameters that determine the catalytic activity of a material [2]. Additionally, the reversibility of the redox reaction is indicated by the peak-to-peak separation between the first reduction peak (i_{pc}) and oxidation peak (i_{pa}) [10]. Generally, a larger J_{pc} and a smaller ΔE_{pp} between anodic and cathodic CV peaks indicates good electrocatalytic activity of a counter electrode [5,10,11]. Furthermore, reduction specifies the redox peaks that have a significant impact on the photovoltaic performance of a DSSC while oxidation has a minor effect on a DSSC's performance [12].

Table 4.1: Parameters obtained from the cyclic voltammetry of the three-electrode half-cell setup.

Counter electrode	J_{pc} $(mAcm^{-2})$	$\Delta E_{pp}(V)$
CZTS	3.40	1.03
LZTS	0.112	0.807
NZTS	0.0954	0.792
Pt	1.82	0.546

From the results in Table 4.1, CZTS had the highest current density which indicated a superior electrocatalytic activity and a faster redox reaction rate for the I^-/I_3^- redox couple compared to the LZTS and NZTS. This may be due to the highly stable kesterite crystal structure of CZTS. However, when Cu atoms are replaced with Li and Na atoms into the kesterite structure, the LZTS and NZTS electrodes show both lower cathodic and anodic peak current densities than the CZTS electrodes.

LZTS and NZTS had similar ΔE_{pp}values which demonstrated that these catalysts needed the same amount of energy to complete the reduction process. However, a larger ΔE_{pp} for CZTS suggested that this electrode required more energy for facilitating the electrolyte reduction process.

By using successive cycle voltammetry scanning for 50 consecutive redox cycles at a maximum scan rate of 100 mV/s, the stability and repeatability of the prepared counter electrodes was studied. The resulting curves are shown in Figure 4.3 (a – c). The changes in reduction peak current density after 50 cycles are presented in Figure 4.3 (d). The stability study clearly indicates that the prepared counter electrodes were not stable, as observed by the decline in current densities with an increasing number of scan cycles. The stability of the counter electrodes may have been affected by a poor interaction of the prepared ink solution with the glassy carbon electrode which resulted in some of the deposited nanoparticles being washed off from the electrode surface after several CV cycles. By comparison, of the three counter electrodes, the stability ranking of the counter electrode materials is as follows: NZTS < CZTS < LZTS.

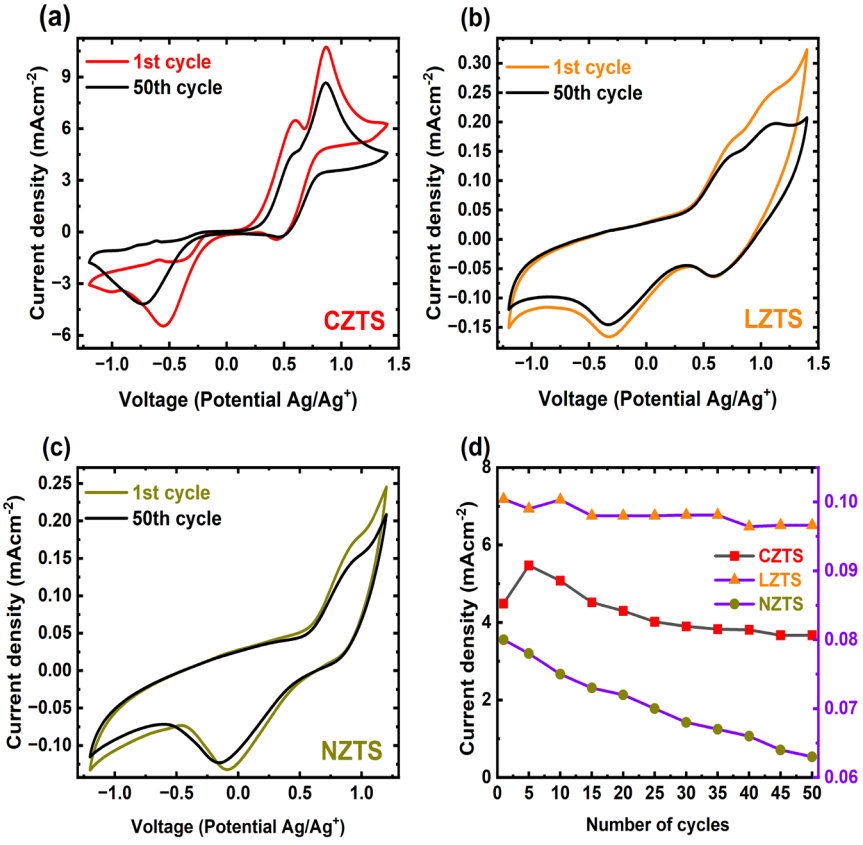

Figure 4.3: (a) – (c) Stability assessment of the prepared CZTS, LZTS & NZTS counter electrodes after 50 cycles at 100 mV/s on GC and (d) relationship between the number of CV scans at the obtained current density (black y-axis for CZTS and purple y-axis for LZTS and NZTS).

The performance of the counter electrodes under various scan rate conditions was examined and the results are depicted in Figure 4.4 (a – c). As the scan rate increased, the current density and ΔE_{pp} increased for all of the counter electrodes. The Randles–Sevcik equation, which is provided below, shows a relationship between the square root of the scan rate and the current density.

$$J_{pc} = 0.4463 \cdot A \cdot C \cdot \left(\frac{n^2 \cdot F^3 \cdot v \cdot D_o}{RT}\right)^2 \quad (4.3)$$

where D_o is the diffusion coefficient, v is the scan rate, F is Faraday's constant, R is the gas constant, T is the temperature (298 K), J_{pc} is the peak current density, C is the electrolyte concentration, n is the number of electrons transferred, and A is the electrode area. A high overpotential and poor reversibility are thus the effects of increasing the scan rate, which also results in the diffusion layer's thickness to decrease and electrochemical polarization to increase [11,13]. The counter electrodes in Figure 4.4 (a – c) showed that the square root of the scan rate had a linear relationship with the current density at both the anode and cathode. This linearity is evident in the plots with R^2 values being approximately equal to 1 in Figure 4.4 (d – f). The oxidation reaction occurring on the anode of CZTS counter electrode was not efficient for this material as it did not follow the linear relationship between current density and the square root of the scan rate due to the R^2 value being equal to 0.0505. The stability of the material under oxidation reactions could have affected how efficient the counter electrode was during an oxidation reaction. Furthermore, there was no specific interaction between the I^-/I_3^- redox couple and the counter electrodes; rather, the linear relationship between current density and the square root of the scan rate showed that ionic diffusion-controlled transport dominated the reaction of the I^-/I_3^- redox couple at both counter electrodes [11,14].

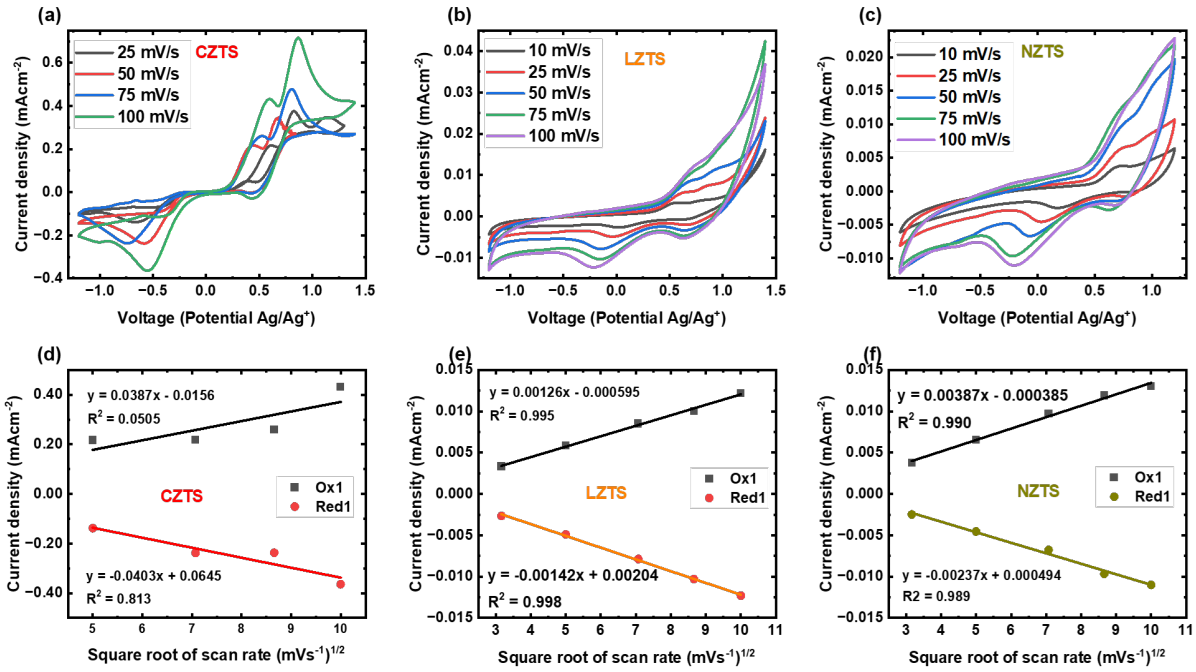

Figure 4.4: Cyclic voltammograms of (a) CZTS, (b) LZTS, (c) NZTS counter electrodes on GC at varying scan rates from 10 mV/s to 100 mV/s and (d) – (f) relationship between the square root of the counter electrodes' scan rates and the anodic and cathodic peak currents.

4.4.1.2. Electrochemical impedance studies

The performance of counter electrode materials in DSSC devices depends not only on their catalytic activity but also on their electrical conductivity [2]. Electrochemical impedance spectroscopy (EIS) is a highly effective and widely used tool for investigating charge transfer processes and evaluating the catalytic activity of a catalyst. These measurements were conducted under dark conditions on symmetrical dummy cells with two identical electrodes sandwiching the I^-/I_3^- electrolyte. The symmetric cell structure had the following sequence: counter electrode / electrolyte / counter electrode. The EIS data of CZTS, LZTS, NZTS and Pt are presented in Figure 4.5 (a) as Nyquist plots. The equivalent circuit Figure 4.5 (b) was used to fit the EIS results, and the circuit shows components that represent four impedance parameters namely R_s, R_{CT}, Z_w and Q_2. Where R_s is the series resistance, R_{CT} is the charge transfer resistance at an interface between the counter electrode and the electrolyte,

Z_w is the impedance of the Warburg diffusion element and Q_2 is the constant phase element [15,16].

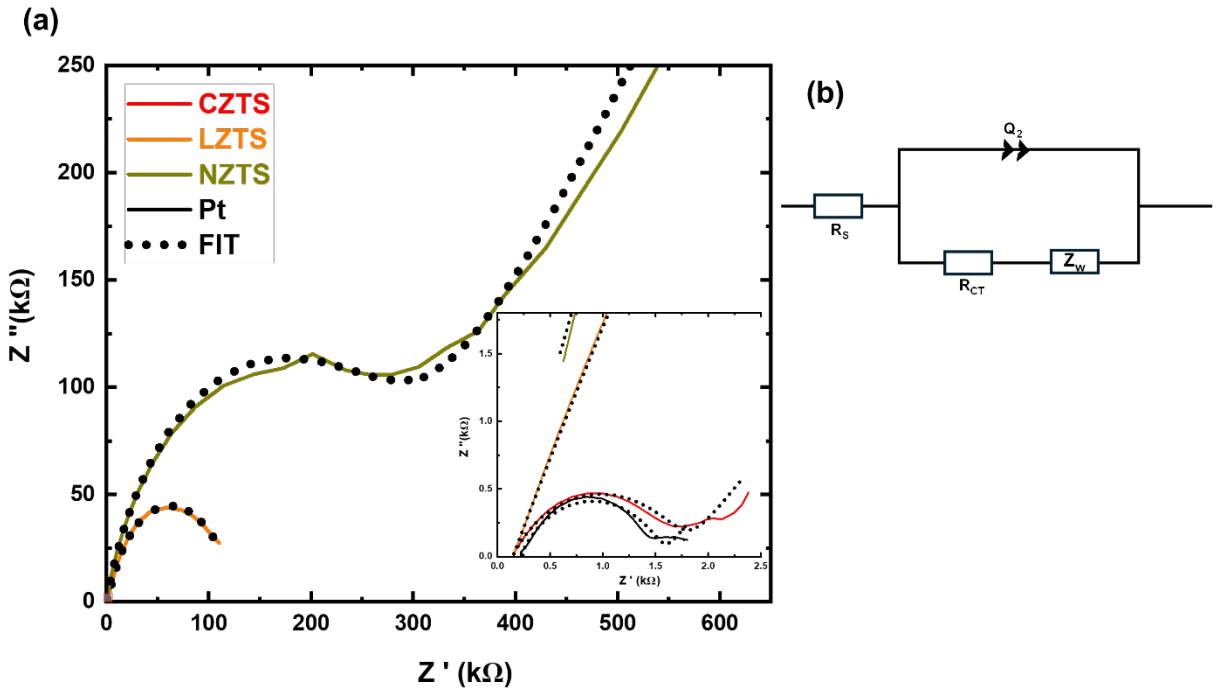

Figure 4.5: (a) Nyquist plot and (b) equivalent circuit used to fit EIS results for the symmetric cells fabricated with two identical electrodes of CZTS (*insert*), LZTS, NZTS and Pt (*insert*) on FTO.

The two important parameters, R_{CT}, and R_s are summarised in Table 4.2 for each counter electrode. Literature states that the conductivity of the counter electrode material increases with a decreased R_s value [11,15]. The following conductivity trend was observed Pt < LZTS < CZTS < NZTS. This suggested that NZTS was the most conductive compared to LZTS, CZTS and Pt. However, it is worth noting that conductivity can be mainly affected by the conductive substrate when there is lack of adhesive strength between the nanoparticle counter electrode layer and the FTO conductive glass substrate, resulting in a change of contact resistance thus altering the conductivity of the electrode [11]. Therefore, the quality of the thin films significantly affects some of the electrical properties of materials. The R_{CT} value for CZTS was far much lower than that of LZTS and NZTS, thus suggesting that CZTS had better charge transfer kinetics. A DSSC device's performance efficiency would be improved by lower R_{CT} values since they would lead to greater J_{sc} and FF values [13,15,17].

Table 4.2: Summary of the electrochemical performance parameters obtained from EIS.

Counter electrode	R_S (Ω)	R_{CT} (kΩ)
CZTS	142.7	1.64
LZTS	147.4	125.2
NZTS	52.7	290.4
Pt	218.8	1.36

4.4.1.3. Tafel polarization studies

To learn more about the catalytic activity of the counter electrodes, Tafel polarization measurements were conducted on the symmetric cells. Plots of the logarithmic current density (log *J*) against potential (V) at room temperature are displayed in Figure 4.6. The Tafel plots allow us to determine the numerical value of the limiting diffusion current density (J_{lim}) and the numerical value of the exchange current density (J_0), which are indicative of the counter electrodes' catalytic activity.

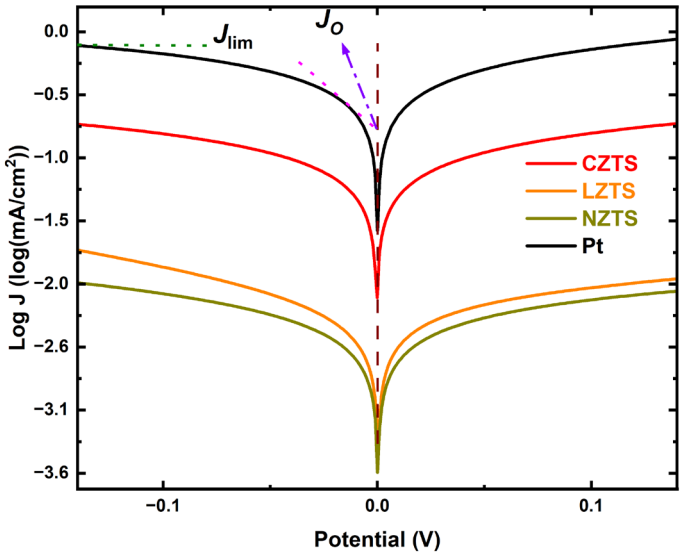

Figure 4.6: Tafel polarization curves for the symmetric cells fabricated with two identical electrodes of CZTS, LZTS, NZTS and Pt on FTO.

J_0 and J_{lim} values increased in the following order, as shown in Table 4.3: NZTS < LZTS < CZTS < Pt. Furthermore, the following equation shows a relationship between the charge transfer resistance and the exchange current density.

$$J_0 = \frac{\mathrm{RT}}{\mathrm{nFR_{CT}}} \tag{4.4}$$

where T is the temperature, n is the number of electrons involved in the reaction, F is the Faraday constant, and R is the gas constant. Based on equation 4.4, R_{CT} has an inverse relationship with J_0. As a result, J_0 and the counter electrode's electrocatalytic activity can be correlated; a higher J_0 indicates a significantly higher catalytic activity [10–11,13].

$$J_{lim} = \frac{2nFCD_n}{l} \tag{4.5}$$

Likewise, according to equation 4.5, a higher J_{lim} value denotes a bigger diffusion coefficient D value, which may lead to increased catalytic activity. In summary, the results from the Tafel polarization curves and EIS indicate that the order of catalytic activity is: NZTS < LZTS < CZTS < Pt, which is in agreement with the CV data.

Table 4.3: Electrochemical performance parameters from EIS & Tafel polarization curves for the counter electrodes.

Counter electrode	R_S (Ω)	R_{CT} (kΩ)	Log J_0 (log(mA/cm^2))	Log J_{lim} (log(mA/cm^2))
CZTS	142.7	1.64	-1.46	-0.746
LZTS	147.4	125.2	-2.65	-1.77
NZTS	52.7	290.4	-2.78	-2.04
Pt	218.8	1.36	-0.774	-0.109

4.4.2. Atomic force microscopy analysis

The surface topology of all the thin films is composed of spherical shaped agglomeration of small grains evolved in 2D atomic force microscopy (AFM) images

and it is clearly seen that the grains have good connectivity that resemble cluster-like or mountain-like structures as seen 3D AFM images of Figure 4.7. To measure the surface roughness with AFM, the root mean square (rms) was used. The rms roughness depicts the standard deviation of the AFM profile from the surface height [18]. Furthermore, roughness could influence electrocatalysis activity, but interfacial losses have also been demonstrated to impact the performance of the solar cell. [10]. The rms values for CZTS, LZTS and NZTS thin films were 138.23 nm, 22.49 nm and 67.95 nm respectively. Additionally, as observed for this study and a previous study by Fan *et al.* 2015, a rough surface with a high rms value would give the desired efficiency in a DSSC as observed from the electrochemical measurements. Since CZTS showed the highest rms value, this implies that it could have the largest electrocatalytic surface area for the reduction of the I^-/I_3^- electrolyte [19]. This could explain why CZTS was the best performing counter electrode compared to LZTS and NZTS.

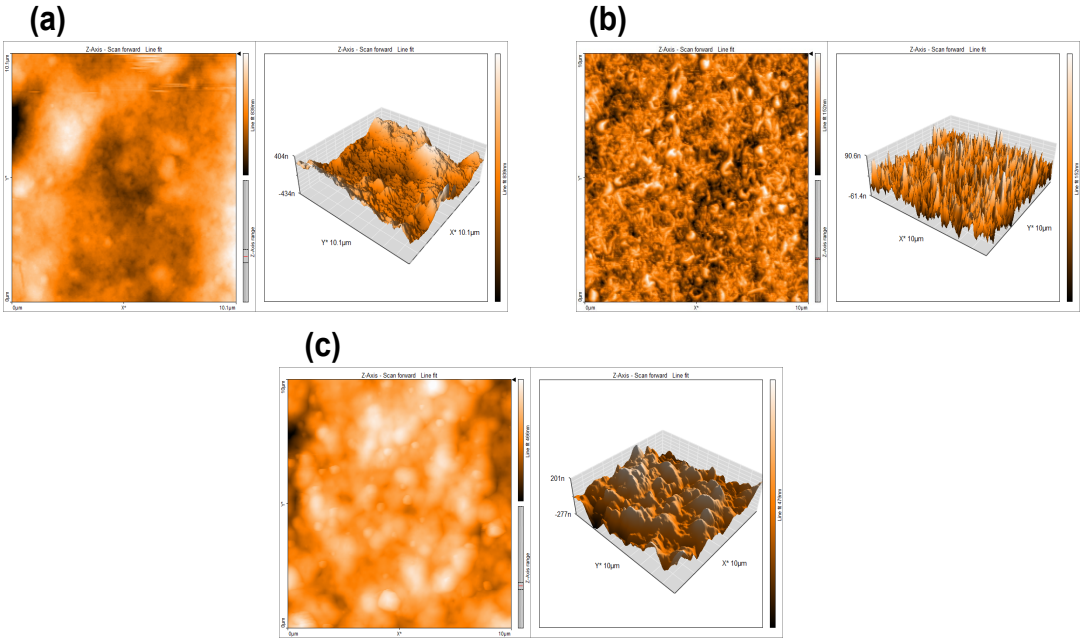

Figure 4.7: 2D and 3D AFM micrographs of (a) CZTS, (b) LZTS and (c) NZTS thin films on FTO substrate.

4.5. Conclusion

The CZTS, LZTS, and NZTS nanoparticles synthesized in the previous chapter were successfully transformed into thin film counter electrodes using a straightforward and

relatively reproducible drop-casting technique. The fabrication process involved preparing a nanomaterial ink, consisting of the nanoparticles, an organic solvent (toluene), and a binding solvent (NMP). The separate inks were then drop-casted onto individual GC and FTO substrates respectively.

To evaluate the suitability of these thin films as counter electrodes for potential application in DSSCs, their electrocatalytic properties were thoroughly investigated using various electrochemical characterization techniques and AFM.

Cyclic voltammetry (CV) measurements revealed that CZTS also exhibited the highest current density among the three counter electrodes. This indicates a faster redox reaction rate and better electrocatalytic activity for the I^-/I_3^- redox couple compared to LZTS and NZTS. Stability tests, however, showed a different trend, with LZTS demonstrating the highest stability, followed by CZTS and then NZTS. This stability ranking underscores the potential trade-offs between catalytic performance and long-term durability in these materials. Additionally, the linear relationship observed between current density and the square root of scan rate for all three counter electrodes confirmed that their electrocatalytic behaviour aligns with the Randles–Sevcik equation, reinforcing the reliability of the electrochemical findings.

EIS and Tafel polarization studies supported the CV data, further confirming the relative electrocatalytic performance of the counter electrodes. The overall order of electrocatalytic activity was established as NZTS < LZTS < CZTS < Pt, indicating that while CZTS showed the best performance among the synthesized materials, it still fell short of the benchmark Pt counter electrode.

AFM analysis provided insights into the surface morphology of the thin films and suggested that CZTS exhibited the most desirable surface characteristics for counter electrode performance, as evidenced by its highest rms roughness value. The superior rms value suggests that CZTS provides a larger surface area, potentially enhancing its electrocatalytic activity compared to LZTS and NZTS. The roughness trend follows the order: LZTS < NZTS < CZTS. However, there is a discrepancy between the roughness trend and the conclusion drawn from the electrochemical activity of NZTS. The presence of a secondary product in the NZTS sample may have negatively affected the performance of the material thus contributing to the observed inconsistency in the trend.

In summary, this study demonstrated that CZTS, LZTS, and NZTS nanoparticles can be effectively converted into thin-film counter electrodes with promising electrocatalytic properties for DSSC applications. CZTS stood out as the most catalytically active material, while LZTS exhibited superior stability. These findings highlight the potential of these materials for future DSSC development, with further optimization required to enhance their overall performance.

4.6. References

[1] Lu, S.; Yang, H.; Li, F.; Wang, Y.; Chen, S.; Yang, G.; Liu, Y.; Zhang, X. Element Substitution of Kesterite Cu_2ZnSnS_4 for Efficient Counter Electrode of Dye-Sensitized Solar Cells. *Scientific Reports* **2018**, *8* (1), 8714.

[2] Kong, J.; Zhou, Z.-J.; Li, M.; Zhou, W.-H.; Yuan, S.-J.; Yao, R.-Y.; Zhao, Y.; Wu, S.-X. Wurtzite Copper-Zinc-Tin Sulfide as a Superior Counter Electrode Material for Dye-Sensitized Solar Cells. *Nanoscale Res Lett* **2013**, *8* (1), 464.

[3] Roy, A.; Sundaram, S.; Mallick, T. K. Cu_2ZnSnS_4, a Fascinating Counter Electrode for TiO2-Free Dye-Sensitized Solar Cells. *ChemistrySelect* **2021**, *6* (7), 1541–1547.

[4] Agasti, A.; Nemala, S. S.; Mallick, S.; Bhargava, P. Stability Study of Co-Electrodeposited CZTS Counter Electrode for Dye Sensitized Solar Cells. *Solar Energy* **2018**, *176*, 325–333.

[5] Imla Mary, C.; Senthilkumar, M.; Manobalaji, G.; Moorthy Babu, S. Solution Processed Cu2ZnSnSe4 Nanoink for Inexpensive Pt-Free Counter Electrode in Dye-Sensitized Solar Cells. *Solid State Sciences* **2021**, *116*, 106612.

[6] Mokurala, K.; Kamble, A.; Bhargava, P.; Mallick, S. Fabrication of Dye Sensitized Solar Cells with Cost-Effective Quaternary Sulfide Counter Electrode. In *2014 IEEE International Conference on Power Electronics, Drives and Energy Systems (PEDES)*; **2014**; pp 1–4.

[7] S. Chen, X. Z.; Tao, J.; Tao, H.; Shen, Y.; Zhu, L.; Jiang, J.; Wang, T. Fabrication of Low Cost Kesterite Cu_2ZnSnS_4 (CZTS) Thin Films as Counter-Electrode for Dye Sensitised Solar Cells (DSSCs). *Materials Technology* **2015**, *30* (5), 306–312.

[8] Ahn, B. D.; Jeon, H.-J.; Sheng, J.; Park, J.; Park, J.-S. A Review on the Recent Developments of Solution Processes for Oxide Thin Film Transistors. *Semiconductor Science and Technology* **2015**, *30* (6), 064001.

[9] Abdulrahman, Z.; AL-Shamkhee, D.; Al-murshedi, A.; Kamil, F.; Al-Manea, A.; Yusaf, T. Comparative Performances of Natural Dyes Extracted from Mentha Leaves, Helianthus Annuus Leaves, and Fragaria Fruit for Dye-Sensitized Solar Cells. *Designs* **2022**, *6*, 100.

[10] Airo, M. A.; Otieno, F.; Mxakaza, L.; Ipadeola, A.; Kadzutu-Sithole, R. S.; Machogo-Phao, L. F. E.; Billing, C.; Moloto, M.; Moloto, N. Probing the Stoichiometry Dependent Catalytic Activity of Nickel Selenide Counter Electrodes in the Redox Reaction of Iodide/Triiodide Electrolyte in Dye Sensitized Solar Cells. *RSC Adv.* **2020**, *10* (65), 39509–39520.

[11] Mposa, E.; Sithole, R. K.; Ndala, Z.; Ngubeni, G. N.; Mubiayi, K. P.; Shumbula, P. M.; Machogo-Phao, L. F. E.; Moloto, N. Novel 2D-AuSe Nanostructures as Effective Platinum Replacement Counter Electrodes in Dye-Sensitized Solar Cells. *RSC Adv.* **2022**, *12* (20), 12882–12890.

[12] Elindjeane Sheela, S.; Murugadoss, V.; Sittaramane, R.; Angaiah, S. Development of Tungsten Diselenide/Polyaniline Composite Nanofibers as an Efficient Electrocatalytic Counter Electrode Material for Dye-Sensitized Solar Cell. *Solar Energy* **2020**, *209*, 538–546.

[13] Kolokoto, T.; Mashindi, V.; Kadzutu-Sithole, R.; Machogo-Phao, L. F. E.; Ndala, Z. B.; Shumbula, N. P.; Nkabinde, S. S.; Ngubeni, G. N.; Gqoba, S. S.; Mubiayi, K. P.; Moloto, N. The Effect of the Metal and Selenium Precursors on the Properties of $NbSe_2$ and Nb_2Se_9 Nanostructures and Their Application in Dye-Sensitized Solar Cells. *RSC Adv.* **2021**, *11* (50), 31159–31173.

[14] Mxakaza, L.; Ngubeni, G.; Moloto, N.; Tetana, Z. Cu_2ZnSnS_4/N-MWCNTs Hybrid Systems as Counter Electrode Substitutes for Platinum in Dye-Sensitized Solar Cells. *Journal of Materials Research* **2024**, *39* (4), 689–701.

[15] Ngubeni, G. N.; Akinbami, O.; Mxakaza, L.; Nkabinde, S.; Kolokoto, T.; Otieno, F.; Moloto, M. J.; Mubiayi, K. P.; Moloto, N. Evaluating the Effect of the Substrate on the Electrocatalytic Performance of Cu_2ZnSnS_4 and $Cu_2ZnSnSe_4$Counter Electrodes in Dye-Sensitized Solar Cells. *Thin Solid Films* **2022**, *745*, 139099.

[16] Nwambaekwe, K. C.; Masikini, M.; Mathumba, P.; Ramoroka, M. E.; Duoman, S.; John-Denk, V. S.; Iwuoha, E. I. Electronics of Anion Hot Injection-Synthesized Te-Functionalized Kesterite Nanomaterial. *Nanomaterials* **2021**, *11* (3).

[17] Dissanayake, M. A. K. L.; Kumari, J. M. K. W.; Senadeera, G. K. R.; Jaseetharan, T.; Weerasinghe, J.; Anwar, H. A Low-Cost, Vein Graphite/Tin Oxide Nanoparticles

Based Composite Counter Electrode for Efficient Dye-Sensitized Solar Cells. *Materials Science and Engineering: B* **2021**, *273*, 115440.

[18] Dhas, C. R.; Christy, A. J.; Venkatesh, R.; Anuratha, K. S.; Ravichandran, K.; Raj, A. M. E.; Subramanian, B.; Panda, S. K. Nebulizer Spray-Deposited $CuInGaS_2$ Thin Films, a Viable Candidate for Counter Electrode in Dye-Sensitized Solar Cells. Solar Energy **2017**, 157, 58–70.

[19] Fan, M.-S.; Chen, J.-H.; Li, C.-T.; Cheng, K.-W.; Ho, K.-C. Copper Zinc Tin Sulfide as a Catalytic Material for Counter Electrodes in Dye-Sensitized Solar Cells. J. Mater. Chem. A **2015**, 3 (2), 562–569.

CHAPTER 5: Overall conclusions, recommendations and future work

5.1: Conclusions

This dissertation presents an extensive investigation into the colloidal synthesis and characterization of a Cu-based quaternary semiconductor, Cu_2ZnSnS_4 (CZTS), along with the first-ever reported colloidal synthesis of alkali metal-based analogues Li_2ZnSnS_4 (LZTS) and Na_2ZnSnS_4 (NZTS). These nanoparticles were successfully synthesized under optimized reaction conditions of 220 °C for 50 minutes, using oleylamine (OLA) as a capping agent. The role of OLA in capping the nanoparticles was confirmed through liquid-state nuclear magnetic resonance (NMR) spectroscopy and Fourier-transform infrared (FTIR) spectroscopy, which indicated that the capping occurred via the nitrogen amine group of the capping agent.

Energy dispersive X-ray (EDX) and X-ray photoelectron spectroscopy (XPS) further verified the elemental composition and oxidation states of the synthesized nanoparticles, identifying the presence of each element (i.e. Cu^{+}, Na^{+}, $Zn^{2+,}$ Sn^{4+} and S^{2-}). However, Lithium (Li) atoms were difficult to detect using standard EDX characterization technique as they are very light, and they also have a very low energy of characteristic radiation. Since it can examine the local chemical bonding environments of individual elements and works especially well with light elements such as Li, electron energy-loss spectroscopy (EELS) coupled to TEM is a viable substitute. Despite the observed agglomeration and polydispersity during transmission electron microscopy (TEM) analysis, this morphology is advantageous for solar cell applications, as it promotes particle interconnectedness and facilitates easier charge transport during the operation of a dye-sensitized solar cell (DSSC) device.

The crystal structures of the nanoparticles were analysed using structural characterization techniques. CZTS was found to adopt a stable kesterite crystal structure, while LZTS and NZTS exhibited mixed-phase crystal structures. LZTS showed a combination of kesterite and wurtzite crystal structures, and NZTS displayed a mixture of kesterite and cubic crystal structures. These variations in crystal structures are attributed to the substitution of Cu (atomic radius 128 pm) with larger

alkali metal ions, Li (atomic radius 152 pm) and Na (atomic radius 186 pm). This substitution not only altered the crystal structure but also significantly influenced the optical properties of the nanoparticles. The optical band gap of CZTS was measured at 3.42 eV, whereas the band gaps of LZTS and NZTS decreased to 3.07 eV and 3.22 eV, respectively, reflecting the impact of atomic substitution on the electronic properties of the materials.

Solid-state nuclear magnetic resonance (SSNMR) experiments provided further confirmation of the presence of Li and Na monovalent cations after the formation of LZTS and NZTS. Raman spectroscopy and other structural analyses such as High-resolution TEM (HRTEM) consistently validated the successful synthesis of the nanoparticles, affirming the robustness of the colloidal method for producing both CZTS and its novel alkali metal-based analogues.

The electrochemical properties of these materials were assessed through Tafel polarization, cyclic voltammetry (CV) and electrochemical impedance spectroscopy (EIS) studies. CV measurements indicated that all the synthesized counter electrodes underwent similar electrochemical processes to the platinum (Pt) counter electrode, as evidenced by distinct redox peaks corresponding to the reduction of the triiodide electrolyte. This suggests that CZTS, LZTS, and NZTS counter electrodes hold potential as alternatives to Pt-counter electrodes in DSSCs. However, based on the overall electrochemical performance, Pt remained the superior counter electrode. Among the synthesized materials, the order of electrocatalytic activity was determined as NZTS < LZTS < CZTS < Pt, with CZTS demonstrating the highest activity among the non-Pt materials.

In conclusion, this work establishes the colloidal method as a viable and efficient approach for synthesizing CZTS nanoparticles and introduces the novel synthesis of LZTS and NZTS nanoparticles. The study provides a comprehensive understanding of their structural, optical, and electrochemical properties, offering valuable insights into their potential applications as counter electrode materials in DSSCs. While Pt remains the benchmark, the promising properties of these quaternary semiconducting nanoparticles pave the way for further optimization and exploration in the field of renewable energy.

5.2: Recommendations and future work

- Explore the use of composites to try and improve the electrochemical properties of the synthesized quaternary semiconductors.
- Test the effects of post-synthesis ligand exchange reactions on the size, shape, and optical characteristics of the generated nanoparticles by removing the long chain organic ligand of OLA and substituting it with shorter chained ligands like ethanethiol or 3-mercaptopropionic acid.
- Investigate the effects of varying capping agents to see if they can affect the produced nanoparticles' size, shape, and optical and electrochemical properties.
- The type of preparation method used to make the thin film can influence the active surface area. Therefore, it is recommended to evaluate other thin film fabrication methods such as slot-die coating and spray coating instead of drop casting.
- Full optimization and fabrication of the DSSC device as well as further investigating the potential use of CZTS, LZTS and NZTS thin films as counter electrodes.

Appendix

Supporting information

Chapter 3

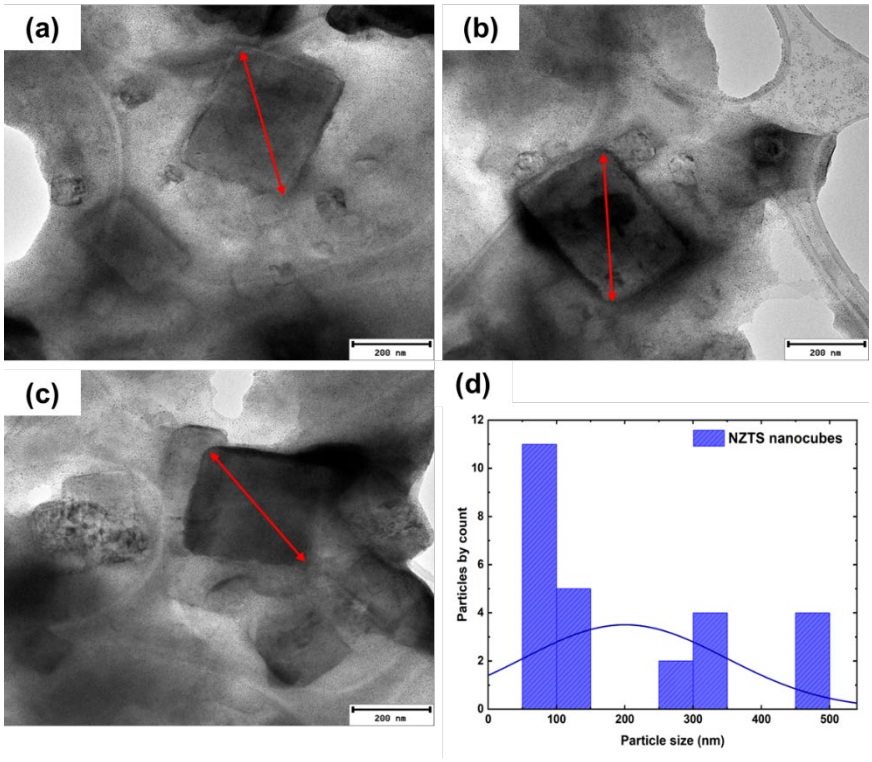

Figure S3.1: (a) - (c) TEM images of NZTS nanocubes and (d) particle size distribution histogram based on the diagonal lengths (red double arrow line) of the nanocubes.

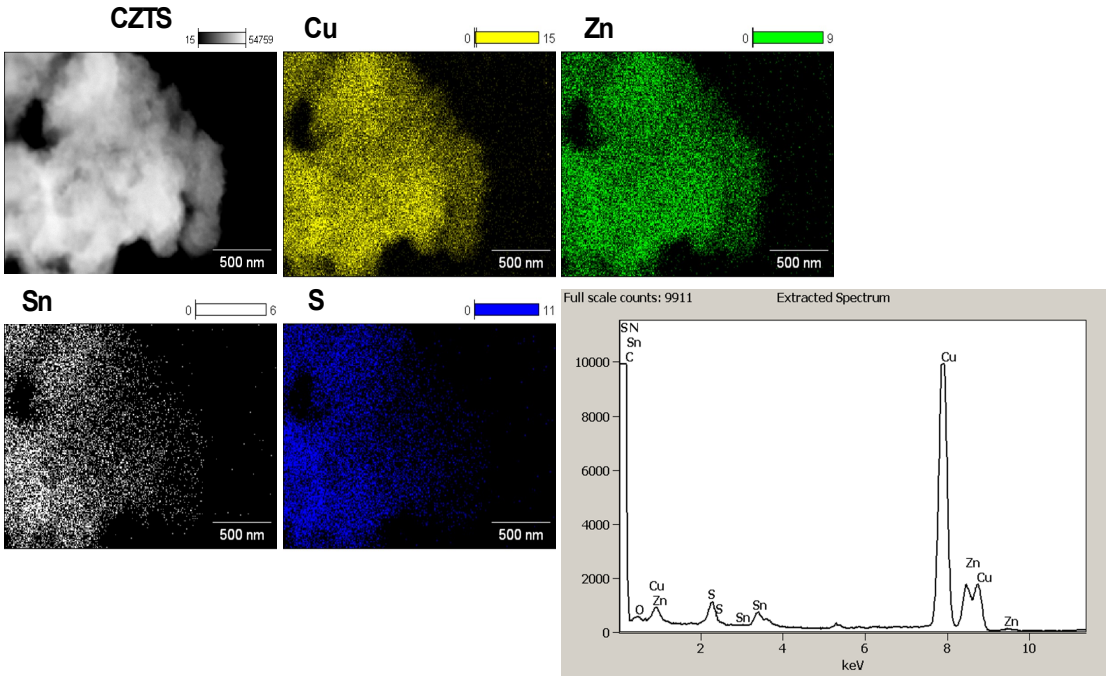

Figure S3.2: EDX mapping showing the elemental composition of CZTS nanoparticles along with the corresponding TEM micrograph of CZTS.

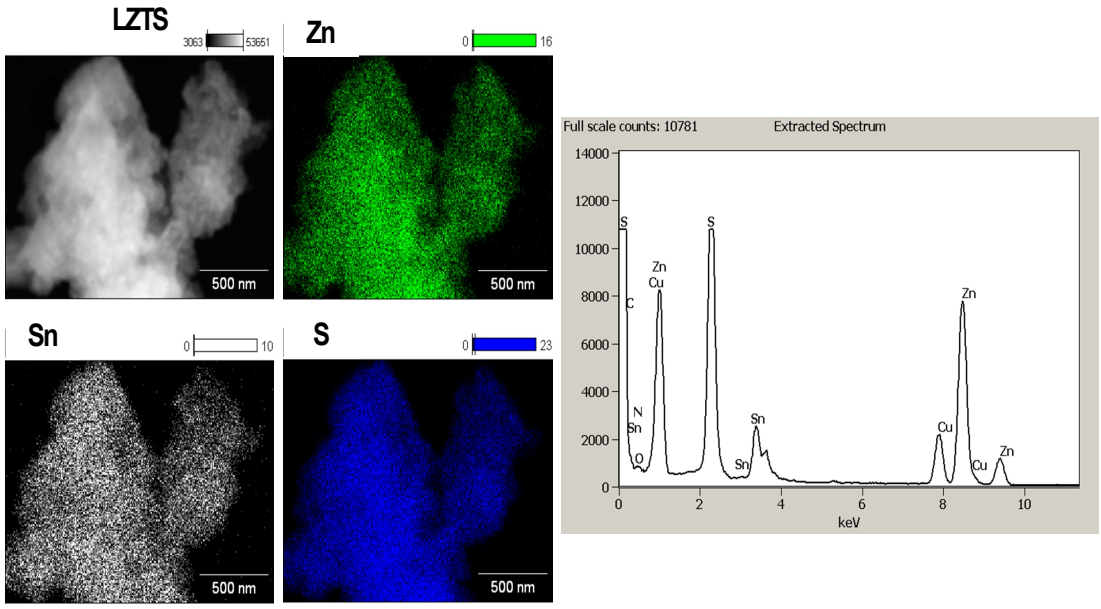

Figure S3.3: EDX mapping showing the elemental composition of LZTS nanoparticles along with the corresponding TEM micrograph of LZTS.

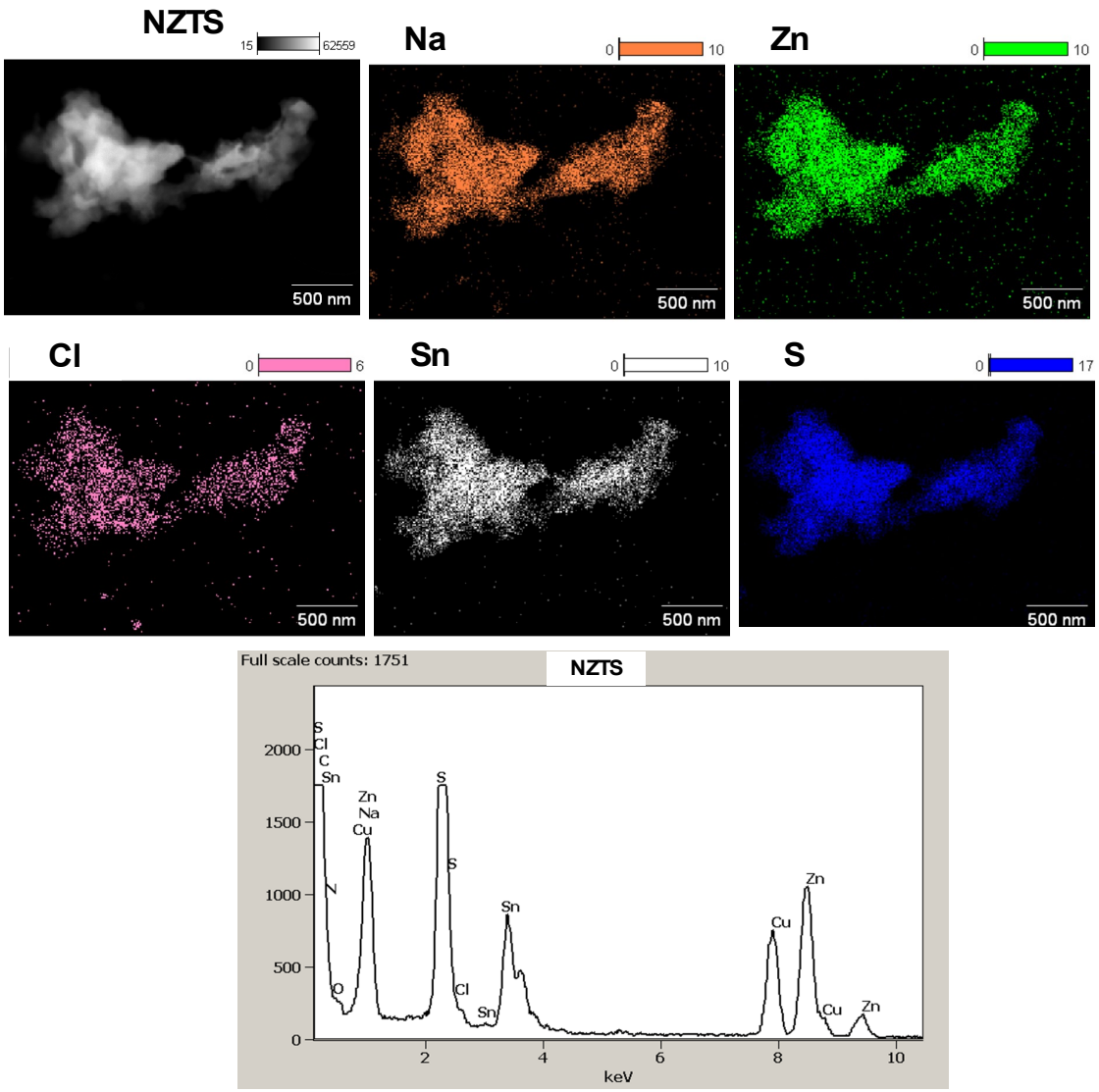

Figure S3.4: EDX mapping showing the elemental composition of NZTS nanoparticles along with the corresponding TEM micrograph of NZTS.

Table S3.1: Summary of the atomic composition stoichiometric assignments obtained from the fitting of the XPS spectra for CZTS.

Element	Assignment	Binding energy (eV)	Atomic %
C	C-C	284.8	58.96
	C-O	286.2	9.15
	O-C=O	288.7	3.96
O	C-O	531.9	7.82
	C=O	533.3	5.23
	Metal oxide	529.5	0.16
N	N 1s	400.5	0.72
		402.4	0.31
Cu	Cu 2p3	934	0.67
		932.1	2.03
Zn	Zn 2p	1022	0.64
Sn	Sn 3d5	486.3	1.39
		487.4	0.51
S	2p3	161.4	4.62
		162.2	2.5
		164.3	0.67
		168.3	0.67

Table S3.2: Summary of the atomic composition stoichiometric assignments obtained from the fitting of the XPS spectra for LZTS.

Element	Assignment	Binding energy (eV)	Atomic %
C	C-C	284.8	52.19
	C-O	286.2	11.03
	O-C=O	288.6	5.75
O	C-O	531.9	6.74
	C=O	533.3	6.24
	Metal oxide	529.6	0.21
N	N 1s	401.6	0.7
Zn	Zn 2p	1022	3.21
Sn	Sn 3d5	486.6	1.26
S	2p3	163.7	1.45
		162.7	1.45
		161.5	8.18

Table S3.3: Summary of the atomic composition stoichiometric assignments obtained from the fitting of the XPS spectra for NZTS.

Element	Assignment	Binding energy (eV)	Atomic %
C	C-C	284.8	58.66
	C-O	286.1	9.26
	O-C=O	288.7	1.58
O	C-O	531.9	2.74
	C=O	533.3	2.23
	Metal oxide	529	0.08
N	N 1s	399,7	1.28
		401.4	0.91
Cl	Cl 2p3	198.8	0.97
Na	Na 1s	1072	1.2
Zn	Zn 2p3	1023.8	0.73
		1021.8	3.91
Sn	Sn 3d5	486.4	2.87
S	2p3	161.3	10.85
		162.7	2.7

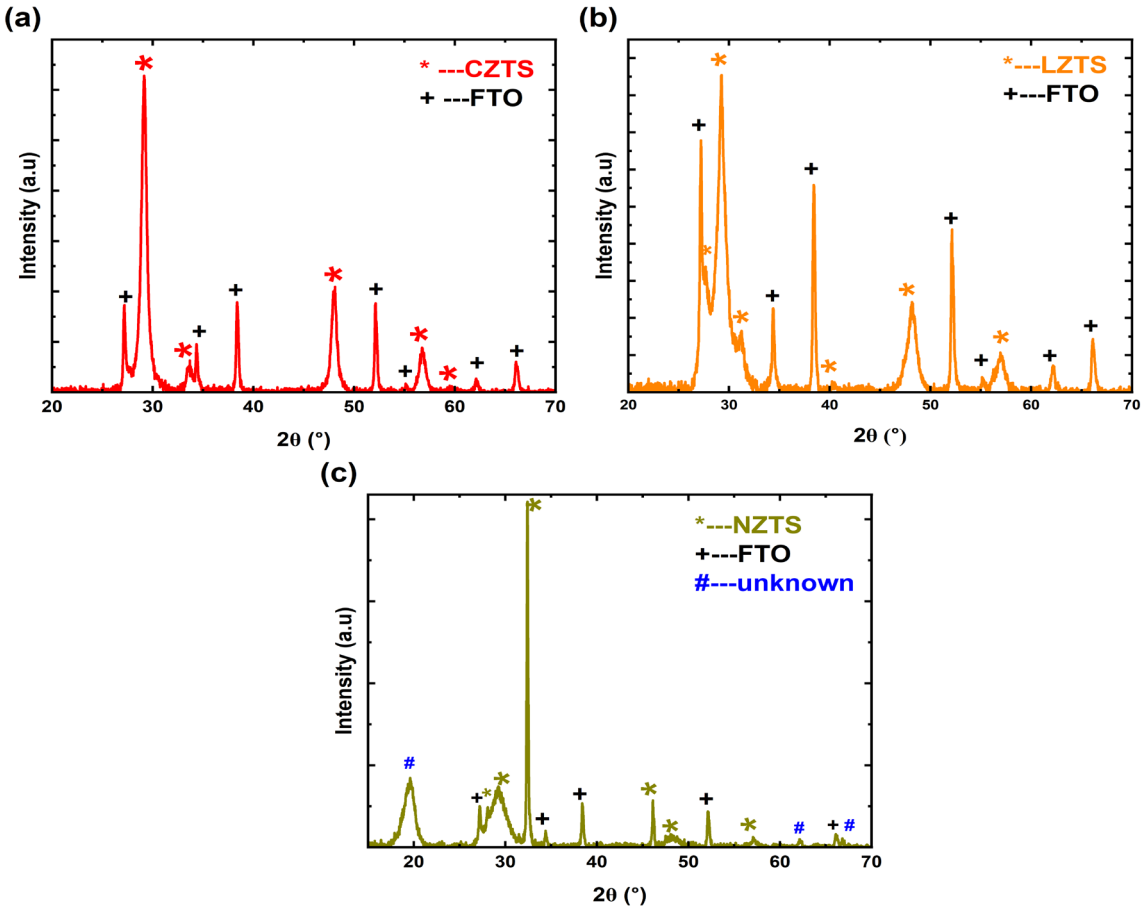

Figure S4.1: XRD of (a) CZTS, (b) LZTS and (c) NZTS thin films fabricated on FTO conductive glass substrate.